

**Methods for Rendering MRI Brain Scans Into Gray Matter, White Matter,  
and CSF Density Maps**

Manuel Mourino, Ph.D., Henry Rusinek, Ph.D., Henryk Kowalski, M.D.,  
Leo Stylopoulos, M.D., Mony De Leon, Ed., and Ajax George, M.D.  
New York University Medical Center, Dept. of Radiology, 560 First Avenue, NYC, NY 10016

Proposal

The New York University Medical Center's Department of Radiology and Department of Psychology Aging and Dementia Research Project have undertaken to use MRI as a means of mapping gray matter, white matter, and CSF in Alzheimer's patients. Our goal is to detect what, if any, morphological changes occur in their brains as the disease progresses. With this as impetus we have developed a method for rendering MR scans into gray matter, white matter, and CSF density maps and made a study of the possible pulse sequences which can be used to acquire the scans.

Method

Assume that the signal which is represented by an image voxel in an MRI scan,  $S$ , can be broken down in the following fashion,

$$S = v_g S_g + v_w S_w + v_c S_c ; \quad (1)$$

where  $v_g$ ,  $v_w$ , and  $v_c$  are the fractional volume of the voxel occupied by, respectively, gray matter, white matter, and CSF (that is,  $v_g + v_w + v_c = 1.0$ ) ; and  $S_g$ ,  $S_w$ , and  $S_c$ , are the MR signals in a voxel of pure gray matter, white matter, and CSF for the imaging parameters which were used to perform the MR scan. It follows that we can process a pair of registered MR multislice head studies into a  $v_g$ ,  $v_w$  and  $v_c$  map. Our approach is as follows: in each of two studies we find areas of voxels which encompass pure gray matter, white matter, and CSF. Specifically, the signal in those three voxel groups in the first study can be written as,  $S_{1g}$ ,  $S_{1w}$ , and  $S_{1c}$ , and in the second study as,  $S_{2g}$ ,  $S_{2w}$ , and  $S_{2c}$ . Thus, we can write for each image voxel in a slice in the first study an equation of the form,

$$S_1 = v_g S_{1g} + v_w S_{1w} + v_c S_{1c}, \quad (2)$$

and for each corresponding slice in the second study a complimentary equation,

$$S_2 = v_g S_{2g} + v_w S_{2w} + v_c S_{2c}, \quad (3)$$

These equations can then be solved for  $v_w$  and  $v_c$  under the condition,

$$v_g + v_w + v_c = 1.0 \quad (4)$$

Pulse Sequences

On a standard MRI system there are five basic methods of generating scan pairs [ Two-Echo SE Scan (1), Two Separate SE Scans (2), Two-Echo IR Scan (3), Two Separate IR Scans (4), and Mixed SE-IR Scan (5) ]. We have ascertained for each of them what imaging parameters produce the smallest amount of uncertainty ( $\sigma$ ) in  $v_w$  and  $v_c$  with respect to the uncertainty of the data input into equations (2) and (3). What we sought can be expressed mathematically, for each

scanning method, as the imaging parameters which yield the minimum value of the quantity,

$$CN = \frac{1}{\epsilon} \left\{ \frac{[\sigma^2(v_w) + \sigma^2(v_c)]}{[v_w^2 + v_c^2]} \right\}^{1/2};$$

where we have made the assumption that the uncertainty in all values input into equations (2) and (3) are a constant fraction of that value [ $\sigma^2(S) = \epsilon S$ ].

We list below for each imaging method the optimum imaging parameters as defined by this equation at 0.5 Tesla and 1.5 Tesla (the format for SE parameters is TR/TE and that for IR parameters is TR/TI/TE)

0.5 Tesla		
Parameters	CN	
(1) 1700/31/132	11.30±1.72	
(2) 1739/30 2097/117	11.20±1.70	
(3) 1553/399/34/184	4.28±0.32	
(4) 1474/383/28 5117/651/187	3.75±0.25	
(5) 211/34 1008/280/34	5.72±0.94	
1.5 Tesla		
Parameters	CN	
(1) 1825/28/113	12.60±1.91	
(2) 1732/28 2232/102	12.50±1.89	
(3) 1892/534/34/184	5.92±0.45	
(4) 1440/458/28 4989/827/184	5.50±0.41	
(5) 208/34 1015/323/35	7.89±1.25	

From these data we could say that if  $\epsilon$  is the same constant for all imaging methods at both 0.5T and 1.5T then the optimum imaging method is Two Separate IR Scans performed at 0.5 Tesla. This conclusion is not necessarily valid for several reasons. For one thing, it is based on assumptions about the nature of the behavior of the signal-to-noise ratio in MRI systems (e.g. that the system tunes and calibrates to set  $\epsilon$  at the same value for the first echo for all imaging sequences and imaging parameters). Further cause for modifying this opinion is that if one only wants to know the total amount of gray matter, white matter, and CSF, in large brain volumes it might be possible to significantly improve CN for an imaging sequence without altering its acquisition parameters. Lastly, data acquisition time precludes the full application of several of these sequences. These variables must be considered when making a choice of imaging method. How they affect it will be the subject of our presentation.

## EFFECTS OF AGING AND DURATION OF HYPERTENSION ON DEVELOPMENT OF LACUNAR STATE

M. Nakamura, T. Sawada, H. Naritomi, Y. Kuriyama and S. Imaoka  
National Cardiovascular Center, Osaka, Japan

Introduction

Magnetic resonance imaging (MRI) often demonstrates multiple lacunar lesions in stroke patients and subjects who have no apparent episode of stroke. The lesions seem to be observed most commonly in patients with high age or hypertension suggesting that these two are important determining factors of lacunes. In this study, number of lacunes in MRI was analyzed with special reference to age, presence or absence of hypertension and duration of hypertension.

Case Materials and Methods

Among patients who were admitted into our neurology department for neurological evaluation or treatment of neurological diseases during the last two years, 58 cases were chosen for the study according to the following criteria; 1) cases with only one or no episode of lacunar stroke in past history, 2) cases with no risk factors of stroke except for hypertension, and 3) cases with no obvious evidence of major cerebral artery occlusion. They consisted of 40 men and 18 women with ages ranging from 20-86 years old. Twenty-nine were hypertensive, and the other 29 were normotensive. Thirty-eight had one episode of lacunar stroke, and the other 10 had no history of stroke. MRI was obtained in all the patients using 1.5 Tesla superconductive prototype system "Magnetom H15" (Siemens). Spin echo pulse sequence was used, T<sub>1</sub>-weighted sequence as SE(500/17) and T<sub>2</sub>-weighted sequence as SE(2000/90 and 30). Slices showing basal ganglia and pons were reviewed by two of the authors, and the number of lacunes was counted. Relationships of the number of lacunes with age, presence or absence of hypertension and duration of hypertension were investigated.

Results

MRI demonstrated one or more lacunar lesions in 38 patients and no lacune in the remaining 20 patients. In the normotensive patients, the number of lacunes was always less than two, if their ages were below 70 years old. The number of lacunes increased abruptly, if the ages exceeded 70 years old (Fig. 1). In the hypertensive patients, there were significantly larger numbers of lacunes compared with the normotensives. In this group, the number of lacunes had no correlation with age but tended to increase correlatively with duration of hypertension. When the entire

patients including both normotensives and hypertensives were analyzed, the following fact was observed; (1) the number of lacunes was always two or less, if the age plus duration of hypertension was below 70 years, and (2) the number of lacunes increased suddenly, if the age plus duration of hypertension exceeded 70 years (Fig. 2).

Discussion

The results have indicated that age and duration of hypertension are two important factors influencing development of lacunar state. Age plus duration of hypertension above 70 years appears to be critical for development of multiple lacunes.

Fig. 1.

Relationship between Age and Lacunes

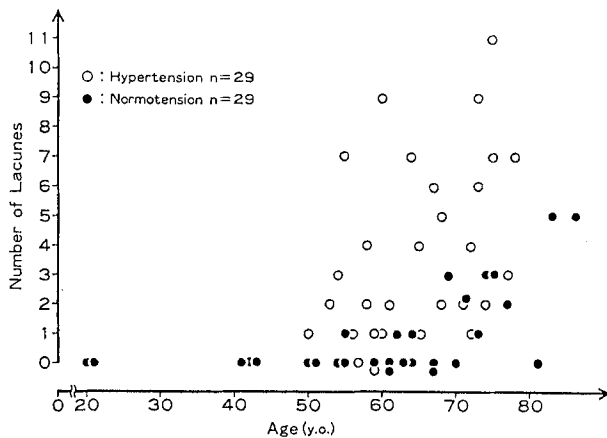
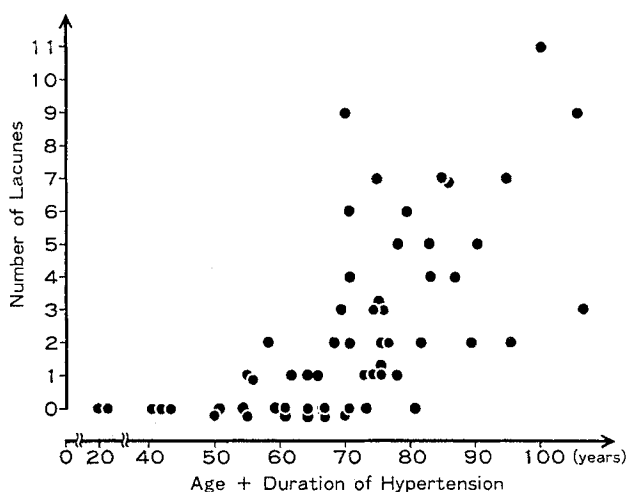


Fig. 2.

Relationship between Lacunes and Age, Duration of Hypertension



Aspect of the fibrous cranial face displasia in M.R.

L. Lopez-Ibor, E. Monton, J.R. Varela and J. Perez Moreiras  
de Santiago de Compostella

Aspect of the fibrous cranial face  
displasia in MR

The authors present the interesting M.R. studies of three patients suffering from a fibrous cranial-face displasia.

The examinations were compared with the findings in the conventional radiology and C.T.

The M.R. allows better visualization, than other examinations, of the scope of the lesion. It also allows differentiation of the tumourous fibrous zones from the oseous ones and their influence on the brain parenchima.

Extended Field of View Magnetic Resonance Imaging  
of the Spine Using the Body Coil With Spatial Presaturation

Maurice H. Lipper, Wayne S. Cail, John P. Mugler, James R. Brookeman  
Dept. of Radiology, University of Virginia Health Sciences Center, Charlottesville, VA 22908

#### Introduction

Magnetic resonance imaging is recognized as an effective method for the evaluation of spinal metastatic disease (1,2) and trauma, specifically in the detection of cord compression. In order to cover the entire spine it has been necessary until recently to obtain multiple separate sequences of each region of the spine using surface coils with motion compensation techniques such as cardiac triggering and gradient motion refocusing. These techniques are time consuming requiring repositioning of the patient and the surface coils, or the use of moveable coils, and are especially tedious for patients who are suffering from considerable pain due to bony metastases or trauma. To overcome this handicap we have developed and implemented a user friendly technique for obtaining images of the entire spine without repositioning the patient.

#### Method

To achieve this on our 1.0T Siemens Magnetom (GBS 1 hardware with B3 and D1 software) we are routinely using the 500 mm body coil for extended field of view imaging in the crano-caudal direction. In the absence of surface coil imaging one would expect considerable motion artifact due to flow, cardiac and respiratory motion and peristalsis, as well as wrap-around artifact. To overcome this drawback we have effectively employed spatial presaturation. Spatial presaturation was proposed in 1987 by Felmlee and Ehman (3) and Edelman et al (4), who noted that in many cases artifacts arise from motion of structures outside major regions of interest and that these ghost artifacts cannot occur if the structures that generate them do not produce an RF signal. However, there has been some delay in implementing a user friendly version of this technique appropriate for routine clinical use. We have designed and implemented a Fortran program, activated by a console function key, which follows the normal sequence menu, and in a simple straightforward manner enables the operator to select the spatial presaturation parameters, such as width, location and orientation. The technologist need answer only questions pertaining to the width of the slab of presaturation and the location of the center of the slab in the phase encoding direction, in order to decrease the artifact without obscuring the spine.

Presaturation is achieved by a large angle pulse, 110 degrees, and dephasing gradients which precede the conventional 90-180 degree sequence and add an additional 20 msec to the slice loop. The angle of 110 degrees instead of 90 degree pulse as advocated by Edelman, was found by experiment to provide the most effective saturation of the tissues anterior to the spine, given the other timing parameters of the sequence. To reduce interference of the

saturation slab with adjacent tissue, the 110 degree pulse employed an optimized RF profile, provided by Silver (Siemens Medical Systems) (5). The orientation, thickness and position of the presaturated slab can be defined independently from a preliminary biaxial scout consisting of seven coronal and one sagittal slice. Also, spatial presaturation can be used in conjunction with other motion compensation techniques.

#### Results and Discussion

We are routinely using spatial presaturation when imaging the cervical and thoracic spine, irrespective of whether the body or surface coils are used, and during the seven month period from July 1988 until February 1989 we have employed this technique on 349 patients. We use presaturation for T1-weighted sagittal sequences only with the body coil and for both T1 and T2-weighted sagittal sequences with surface coils. Of these patients, 59 have been studied by the body coil, presaturation technique. It has been possible to examine almost the entire spine in one sequence with a second sequence being only occasionally necessary to cover a remaining area. Usually following this sequence, we may study any area showing pathology in greater detail using a surface coil, if the patient's condition so permits.

Of the 59 patients examined by this technique, 42 were investigated for metastatic disease, five for trauma, three for spinal dysraphism and nine for miscellaneous conditions. Thirty-seven studies were positive for metastases with 14 showing cord compression and 4 showed positive evidence of spinal trauma with one instance of cord compression. The nine miscellaneous conditions included three spinal degenerative conditions, two cases of cord atrophy, one each of cord swelling, extensive astrocytoma, arachnoid cyst and bone infarcts due to sickle cell disease. All studies were of good diagnostic quality except for three suboptimal studies, two due to patient motion and one with metallic shunt artifact. The only drawback from the use of the body coil was some increase in noise which was more than compensated for by the reduction in motion artifact achieved by spatial presaturation and the advantages of the extended field of view.

#### References

1. Sarpel, S., Sarpel, G., Yu, E., et al. *Cancer*, 59, 1112, 1987.
2. Smoker, W.R.K., Godersky, J.C., Knutson, R.K., et al. *AJNR*, 8, 901, 1987.
3. Felmlee, J.P., Ehman, R.L., *Radiology*, 164, 559, 1987.
4. Edelman, R.R., Atkinson, D.J., Silver, M.S., et al. *Radiology*, 166, 231, 1988.
5. Warren, W.S., Silver, M.S., *Adv. Magn. Reson.*, 12, 247, 1988.

### **3D MR Imaging with Gd-DTPA in Head-Lesions**

T.Vogl,MD, C.Wilimzig,MD, G.Grevers,MD, G.Laub,PhD, J.Lissner,MD  
Department of Radiology, Klinikum Großhadern, University of Munich

#### **Introduction**

Three-dimensional (3D) MR imaging technique is not a new concept, however there are very little experiences concerning clinical trials. Especially in head and neck lesions the accuracy of this new imaging method has not yet been tested. A pilot study was performed to evaluate the diagnostic value for demonstrating the head and neck lesions and topographical structures implemented in a three-dimensional reconstruction of the whole head. Twenty-five normal volunteers and ten patients with head and neck lesions were so far primarily examined with standard 2D MR imaging with the contrast medium Gadolinium-DTPA. After this examination a 3D MR imaging was performed. The diagnostic value of the 3D-images calculated at a workstation is discussed in this report.

#### **Methods and Material**

MR imaging was performed with a 1.0T MAGNETOM (SIEMENS) using a 25cm diameter headcoil. To maintain a satisfactory signal-to-noise ratio, to reduce motion artefacts and to obtain vessels with maximum grey value a special 3D-FLASH sequence was used, which was developed by SIEMENS, Erlangen. The TR/TE was 40/15, the flip angle was 40° and the slice thickness of the 128 slices ranged between 1.0 and 1.5mm depending of the width of the patients head. The patients were measured after application of the contrast medium Gadolinium-DTPA.

3D-reconstructions were performed with a separate workstation. To transfer the data from the MAGNETOM to this workstation special equipment was required, which transform the MAGNETOM 16bit data-size to the workstations 8bit data-size. The 3D-reconstruction mode based on the ray-tracing model: from a point of view outside the original data set a succession of rays descends through the data cube. Thus, it was possible to construct arbitrarily complex extraction schemes, and the resulting object could be viewed from any direction. In the surface mode a 3D-surface view of the patients head was reconstructed. In the next and most important step a section of the 3D-reconstructed head was cut off and the now visuable inner parts of the head were imaged by projecting the concerned parts of the original slices in the 3D-reconstructed image.

#### **Results**

MR imaging and 3D-reconstruction was performed primarily at 25 normal volunteers optimizing the examination and calculation conditions. Several 3D-FLASH sequences were compared and the one with the lowest motion artefacts and best signal to noise ratio was choosen using the upper described sequence parameters which proved to be optimal for this special sequence. 3D-reconstruction of the volunteers data of the skull base, temporal bone, parapharyngeal space and surface has been calculated to evaluate the artefacts and the point of view. After optimizing the conditions 10 patients underwent the examination and calculation procedures. Diagnosis included skull base lesions in five patients, glomus tumors in two, meningiomas in two and hemangioma in one. The application of the contrast medium Gadolinium-DTPA proved to be helpful due to signal intensity. 3D-reconstruction revealed well topographic details of the lesions including the spread of infiltration and destruction of soft tissue. Additionally the simultaneous view of multiple slices in different orientations makes this method well suited for evaluation of the spread of the lesion and the relationship between lesion and surrounding tissue.

#### **Conclusion**

The preliminary results on 3D-reconstruction of head-lesions are encouraging. Images of selected anatomy such as tumor tissue or vessels can be reconstructed to show soft tissue boundaries. The important aspects of the lesions are much easier to evaluate by 3D-reconstructed images than by mentally reconstructing the morphology from individual slices. However, some problems are still to solve. The period of one 3D-FLASH acquisition is quite long, thus the rate of motion artefacts is high, especially when patients are old or not in a good condition. Additionally the software does not satisfactory support the user when projecting parts of the original slices into the 3D-reconstructed image.

In summary 3D-reconstruction is going to be an accurate method for the evaluation of head-lesions and the clinical use of this modality has to be expected in the future.

MR-Imaging of the Nasopharynx, the Paranasal Sinuses and the Skull Base with Spin Echo Sequences and Gradient Echo Sequences

P. Held, N. Obletter, C. Prüll, H. Kett, A. Breit;  
Munich, Technical University

The object of the paper is a comparison between the value of spin-echo (SE) modes and gradient-echo (GE)-imaging (FISP, FLASH) in order to estimate the extension of tumors of the nasopharynx.

Technique: Magnetom, 1.0T (Siemens), head coil, T1 weighted, balanced and T2 weighted SE sequences; GE sequences: FLASH (TR 32 ms TE 15 ms flip angle 40° and 70°), FISP (TR 32 ms TE 15 ms flip angle 90°), 3D GE sequences FLASH (flip angle 40° and 70°) with gadolinium (Gd)-DTPA iv, FISP (flip angle 90°), volume thickness 16 cm, voxel size: 1,2 x 1,2 x 1,2 mm<sup>3</sup>.

Patients: 94 examinations with SE sequences and GE sequences, in 23 cases also with 3D GE sequences.

Result: The different acquisition conditions - monoslice, multislice, 3D-technique - lead to different signal characteristics of the GE-sequences. Performing a volume mode, images of any orientation - also curved slices - can be obtained from a 3D data set by means of the image processing system MIP-MR (Kontron). The use of 3D GE sequences allows a better evaluation of the extension of the tumor than common SE-modes.

3D-Sequenzen mit schnellem Bildverarbeitungssystem

RöFo 147, 557-562 (1987).

- 3) Obletter N., Kett H., Breit A.: Erweiterung der diagnostischen Methodik in der MR-Tomographie: Rekonstruktion von beliebigen Schichtorientierungen, S. 43-48, in: Lehner G. (Hrsg.), Kongressband Österreichischer Röntgenkongress, Wien, 1987.
- 4) Obletter N., Kett H., Breit A.: 3D-Sequenzen bei Untersuchungen an der Wirbelsäule. Der Nuklearmediziner 11, 271-276 (1988).
- 5) Oppelt A., Graumann R., Barfuß H., Fischer H., Hartl W., Schajor F.: FISP: Eine neue schnelle Pulssequenz für die Kernspintomographie. Electromedia 54, 14-18 (1986).

References:

- 1) Frahm J., Haase A., Matthaei D.: Rapid three dimensional MR Imaging using the FLASH technique. J. Comp. Assist. Tomogr. 10, 363-368 (1986).
- 2) Kett H., Obletter N., Breit A.: Weiterentwicklung der diagnostischen Möglichkeiten in der MR-Tomographie: Kombination von

## MRI FINDINGS IN GRAVES DISEASE

Schilling A., Bende T., Seiler T., Wollensak J.

I. Introduction

Graves disease is the orbital manifestation of a thyroidal malfunction. The cardinal clinical symptom is proptosis accompanied by a great variety of other ophthalmological disorders such as palsies, lacrimal gland dysfunction and compression of the optic nerve. The latter leads to the loss of visual acuity in the progredient stages of the disease. All symptoms are thought to be caused by the massive abundance of glycosaminoglycans into the orbital fat and the ocular muscles. With MRI a imaging method is available that allows to evaluate the morphological changes and therefore the early diagnosis which is critical for sufficient treatment. The purpose of the presented study is to quantify the pathological findings in MRI.

II. Material and Methods

20 out-patients with clinical signs of Graves disease since 2 to 5 years and 5 healthy subjects that served as a control group had a thoroughly ophthalmologic examination. After that MRI was performed not later than 10 days after first presentation. A low field system ( Bruker BMT 1100 ) with a magnetic field of 0.24 T was used. We utilized orbital coronar ( CPMG, 4SSE, TR 1600 msec, TE 55 msec ), transverse and sagital sections ( CPMG, 1S4E, TR 400 msec, TE 55 msec ) using a surface coil of 10 cm diameter. This coil was specifically designed for ocular investigation. The resulting images were processed and geometrically and mathematically evaluated for the relaxation time T2 of ocular muscles and orbital fat, muscular cross section and relative spin densities of these tissues.

III. Results

No significant change of the spin density was observable in the examinations of the 20 patients with clinical symptoms of Graves disease.

The relaxation time T2 of the ocular muscles increased from 75 - 85 msec in the healthy subjects to 100 - 130 msec in the studied group. In the orbital fat the T2 time averaged to be 110 msec ( SD 4.4 msec ) in contrast to the normal value of 90 msec ( SD 3.7 msec ). Geometrical analysis showed a distinct difference in the factor of enlargement for the four straight ocular muscles. The nasal muscle, the superior and inferior increased by a factor of  $2.1 \pm 0.6$  and the temporal by  $1.6 \pm 0.4$  in a coronar slice about 15 mm retrobulbar.

In 3 cases a dilatation of the subarachnoidal space of the optic nerve was observable bilaterally as bright stripes accompanying the nerve. This was unilaterally detectable in 4 cases.

IV. Discussion

As expected MRI shows a thickening of the ocular muscles in cases of Graves disease. Interestingly the temporal ocular muscle presents the least increase. The increase in size was best measurable in a coronar slice 15 mm retrobulbar. This is easily explained by the fact that the primary thickness of the muscles is at maximum at this site.

The increase of the T2 relaxation time in muscle tissue as well as in orbital fat is a typical finding in Graves disease. This is understandable by the appearence of glycosasminoglycans and the subsequent edema in these structures. Both is emphasised in MR images by bright isles included in the normal tissues. In each investigated eye with the disease a coincident increase of the relaxation times in ocular muscles and orbital fat was determind.

As previously postulated neither the increase of T2 relaxation time nor the enlargement of the muscular cross section show any correlation to the thyreoidal function.

The dilatation of the subarachnoidal space of the optic nerve is the visible sign of a compression of the proximal nerve. This seems to be a good diagnostic findingto initiate a decompression therapy.

Neither the increase of T2 relaxation time nor the enlargement of the muscular cross section are to date of any therapeutical consequences as interesting as these findings might be in the further investigation of the pathomechanism of Graves disease. However, the dilatation of the subarachnoidal space of the optic nerve is of eminent interest in the clinical routine. It is the very first symptom of a nerve lesion long before a loss of the visual acuity is detectable.

## MR of Head and Neck Cystic Hygromas

WTC Yuh, Y Sato, SD Gray, SCS Kao, WL Smith, EA Franken, Jr., Depts. of Radiology and Otolaryngology, Univ. of Iowa, Iowa City, IA 52242, U.S.A.

MR was performed in six children with surgically proved cystic hygromas of the neck. One patient had bilateral involvement. Two patients had involvement that extended inferiorly to the thoracic inlet. Five patients had follow-up MR postoperatively. On T1-weighted images, these lesions had signal intensity greater than that of muscle. On T2-weighted images, these lesions had extremely high signal intensity probably due to the proteinaceous nature of their contents. The multilocular cystic nature of the tumor was best demonstrated by T2-weighted images. The extent of involvement was best outlined by coronal T2-weighted images. Fluid levels best seen on T2-weighted axial images were probably due to various combinations of protein and/or lipid content. All these MR findings were indicative of cystic hygroma. We conclude that MR is a useful tool in the detection, localization, and characterization of cystic hygromas and can be used in preoperative and postoperative patients.

**T1 and T2 Measurements in Cerebral White Matter and Hippocampus of Patients with Suspected Alzheimer's Disease - An In-Vivo Analysis**

Dra. Levin, María Elena; Dr. Eurnekian, Alberto  
Centro de Diagnóstico San Martín de Tours, Buenos Aires, ARGENTINA

**Introduction**

The advent of Magnetic Resonance (MR) permitted new research modalities - unconceivable until now because the physical principles on which it is based are substantially different from those of radiology.

Ultra Low Field (ULF) MR offers additional advantages since patients with metallic prostheses can be studied safely, and T1 tissue contrast is greater at ULF than at higher fields.

Until now diagnosis were traditionally based on images but, granting that T1 and T2 values are different for each tissue, be it normal or pathologic, we can use MR technique in order to examine different pathological tissues through the measurement of their relaxation parameters.

This adds a new dimension to MR since it affords a biological, non-invasive and in-vivo examination of body tissues.

Our aim was to determine the T1 and T2 behaviour of periventricular white matter (PVM) and hippocampal formation (HF) in patients with suspected Dementia of Alzheimer Type (SDAT) through a double-blind method.

**Materials and methods**

The study was carried out on a Total Body ULF MR scanner operating at 0.02T (Acutscan 110, Instrumentarium Corp., Helsinki, Finland). T1 and T2 values were obtained at PVM centrum semiovale and HF. Intensity values were obtained from ROI's located symmetrically over PVM and HF.

Patients were examined with a double-blind method in order to have an approach not influenced by the patient's clinical records.

We examined 5 (five) normal volunteers and 5 (five) patients with SDAT.

We have established as a methodology for this study that all the patients should be examined with equal parameters, through slices going 50 mm upwards and 10 mm downwards starting at the 0 mm slice which coincided with the orbito-meatal line, in order to obtain comparable results.

On a SR (Saturation Recovery - 90° pulses) sequence, 200TR/30TE Scout View Image, two multislice non-contiguous 10 mm Spin Echo sequences were planned for axial and coronal views 2000TR/150 and 200TE, in order to obtain T2 values.

T1 was calculated on two IR (Inversion Recovery) sequences at TR=1s., TI=50/375, TE 40 ms.

T1 and T2 assumed a simple monoexponential behaviour and were calculated by the following formulae:

$$\begin{aligned} \text{IR sequence: } S &= N(\%) \exp(-TE/T2)(1-2\exp(-TI/T1)) + \exp(-TR/T1) \\ \text{SE sequence: } S &= K \exp(-TE/T2) \end{aligned}$$

T1 was calculated through iterations of Intensities' ratio (average of Region of Interest (ROI)'s, in two sequences with  $\neq$  T1) until finding the suitable value.

T2 was calculated directly from the average of the two intensities obtained from the SE sequences with different TRs.

We are presenting hereby a group of patients, 2 females and 3 males, with clinical SDAT, following the general criteria of the NINCS - ADRA workgroup.

**Results and discussion**

We assume that obtaining a multislice format in the Spin Echo sequences with our unit do not alter substantially our results due to minimal variations in slice positioning or patients' movements.

The selected slices for T1 and T2 measurements are located centrally relative to the magnetic field, and patients heads were kept in a fixed position throughout the examination.

The IR sequence was performed at 1000 ms.TR. Since we got T1 relaxation times over 330 ms., we consider that we must study our patients further with IR sequences at 1500 ms.TR.

Since our T1 and T2 measurements obtained on normal volunteers are quite similar to those from other ULF MR departments (St. Görans Hospital at Karolinska Institute, Stockholm, Sweden), we conclude that our results are reliable and we will have in mind all the drawbacks previously mentioned for the follow-up work.

Our five SDAT patients showed T1 and T2 values over the two cerebral hemispheres within a quite different range of values when compared to those of normal volunteers.

T1 and T2 values of patients with SDAT are widely lengthened when compared to normal controls, they also show longer relaxation times corresponding to worsened clinical condition.

All 5 SDAT patients presented multiple WM plaques in both cerebral hemispheres, characterized by a long T1 and T2 relaxation times.

**Conclusions**

T1 and T2 measurements were obtained in brains of normal volunteers and patients with suspected Alzheimer's disease. These relaxation parameters showed an statistically significant lengthening, particularly in periventricular WM and HF, which correlates well with clinical condition: the longer the time (mainly T1), the worse the neurological status of the patient.

We found T2 values highly altered in HF of all patients scanned when compared with normal controls.

## MRI of the Pituitary Adenoma at 1.5 T

Suresh Patel, M.D., Allan M. Haggard, M.D., Magnetic Resonance Imaging, Dept of Diagnostic Radiology, Henry Ford Hospital, 2799 W. Grand Blvd., Detroit, MI 48202

**INTRODUCTION:**

Our experience with various histologic types of sellar lesions is presented and correlated with MR findings in the presence or absence of clinical endocrinopathy.

**MATERIALS AND METHODS:**

A retrospective analysis of 28 cases of functioning and nonfunctioning pituitary adenomas was carried out. All cases were documented by operative correlation. In addition, histochemical analysis were accomplished on all tumors. All studies were performed at 1.5 T (GE, Milwaukee, Wis), multiplanar T1, and T2 weighted images were obtained including both sagittal and coronal projection (SE 600-800/25/4, 2500/25,90/2) using 3 mm slice thickness with 0.5 mm interslice gap. All examinations reviewed by an observer experienced in MR diagnosis. Gross morphologic features and signal intensity were noted and correlated with eventual histologic, histochemical outcome.

**RESULTS:**

Of the 28 patients studied, 11 were found to have nonfunctioning (chromophobe) adenomas. Four patients (14%) had growth hormone secreting adenomas and 5 (18%) had ACTH secreting adenomas. Five (18%) prolactinomas and three (11%) cases of combined prolactinoma and GH secreting tumors were found. Morphologic identification of an abnormality depended on contour deformity of the pituitary gland, deviation of the stalk or elevated signal intensity on the long TR/TE images. Cavernous sinus invasion was readily apparent. Five of 28 (18%) pituitary masses showed evidence of subacute hemorrhage on short TR/TE images. The later pulse sequence was most beneficial in assessing possible pituitary apoplexy. There was no correlation between signal intensity of the lesion and eventual histologic outcome. Furthermore, no distinguishing characteristics were found to suggest whether a given lesion was endocrinologically active at the time of study.

**Craniopharyngioma presenting with visual disturbance -  
optic tract hypersignal on MRI.**

Yous BD<sup>1</sup>, Plant GT<sup>1</sup>, Stevens JM<sup>2</sup>, McDonald WI<sup>1</sup>, Crockard HA<sup>3</sup>.  
 1. MRI Research Group, The Institute of Neurology, Queen Sq, London.  
 2. Department of Radiology, The National Hospitals for Nervous Diseases.  
 3. Department of Neurosurgery, The National Hospitals for Nervous Diseases,  
 Queen Square, London.

**Introduction.**

Two patients presented with progressive visual failure. MRI showed hyper-signal extending from the optic chiasm along both optic tracts in each case. Both patients were found to have craniopharyngioma.

**Case No. 1.**

A 37 year-old white female was admitted with 2 months of progressive blurring of vision on the right. Three weeks later she developed a left temporal field defect and symptoms of post fixational blindness. Her periods had been erratic and she gained 6kg in weight over the previous month. On examination the acuities were reduced to 6/36R and 6/24L, but colour vision, pupillary responses and fundi were normal. Goldmann perimetry showed incomplete left temporal hemianopia and right superior temporal quadrantanopia.

CT scan showed a well defined mass of brain density within the supra-sellar cistern which appeared to deform the floor of the third ventricle. MRI showed a supra-sellar mass of high signal intensity which could not be distinguished from the optic chiasm and an apparently normal pituitary fossa. The high signal extended postero-laterally towards the lateral thalamic regions, along the paths of the optic tracts. A large craniopharyngioma was resected. It was compressing and stretching the optic chiasm, but remained separate from it and extended posteriorly towards the hypothalamus. Acuities improved to 6/9R and 6/12L but there was little alteration in visual field loss. Further MRI scans, 2 and 6 months post-operatively showed no evidence of the abnormal signal, nor of residual tumour.

**Case No. 2.**

A 46 year-old white female presented with three weeks of deteriorating vision and mild headache. The near acuities were N14R and N18L. Visual fields were intact. CT scan showed a large supra-sellar mass. The pituitary fossa was normal. MRI showed a rounded mass of high signal intensity effacing the anterior part of the third ventricle and extending into the inter-peduncular

fossa. The increased signal extended postero-laterally towards the lateral thalamic regions, along the optic tracts. A cystic tumour was found at craniotomy which was entirely supra-sellar. The optic nerves were grossly stretched over it. The chiasm was pre-fixed. The tumour was entirely removed and the optic chiasm decompressed. Pathological examination confirmed it to be a craniopharyngiomatous cyst. Post-operatively the visual acuities improved to N5R (6/6) and N5L (6/9). Goldmann perimetry was normal. MRI post-operatively showed disappearance of the high signal abnormality, although the floor of the third ventricle remained slightly thickened.

**Discussion.**

The distinction between intrinsic and extrinsic lesions of the anterior visual pathways may be difficult. In each of the two cases presented an unusual feature on MRI was interpreted as favouring a diagnosis of chiasmatic glioma. This was further supported by the absence of clear delineation of tumour from chiasm.

In the case of intra-chiasmatic craniopharyngioma, Brodsky et al.<sup>1</sup> have pointed to a relatively short extension of optic nerve expansion anterior to an enlarged bilobed chiasm as a feature on MRI which may aid distinction from glioma. In the two cases we have described, however the tumours were extrinsic to the chiasm. A possible explanation for our findings is the tracking<sup>2</sup> of edema fluid along fiber bundles.

Whilst this feature may not be specific to craniopharyngioma, its occurrence should raise this possibility.

**References.**

1. Brodsky MC, Hoyt WF, Barnwell SL, Wilson CB. *J Neurosurg*, 68, 300, 1988.
2. Cowley AR. *AJNR*, 4, 915, 1983.

**Acknowledgements.**

The NMR Research Group is supported by the Multiple Sclerosis Society of Great Britain and Northern Ireland and the Medical Research Council.

**Gadolinium-DTPA (Magnevist<sup>TM</sup>) in Pediatric MRI**

Aye A. Khine Hackett, M.D., Emanuel Kanal, M.D., Gerald L. Wolf, Ph.D., M.D.  
Pittsburgh NMR Institute, VAMC Hospital and University of Pittsburgh

One hundred thirty-seven pediatric cases were studied with Magnevist<sup>TM</sup> at the Pittsburgh NMR Institute for evaluation of the intracranial and skull base pathology. Imaging was performed on 2 General Electric 1.5 Tesla systems, both before and after intravenous administration of 0.2 ml/kg (0.1 mmol/kg) Magnevist<sup>TM</sup>). At least three series were performed including sagittal, axial, and coronal planes emphasizing proton spin density and T1 and T2 contrast information. MR studies must often be combined with sedation, as are non-enhanced studies in this population. Our results to date reveal 51 cases with sedation and 86 without. Significant positive imaging yield was 24%. There is also value in negative studies, but this has not been fully assessed. Adverse events were 1 headache and 1 seizure (patient referred for MRI seizure protocol). There were 78 males and 59 females, the youngest was one month old and the median age was 8 years. As is common for drugs useful in pediatric population, Magnevist<sup>TM</sup> has not been submitted for FDA approval in the pediatric population.

The European Congress of NMR in Berlin, 1988, summarized the worldwide experience with Magnevist<sup>TM</sup> in over 7,000 cases. Since its introduction in the United States, more than 140,000 additional studies have been performed with less than 1% side effects.

Our own experience further attests to the safety and efficacy of Magnevist<sup>TM</sup>. We believe the very low incidence of adverse reactions of any type with MRI compares quite favorably with the low but finite risks associated with ionizing radiation as with CT scans. We, therefore, feel that pre and post contrast enhanced MRI of the CNS may be preferable to CT in this age group as a primarily diagnostic tool.

### MR Microscopy of Tissue Homogeneity

G. A. Johnson<sup>1</sup>, Ph.D., G. P. Cofer<sup>1</sup>, M.S., L. W. Hedlund<sup>1</sup>, Ph.D., S. B. Zivl<sup>1</sup>,  
B.S., M. B. Thompson<sup>2</sup>, DVM, Ph.D., R. R. Maronpot<sup>2</sup>, Ph.D.

<sup>1</sup>Duke Univ. Med. Ctr., Durham, NC, and

<sup>2</sup>Natl. Inst. of Environ. Health Sciences, Research Triangle Park, NC

#### Introduction

Early work in MRI clearly demonstrated the potential for tissue characterization using T1 and T2 (1). The parameters are sensitive but frequently not specific. We suggest here that measure of tissue (T1 and T2) homogeneity using MR microscopy may provide an additional tool for characterizing tissue.

#### Methods

Liver foci were induced in Fisher 344 rats using diethylnitrosamine (DEN) as an initiator, and barbiturate as a promotor. Three groups were maintained through the course of the study: a) DEN treated maintained on barbiturate diet; b) untreated animals maintained on barbiturate diet; and c) controls.

In vivo imaging was performed serially over the course of 18 months using a 2T system dedicated to MR microscopy (G.E. NMR Instruments). Animals were anaesthetised using halothane in conjunction with scanned synchronous respiration (2). An acrylic carriage supported the animal and a series of relaxation standards. Images were acquired using two 16 slice 3DFT sequences: a) a CPMG sequence (TR=2 sec, TE=20, 40, 60, 80 ms); b) a single echo (TR=0.5 sec, TE= 20 ms). Slice thickness was 1.25 mm with in-plane resolution of 235 x 235  $\mu\text{m}$ .

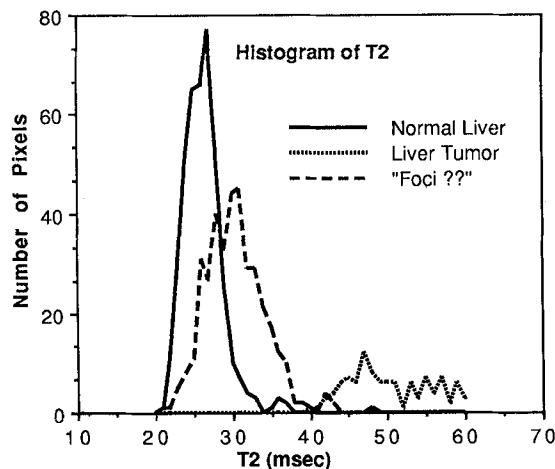
The set of 80 images/protocol permits pixel by pixel calculation of T1 and T2. The limited samples in TR and TE compel us to fit to simple expressions ( $1 - \exp(-\text{TR}/T_1)$ ) and  $N(H) \exp(-\text{TE}/T_2)$  for T1, T2 and N(H). Relaxation standards in each image allow verification of fit. Analysis is accomplished on Sun workstations linked via ethernet to the scanner. Data are stored on optical disk.

At fixed points animals were sacrificed and formalin fixed for histological examination. Tissue samples were also imaged using a second MR microscope operating at 7T. The increased SNR afforded by the higher field permits imaging with slices of 200  $\mu\text{m}$  with in-plane resolution of 20 x 20  $\mu\text{m}$ .

#### Results

Tissue heterogeneity was measured using histograms from the calculated images. Figure 1 demonstrates the effect of growing heterogeneity as the foci grow. The FWHM of the distribution in the T2 histogram of normal liver parenchyma is ~10 ms, not far from that of the standards. As tumors form, the T2 is shifted. The spread of the histogram clearly demonstrates the increased heterogeneity of the tumors. At intermediate stages where individual lesions are not

clearly visible, there is a subtle shift in the mean of the T2 histogram with a noticeable broadening.



#### Discussion

The in vivo studies here, with elements 1000 x smaller than those of early efforts, permit an improved measure of tissue heterogeneity. The nontrivial problems of animal support, pulse sequence development, and data handling have enabled us to develop an integrated system for further application of quantitative tissue characterization using in vivo MR microscopy.

#### References

- Herfkens, R., Davis, P., Crooks, L., et al. 1981. Radiology 141:211-219.
- Hedlund, L., Deitz, J., Nassar, R., et al. 1986. Invest. Radiol. 21:18-23.

Supported in part by NIEHS contract No. 273-86-I-0020 and NIH Grant No. 1 R01 ES04187.

## A Comprehensive T1 Measurement Protocol

Elliot McVeigh

The Johns Hopkins University School of Medicine

Introduction

We have developed a line-selective, multi-point inversion recovery (IR) protocol for volume localized multi-exponential T1 measurements.

Method

The method has two stages: first, a quick estimate of T1 in a localized region, second, a "many-point" IR sequence with an optimal distribution of T1 values.

A region of interest (ROI) is defined from the initial clinical protocol. A quick, one SHot IR T1 (SHIRT) estimate in the chosen region is obtained using the line projection pulse sequence shown in Figure 1. Three 1mm pre-inversion "slices" are applied at different TI delays, with 1.5mm gaps between them in the X direction. After slice selective excitation (Z), a line is selected through the ROI using an orthogonal gradient (Y) for the selective 180 degree refocussing pulse. The line is then projected using the X gradient. This sequence gives a profile of a 3-point IR curve which can be displayed at the console. An example of such a profile from a single projection of a 3x3mm line is shown in Figure 2. Using the non-inverted part of the projection as the baseline estimate, and the signal from the pre-inversion pulses as the IR data, a least-squares algorithm on a programmable calculator is used to fit T1 for the volume spanned by the pre-inversion slices. The volume can be as small as 5x3x3mm.

From this quick estimate of T1 in the ROI, the sampling of the many-point IR curve can be chosen to maximize the accuracy of the T1 estimate. The line selective many-point IR sequence uses a single broadband 180 degree pulse in place of the selective pre-inversion pulses, followed by the same line selective spin-echo sequence as used in SHIRT. The operator selects the series of T1 values used in the many-point IR experiment based on the quick estimate of T1. The IR curve can be sampled logarithmically, linearly, or in sections of different TI spacings. After a 1-dimensional Fourier transform in the X direction, the data is a set of IR curves for the voxels in the chosen line.

Conclusion

We have used this comprehensive T1 measurement protocol for measuring T1 values both *in vivo* and in phantoms. It is simple to use and has the added advantage that partial volume effects can be reduced by fitting multi-component exponentials to the many-point IR data.

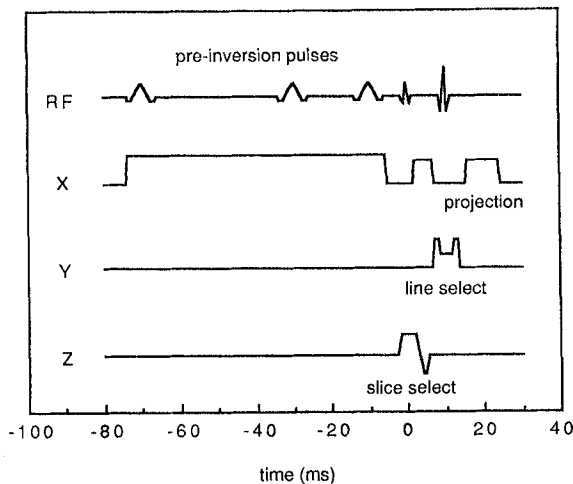


Figure 1. The SHIRT pulse sequence used to obtain the quick T1 estimate with the pre-inversion pulses.

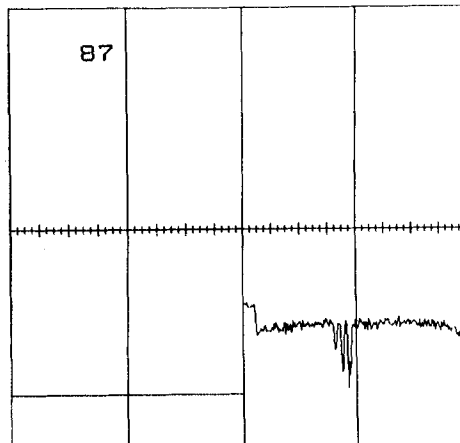
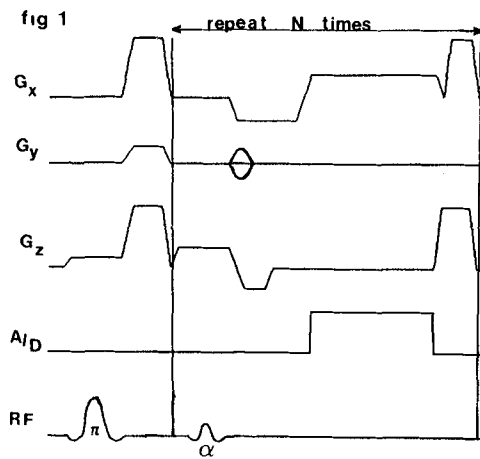


Figure 2. The data displayed using the SHIRT pulse sequence. The field of view for the projection is 80x3x3mm.

One-Shot  $T_1$  Imaging

I. Kay and R. M. Henkelman  
 Ontario Cancer Institute and Dept. of Medical Biophysics,  
 University of Toronto, Toronto, CANADA.

Spin lattice relaxation times ( $T_1$ ) are estimated in an imaging context using a "One Shot" method based on the pulse sequence proposed by Look and Locker<sup>1</sup> (fig.1). This sequence is significantly faster than inversion recovery (IR) methods for measuring  $T_1$ , and also has been shown in theory to be almost as efficient as the IR method<sup>2</sup>.



The technique produces an image for each  $\alpha$  pulse used. The intensity of each pixel in the set of images is described by the equation  
 $S_i = DR \exp(t_i/T_1^*) + \beta$  where  $DR$ ,  $\beta$ , and  $T_1^*$  are non-linear functions of the  $\alpha$  angle and the true value for  $T_1$ .  $T_1^*$  can be estimated by treating  $DR$ ,  $T_1^*$  and  $\beta$  as constants and then using a correction which depends on  $\alpha$ . Using a larger number of relatively smaller angle  $\alpha$ 's has several advantages: one obtains a better fit to the signal equation, the correction to find  $T_1$  is less prone to errors in  $\alpha$  and there is little penalty in the signal to noise ratio. We have shown that the method is robust despite imperfections in the limited tip angle ( $\alpha$ ) and initial 180° inversion pulses across the slice profile.

We have implemented this pulse sequence on a General Electric Sigma imager to acquire single slices and have worked towards optimizing its accuracy and utility. Up to 29 images having a 256 by 128 acquisition matrix with 2 excitation averaging can be produced in about 5 minutes. Subsequent analysis is presently carried out on separate workstations, but could in principle be done on a clinical machine. From these images of phantoms we can estimate a range of  $T_1$ 's to better than 10% in regions of interest.

This technique provides a rapid method for quantitative  $T_1$  measurements of pathological regions in patients. The large number of points that can be gathered along the recovery curve can also be used to investigate the possibility of multiexponential recovery in localized regions, which may be an indicator of pathology<sup>3</sup>. It can also serve as the basis for calculated  $T_1$  images, avoiding misregistration problems.

1. Look, D.C. and Locker, D.R. Rev. Sci. Instrum., 41, 250 (1970).
2. Crawley, A.P. and Henkelman, R.M. Magn. Reson. Med., 7, 23-34 (1988).
3. Kroeker, R.M. and Henkelman, R.M. J. Mag. Res., 69, 218 (1986).

## IMPROVED ACCURACY AND ACQUISITION TIME IN QUANTITATIVE T1 IMAGES

P.A.Gowland, M.O.Leach, and J.C.Sharp. The Joint Department of Physics, Royal Marsden Hospital and Institute of Cancer Research, Surrey, SM2 5PT, U.K.

INTRODUCTION

NMR imaging is being used to measure *in vivo* NMR relaxation times to aid the quantitative monitoring of tumour response to therapy. In order to carry out repeated measurements on patients, it is necessary to be able to perform scans as rapidly and as conveniently as possible. The interleaved saturation recovery/inversion recovery (SR/IR) sequence is a very efficient method of measuring T1 [1]. However it was found that results obtained with this sequence showed a systematic error of 7% using a long repetition time, which increased to 10% for a shorter repetition time [2]. It was considered likely that this error was due to the poor profile of the sinc inversion pulse, therefore the hyperbolic secant (HSC) pulse, which gives a much improved slice profile [3], was implemented in the sequence. The effect of this was investigated with simulations and experiments.

SIMULATIONS

Although the bandwidth of the SINC inversion pulse used was 2.4 times that of the 90° readout pulse, a simulation program based on the Bloch equations confirmed that the magnitude of the longitudinal magnetization created by this pulse varied by 20% over the frequencies read out by the 90° pulse. However if a HSC pulse of only twice the bandwidth of the 90° readout pulse was used, the magnitude of the longitudinal magnetization varied by less than 2% over the same region. This HSC pulse was implemented in the SR/IR sequence.

MEASUREMENTS

The measurements were carried out on a 1.5T Siemens Magnetom, using a calibrated set of Gadolinium doped agarose gel phantoms, with T1's ranging from 226 to 1621ms, obtained from the Hammersmith Hospital, London. When using short sequence timings it was necessary to use a phase correction technique to be able to take account of the phase reversal at the null point of recovery data, which is not detected on magnitude images. Instead of carrying out an

exact phase correction scheme, a simpler method, sufficient for this application, was used. The phase image associated with the SR image was subtracted from that associated with the IR image: the resulting image was flat, except at pixels where the spins had not yet recovered past the null point; these pixels had a 180° phase shift with respect to the rest of the image. The signal from the inversion image for these pixels was assigned to be negative before being referred to a look up table.

RESULTS

Figure 1 shows the results obtained with a long repetition time ( $Tr=4.0s$ ,  $Ti=1.3s$ ) for the SINC and the HSC pulse. The difference between the measured T1 and the calibrated T1 (averaged over all the samples with T1's longer than 500ms, and over 5 measurements) was reduced from 7% to 2%, by changing the SINC inversion pulse to a HSC pulse. The percentage standard deviation on the mean of the 5 measurements, averaged over all the samples with T1's longer than 500ms was 3%. Figure 2 shows that at a shorter repetition time ( $Tr=1.5s$ ,  $Ti=0.5s$ ) the difference between the measured T1 and the calibrated T1 (averaged over all samples with T1's greater than 300ms, for a single set of measurements) was reduced from 10% to 3% by replacing the sinc pulse with the HSC pulse.

CONCLUSION

The use of the hyperbolic secant pulse, with a suitable phase correction scheme, allows accurate and reproducible measurement of T1 with a reduced imaging time. The pulse would be expected to provide improved accuracy in multi-slice imaging.

REFERENCES

- 1 R.J.Kurland, Magn. Res. Med., 2, 136, 1985.
- 2 P.A.Gowland, M.O.Leach, and J.C.Sharp submitted to Magn. Res. Med. 1989.
- 3 M.S.Silver et al, J. Mag. Res., 59, 347, 1984.

ACKNOWLEDGEMENT

This work is supported by the Cancer Research Campaign.

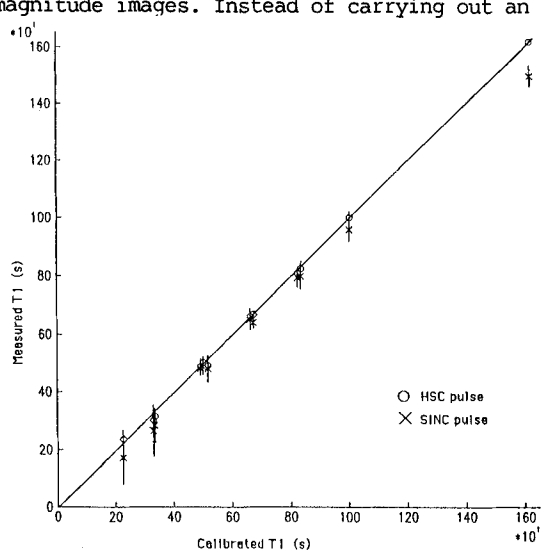


Figure 1 Results obtained using  $Tr=4s$ ,  $Ti=1.3s$ ; diagonal line is the line of identity.

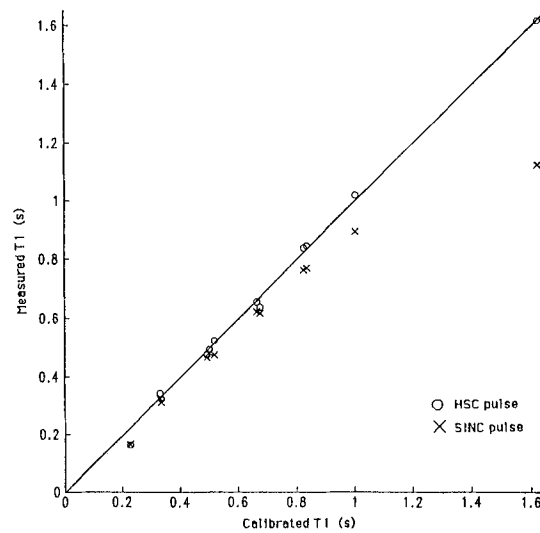


Figure 2 Results obtained using  $Tr=1.5s$ ,  $Ti=0.5s$ ; diagonal line is the line of identity.

## Quantitative Pixel Analysis with Surface Coil Imaging: $T_1$ - and $T_2$ -Relaxation and Diffusion

J. Gehrig, R. Bader, H.-J. Zabel and W.J. Lorenz  
German Cancer Research Center, 6900 Heidelberg, West Germany

### Introduction

The high signal-to-noise ratio (S/N) of surface coil imaging leads not only to high spatial and contrast resolution (1) but also to a sensitive method for the quantitative determination of the  $T_1$ - and  $T_2$ -relaxation and spin motion. The way to analyze these parameters from surface coil images with inhomogeneous intensity distribution (2) is demonstrated and the possibility to determine very exactly these parameters up to a distance of nearly the coil diameter will be shown. Within this region tissue characterization (3) and the calculation of spin diffusion (4) in respect to pathological states is improved.

### Method

The base for the parameter extraction are the signal intensities  $S(TE, TR)$  (5) and  $S(TE, G_z)$  (4,6) obtained with a 32 echo CPMG sequence (eq.1a) and a Pulsed Gradient Spin Echo sequence (PGSE) (eq.1b):

$$S(TE_n, TR) = S(0,0) \exp(-TE_n/T_2)(1-\exp(TR/T_1)) \quad \text{eq. 1a}$$

$$\begin{aligned} S(TE, G_z) &= S(0,0) \exp(-TE/T_2)(1-\exp(TR/T_1)) \\ &\quad \exp(-\gamma^2 \delta^2 G_z^2 (\Delta - \delta/3) D) \end{aligned} \quad \text{eq. 1b}$$

where for the CPMG sequence  $TE = 22/704$  msec,  $TR = 3$  sec and for the PGSE sequence  $TE = 120$  msec,  $TR = 2$  sec, amplitude of the pulsed gradient  $G_z = 0, 6,$  and  $8$  mT/m, the pulsed gradient duration  $\delta = 35$  msec, the pulsed gradient time interval  $\Delta = 72.12$  msec and  $\gamma$  is the gyromagnetic ratio. After homogeneous excitation and surface coil receiving the signal is modified by the varying field  $B_{1P}(z)$  the receiving characteristic of the coil. From a surface coil with a one turn loop of a radius  $r$ , the field  $B_{1P}(z)$  at point  $P$  on the coil axis (fig.1) is calculated by Biot and Savart's law as (eq.2):

$$B_{1P}(z) = kr^2/(r^2+z^2)^{3/2} \quad \text{eq. 2}$$

where  $k$  is a constant and the coordinates are referred to the origin at the center of the coil (7). So the signal (eq.1a+b) received by a surface coil is given by (eq.3a+b):

$$\begin{aligned} S(TE, TR) &= B_{1P}(z) S(0,0) \exp(-TE/T_2) \\ &\quad (1-\exp(TR/T_1)) \end{aligned} \quad \text{eq. 3a}$$

$$\begin{aligned} S(TE, G_z) &= B_{1P}(z) \exp(-TE/T_2) \\ &\quad (1-\exp(TR/T_1)) \exp(-\gamma^2 \delta^2 G_z^2 (\Delta - \delta/3) D) \end{aligned} \quad \text{eq. 3b}$$

Finally, the desired parameters are calculated by an exponential fitting of these signals.

### Results

This method results in an uniform image without reduction in signal intensity from the coil center up to a distance equal the coil diameter. In respect to body or head resonators the contrast resolution or image quality is higher and the simultaneously obtained  $T_1$ -,  $T_2$ -values and the determined diffusion coefficients are identical in the same regions. Usually the noiselevel of a surface coil image is reduced by a factor 4 or more (Tab.1), depending on the coil load and the zoom factor or field of view. Therefore the  $T_2$  calculation can be extended to later echoes even if the relaxation time is short. For a probe of agarose gel, doped with Gadolinium a  $T_2$  time of 90 msec was measured. In this case five additional

echoes are available for calculation compared to measurements with the head resonator.

Tab.1: Noise and noiselevel for different antenna types

Antenna	Noise	Noiselevel
Bodyresonator	71	146
Head resonator	46	96
Surface coil	14.5	29

A selfdiffusion coefficient of  $2.3 \times 10^{-9}$  m<sup>2</sup>/sec results for a probe of water at 21°C being positioned in a distance of 3 cm from the center of a surface coil with 7.5 cm in diameter.

### Conclusion

For the diagnosis and tissue characterization of superficial tissues and extremities surface coils can applied with higher efficiency for parameter extraction than with body resonators receiving. For minimizing the motion artifacts caused by blood pulsation, the PGSE sequences only should used with ECG triggering.

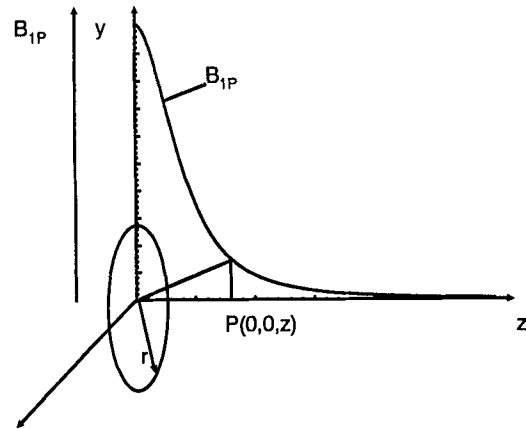


Fig.1: The field  $B_{1P}(z)$  of a one turn loop of the radius  $r$  at a point  $P$  on the coil  $z$  axis.

### References

1. Zabel, H.-J., R. Bader, J. Gehrig, W.J. Lorenz. *Radiology*, 165, 857, 1987.
2. Gehrig, J., R. Bader, H.-J. Zabel, W.J. Lorenz. In: Book of abstract: Society of Magnetic Resonance in Medicine, Berkeley, Calif., 2, 969, 1988.
3. Brix, G., L. Schad, I. Zuna, private communications
4. Le Bihan, D., E. Breton, D. Lallemand, P. Grenier, E. Cabanis, M. Laval-Jeantet. *Radiology*, 161, 401, 1986
5. Gore, J. C. In: Nuclear Magnetic Resonance and Correlative Imaging Modalities: The Society of Nuclear Medicine, C. Leon Partain (ed.), New York, 75, 1984
6. Stejskal, E.O., J.E. Tanner. *J. Chem. Phys.*, 42, 288, 1965
7. Young, I.R. In: Practical MR Imaging, M.A. Foster and JMS Hutchison (eds.), IRL Press, Oxford, 199, 1987

in vivo  $^{31}\text{P}$  CPMG  $T_2$  MEASUREMENTS IN RAT BRAIN WITH SURFACE COILS

A. Ziegler, J.P. Albrand, C. Rémy\*, and M. Décorps

Centre d'Etudes Nucléaires de Grenoble, DRF/Service de Physique/RMBM, 85 X, 38041 GRENOBLE FRANCE  
\*INSERM U 318, LMCEC, Faculté de Médecine de Grenoble, 38700 - LA TRONCHE FRANCEIntroduction

Transverse relaxation time measurement by the Carr-Purcell-Meiboom-Gill (CPMG) technique can provide useful informations about molecular motions, spin-spin coupling, chemical exchange etc... However it is known that nonideal refocusing pulses can introduce strong errors in spin-spin relaxation time measurements. In this study, we describe a pulse sequence which allows to overcome such a problem. The method is applied to  $^{31}\text{P}$  NMR  $T_2$  measurement with a surface coil, of Phosphocreatine in rat brain.

Methods

In the inhomogeneous rf field of surface coils, the CPMG pulse sequence can be written as:

$$\theta_x - (\tau - 2\theta_y - \tau)^N - \text{ACQ} \quad [1]$$

A drawback of the sequence is that the excitation pulse leaves some longitudinal magnetization along the z-axis. The subsequent  $2\theta_y$  pulses tip a part of this residual magnetization along the x axis ; such a component cannot be properly refocused and is a source of errors. This problem can be circumvented by using the following modification of the pulse sequence :

$$\text{SR} - [2\theta]_{\pm x} - \theta_x - [2\theta]_{\text{EX}} - (\tau - 2\theta_y - \tau)^N - \text{ACQ} \quad [2]$$

where EX means an Exorcycle phase-cycling. SR is a saturation recovery period which avoids the use of long recycle delays which are needed for efficient phase cycling. An analysis of the effects of this sequence can be made by using the cycle matrix formalism (1) and taking into account  $T_1$  and  $T_2$  relaxation during the free precession delays  $\tau$ . First of all the use of the  $[2\theta]_{\pm x}$  preparation pulse and of the  $[2\theta]_{\text{EX}}$  refocusing pulse give to the sequence some spatial selectivity (1) and thus reduce the sensitive region and hence the rf inhomogeneity in this region. Secondly, the  $[2\theta]_{\text{EX}}$  refocusing pulse suppresses any contribution to the acquired signal from the residual longitudinal magnetization after the excitation pulse. Finally due to the add-subtract phase cycling in the Exorcycle scheme, it can be shown that relaxation effects during the  $\tau$  delays can be simply described by applying a relaxation matrix:

$$\begin{vmatrix} R_2 & 0 & 0 \\ 0 & R_2 & 0 \\ 0 & 0 & R_1 \end{vmatrix}$$

where  $R_1 = \exp - \tau / T_1$  and  $R_2 = \exp - \tau / T_2$ . Thus, due to the phase cycling, spin lattice relaxation acts on longitudinal components like the spin spin relaxation on the transverse ones.

Results

Computer simulation of CPMG  $T_2$  measurements using pulse sequence [2] with non ideal pulse angles shows that  $T_2$  measurement accurate to  $\sim 5\%$  can be achieved in the entire range of pulse angles if  $\Delta\tau \ll 1$ , where  $\Delta = f_0 - f$  is the off-resonance offset, even if  $T_2 \ll T_1$  which can be the case for biological samples. To corroborate these results NMR experiments were performed using a doped water phantom in the homogeneous rf field of a standard saddle coil probe with various pulse angles and in the inhomogeneous rf field of a surface coil. These experiments showed that measured values of  $T_2$  did not differ from  $T_2$  values obtained with small samples in an homogeneous radiofrequency field by more 5%.

Finally  $^{31}\text{P}$  NMR,  $T_2$  measurements of Phosphocreatine in rat brain were made and compared to the spin spin relaxation times obtained by using a 2 pulses Carr-Purcell sequence:

$$\theta_x - T_e - [2\theta]_{\text{EX}} - T_e - \text{ACQ} \quad [3]$$

and increasing the spin echo delay  $T_e$ .  $T_2$  measured using the CPMG technique (pulse sequence [2]) was found equal to about 240 ms. This is significantly longer than the value obtained with the CP sequence ( $\approx 170$  ms). In the range  $0.5 \text{ ms} \leq \tau \leq 2 \text{ ms}$  the CPMG  $T_2$  value was found independent of the  $\tau$  value. Therefore the difference observed in  $T_2$  values between the CP and CPMG experiments is not due to spin locking effects (2). These differences could be due to chemical exchange or to diffusion through intracellular magnetic field heterogeneities.

Conclusions

This study is the first demonstration that accurate CPMG measurements can be carried out in the strongly inhomogeneous rf field of surface coils.

References

1. Bendall M.R. and Pegg D.T. *Magn. Reson. Med.*, 2, 91, 1985.
1. Santer G.E., Henkelman R.M. and Bronskill M.J. *J. Magn. Reson.*, 79, 28, 1988.

<sup>31</sup>P magnetic relaxation of adenosine 5'-monophosphate,  
adenosine 5'-diphosphate and adenosine 5'-triphosphate in solution

E.R. Andrew, W.S. Brey, R. Gaspar, and A. Qiu  
Departments of Physics, Chemistry, Radiology and Nuclear Engineering Sciences  
University of Florida, Gainesville, Florida 32611 U.S.A.

**Introduction.** In vivo NMR spectroscopy continues to provide important information concerning the metabolism of tissues and organs in normal and diseased states. Although the NMR spectra of metabolites have been well investigated few measurements have been made of their relaxation times and basic relaxation mechanisms are not well understood. A good understanding of relaxation is needed in quantitation of spectra in presence of partial saturation, in saturation transfer experiments, and in studies of molecular mobility and exchange. We have therefore made a basic investigation of <sup>31</sup>P relaxation behaviour of the metabolites AMP, ADP and ATP in solution over a range of temperatures and at different magnetic field strengths as a first step in the elucidation of relaxation mechanisms in these compounds from which an understanding in vivo can later be developed. The work follows our previous investigation of <sup>1</sup>H relaxation in these compounds (1,2).

**Methods.** <sup>31</sup>P relaxation times  $T_1$  were measured for the individual phosphorus resonances from 278K to 333K at 121.5 MHz (Nicolet NT-300) and 40.5 MHz (Varian XL-100). Samples were 0.02-0.1 M solutions in pure H<sub>2</sub>O from which dissolved oxygen was removed and relaxation by paramagnetic ions suppressed by 5mM CDTA (1) and pH adjusted to 7.4.  $T_1$  was measured using an inversion recovery pulse sequence; all recoveries were exponential within experimental error.

**Results and Discussion.** As examples, measured  $T_1$  values at 121.5 MHz and 310K are given in Table 1 for the individual <sup>31</sup>P resonances in the three compounds. Values of  $T_1$  at 40.5 MHz were roughly double, indicating a strong relaxation contribution from the chemical shift anisotropy (CSA) mechanism.  $T_1$  was found to be independent of concentration over the range 0.02-0.1M. For all six resonance lines  $T_1$  increased monotonically with increase of temperature by a factor 3 to 4 times over the range 278 to 333K. Activation plots of  $\log T_1$  against inverse temperatures were closely linear for all six resonances. This implies molecular motions characterized by correlation times  $\tau_c$  in the fast motion limit,  $\omega_0 \tau_c \ll 1$ , and excludes the spin-rotation interaction mechanism which would have an opposite temperature dependence. Scalar relaxation of the second kind to adenosine protons is estimated to be negligibly small on the basis of known coupling constants and our proton  $T_1$  values (1,2). Relaxation due to paramagnetic impurities was minimized by careful sample preparation (1).

We are left then with two dominant relaxation mechanisms, namely dipolar and CSA; for both the relaxation rate in the fast motion limit is proportional to  $\tau_c$ . Only the CSA contribution is frequency-dependent and from the measurements at the two frequencies the two contributions are separated. The fractional CSA contributions for all six resonances are shown in Table 2 and are consistent with published values of shift anisotropy (3).

The dipolar relaxation arises mainly from interactions of <sup>31</sup>P nuclei with adenosine protons, particularly H<sub>4'</sub>, H<sub>5'</sub>, as well as solvent water protons and with intramolecular <sup>31</sup>P nuclei, but not with intermolecular <sup>31</sup>P nuclei in view of the lack of concentration dependence of  $T_1$ .

The values of  $E_A$  in Table 3 fall in the close range 17.1-20.0 kJ/mole and are similar to those found from analysis of proton  $T_1$  measurements (1,2). This suggests that torsional motion around the C<sub>4'</sub>-C<sub>5'</sub> bond, important for securing proton relaxation is also important for <sup>31</sup>P relaxation. The outermost <sup>31</sup>P nuclei have slightly lower  $E_A$  values indicating greater freedom of the outer groups and consistent with the lower proportion of CSA contribution for these groups in Table 2.

This work was supported by NIH grants CA 42283, RR 02278.

**References.**

1. Andrew, E.R., Gaspar, R. Chem. Phys. Letters 146, 184, 1988.
2. Andrew, E.R., Gaspar, R. Chem. Phys. Letters 147, 441, 1988.
3. Brauer, M., Sykes, B.D. Biochem. 20, 6767, 1981.

Table 1.  $T_1$ (s) at 121.5 MHz, 310K

	$P_\alpha$	$P_\beta$	$P_\gamma$
AMP	5.7		
ADP	3.9	6.3	
ATP	3.0	4.4	6.0

Table 2. CSA relaxation contribution(%)

	$P_\alpha$	$P_\beta$	$P_\gamma$
AMP	121.5	51	
	40.5	11	
ADP	121.5	53	25
	40.5	11	4
ATP	121.5	59	68
	40.5	14	19
			34
			5

Table 3. Activation Energy  $E_A$  (kJ/mole)

	$P_\alpha$	$P_\beta$	$P_\gamma$
AMP	17.1		
ADP	20.0	17.1	
ATP	19.6	19.2	17.7

**A New Method For Combined  $T_1$ -Measurement And Multi-Exponential  
 $T_2$ -Analysis In Tissue Characterizing MRI**

Manfred Eis<sup>+</sup>, Heinz Handels<sup>†</sup>, Klaus Bohndorf<sup>o</sup>, Matthias Drobnytzky<sup>o</sup>, Thomas Tolxdorff<sup>†</sup> and Achim Stargardt<sup>o</sup>

<sup>†</sup>Institut für Medizinische Statistik und Dokumentation <sup>o</sup>Klinik für Radiologische Diagnostik  
Klinikum der Rheinisch-Westfälischen Technischen Hochschule Aachen (RWTH), D-5100 Aachen, West-Germany

Purpose

A new method for combined  $T_1$  and  $T_2$  measurements has been developed to support tissue characterization with MRI in the clinical routine. In order to reduce the measurement time and to preserve the necessary accuracy for relaxation time evaluation with the possibility of multi-slice imaging the pulse sequence parameters have been optimized. The accurate description of the magnetization decay by alternating application of rotation and relaxation matrices allows both the evaluation of  $T_1$  based on four independent parameter estimates and the realization of a multi-exponential  $T_2$ -analysis according to 28 echoes.

Introduction

Employing modified CPGM-sequences with 32 echoes a second excitation pulse is transmitted into the system after an additional recovery interval  $TR_{2\text{eff}}$  which follows the 28th refocusing pulse (see fig. 1). The theoretical model describing the signal dependency on  $T_1$ ,  $\alpha$ ,  $\beta$ ,  $TR_{1\text{eff}}$ ,  $TR_{2\text{eff}}$  and  $T$  ( $\alpha$ : excitation pulse angle;  $\beta$ : refocusing pulse angle;  $T := TE/2$ ) uses an alternating application of rotation (RO) and relaxation (RE) matrices :

$$\underline{M}(t) = \dots \text{RE}(T) \downarrow \text{RO}(\beta) \text{RE}(T) \downarrow \text{RO}(\alpha) \underline{M}(0)$$

Using this formalism, the effects of  $T_1$ -relaxation between successive echoes are taken into account. Furthermore the magnetization values are computed immediately before the two excitations take place considering the oscillation of the spin-system into an asymptotic equilibrium state during the 'preparing scans' of the sequence. These results are regarded as constant starting values of the magnetization for the subsequent data scans.

Methods

Knowing the magnetization vector of a spin-ensemble at a given time the projection of  $\underline{M}(t)$  onto the measurement plane  $x'y'$  superimposed by the dephasing effect due to  $T_2$ -relaxation yields the corresponding NMR-signal  $S(t)$ . To determine  $T_1$  the theoretical signal ratios

$$Q_{i\text{TH}}(T_1) := S_i / S_{i+28} \quad (i = 1, \dots, 4)$$

are computed (assuming perfect pulse angles) and stored in four look up-tables (LUT's) eliminating the multi-exponential  $T_2$ -dependence. Before calculating  $T_1$  our data preprocessing subjects all measured signals to a noise treatment [1].

In the following a binary search algorithm scanning the four LUT's yields the  $T_{1i}$  that show the best accordance between the measured  $Q_{i\text{MEAS}}$  and the theoretically predicted  $Q_{i\text{TH}}$ . After this the mean of the four  $T_{1i}$  is regarded as result of the  $T_1$ -evaluation. Finally a multi-exponential  $T_2$ -analysis is done with a nonlinear optimization algorithm implemented in RAMSES (RWTH Aachen Magnetic resonance Software System) [2].

Results

Using  $256^2$ -matrices and a fixed repetition loop ( $n=2$ ) the whole data set for the  $T_1$  and  $T_2$ -determination takes about 33 minutes to be acquired ( $TR_{1\text{eff}} = 3000$  ms,  $TR_{2\text{eff}} = 300$  ms). The influence of noise and the standard deviation of  $T_1$ -estimates are reduced because the combination of the pulse sequence and the computation formalism allows to determine  $T_1$  based on four different signal ratios.  $T_1$ -images computed with this method show much better quality with more reliable relaxation time values than images using only one signal ratio and the simple SR-approximation, implemented in most MRI systems. Due to the use of fast algorithms the computation time needed for the  $T_1$ -determination is very short so that the generation of a  $T_1$ -image can be performed in about 2 minutes.

Conclusion

The described method yields the relaxation parameter  $T_1$  and multi-exponential  $T_2$ -values with only one measurement, thus using the input data set acquired in the sparsely available measurement time of the clinical routine in a very efficient manner. Multi-slice imaging is principally possible although limitations on the number of obtainable slices are imposed by the rawdata storage capacity of the MR-system and the chosen combination of  $TR_1/TR_{2\text{eff}}$ . Attempts of tissue characterization with imaging methods are improved because of the gained accuracy and reliability based on the nearly complete tissue parameter set.

References

- [1] Handels, H., Tolxdorff, T., Bohndorf, K., *Proceedings of the International Symposium on Tissue Characterization in MRI*, Wiesbaden, (IN PRESS)
- [2] Felberg, L., Tolxdorff, T., Gersonde, K., 5th Annual Meeting of the Society of Magnetic Resonance in Medicine, Montreal, Abstr. Vol. 2, 518, 1986

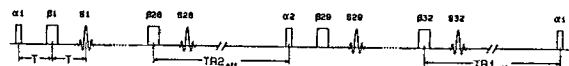


Fig. 1: timing of the studied pulse sequence

## COMPUTATION OF HIGH QUALITY T<sub>1</sub> IMAGES USING A TOMROP SEQUENCE

Gunnar Brix, Lothar R. Schad, Michael Deimling, Walter J. Lorenz  
 Institute of Radiology and Pathophysiology, German Cancer Research Center, Heidelberg, FRG,  
 and Siemens AG, Medical Division, Erlangen, FRG

### Purpose

The evaluation of high quality T<sub>1</sub> images is an important prerequisite for tissue characterization and texture analysis. In clinical practice T<sub>1</sub> images are usually obtained from two MR images acquired with different repetition times. However, the quality of the resulting T<sub>1</sub> images is poor. This study was undertaken to compute the longitudinal relaxation time T<sub>1</sub> pixelwise from a series of gradient echo images measured with a fast TOMROP sequence<sup>1</sup>, first proposed by Look and Locker<sup>2</sup>.

### Methods

The measurements have been performed on a 1.5 T whole body MR imager (MAGNETOM, Siemens). The pulse train of the TOMROP sequence is sketched in Figure 1. Using the abbreviations c=cosβ, s=sinβ, E<sub>1</sub>=exp(-T<sub>1</sub><sub>1</sub>/T<sub>1</sub>), E<sub>2</sub>=exp(-T<sub>1</sub><sub>2</sub>/T<sub>1</sub>), E<sub>r</sub>=exp(-t<sub>r</sub>/T<sub>1</sub>), and F=(1-E<sub>2</sub>)/(1-cE<sub>2</sub>) the steady state signal S<sub>n</sub> of the n-th image (1≤n≤N) is given by the signal equation:

$$S_n = | s A [ F + (c E_2)^{n-1} (G - F) ] | ,$$

with

$$G = \frac{F c E_r E_1 [1 - (c E_2)^{N-1}] + E_1 (1 - E_r) + E_1 - 1}{1 + (c E_2)^{N-1} c E_r E_1}$$

From this signal equation the three free parameters T<sub>1</sub>, β and A were calculated for each pixel using the iterative Marquart algorithm for least squares estimation of non-linear parameters<sup>3</sup>.

### Results

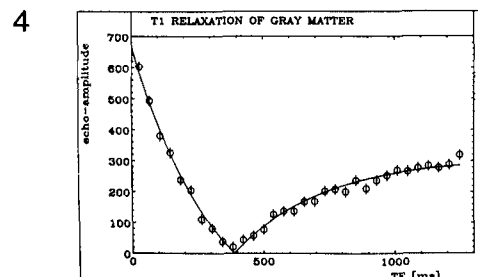
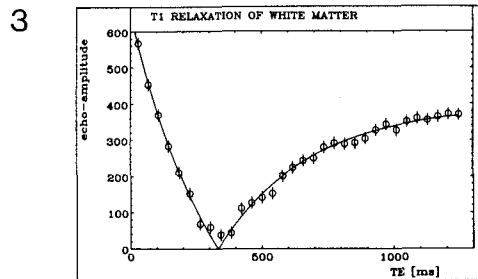
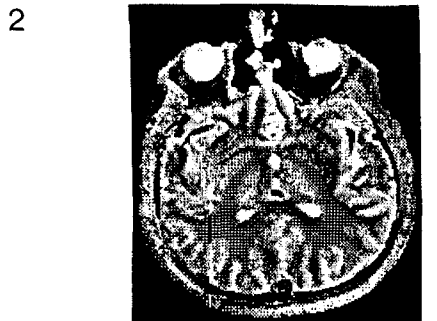
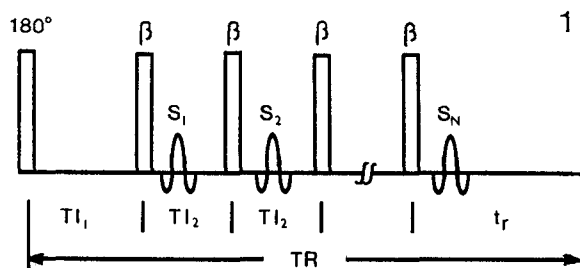
The computer time for the approach discussed was about 10 min on a MicroVAX 3600 for a typical head image with a matrix size of 256 x 256 pixels. Figure 2 shows the T<sub>1</sub> image of a human brain, which were computed from 32 gradient echos (T<sub>1</sub><sub>1</sub>=30 ms, T<sub>1</sub><sub>2</sub>=40 ms, TR=2000 ms, β=20°). As typical examples the relaxation curves of two pixels, one in the white and one in the gray matter, are shown in Figures 3 and 4. The computation yielded T<sub>1</sub> values of 542 ± 9 ms and 962 ± 13 ms respectively.

### Conclusion

In contrast to the usual "two point" T<sub>1</sub> images the T<sub>1</sub> images computed from a gradient echo series created by a TOMROP sequence show an excellent quality, which is comparable to T<sub>2</sub> images calculated from a multi-echo sequence.

### References

1. Graumann R, Deimling M, Heilmann T, Oppelt A: A new method for fast and precise T<sub>1</sub> determination. SMRM 1986, Book of Abstracts, 922-923
2. Look DC, Locker DR: Time saving in measurements of NMR and EPR relaxation times. Rev. Sci. Instrum. 1970, 41:250-251.
3. Marquart DW: An algorithm for least squares estimation of non-linear parameters. J. Soc. Industr. Appl. Math. 1963, 11:431-441



Compatibility of the Two-site Exchange Model  
and  $^1\text{H}$  NMR Relaxation Rates

R.V. Mulkern, A.R. Bleier, T. Sandor, F.A. Jolesz  
Dept. of Radiology, Brigham and Women's Hospital

The two-site exchange model (1) is widely used for qualitative interpretations of relaxation behaviour in tissue (2). However, its use to quantitatively evaluate exchange parameters has been largely confined to paramagnetically doped whole blood studies (3) where measurements of relaxation rates in both intra and extra cellular spaces of whole blood may be made independently. This permits a direct conversion of relaxation data into two-site exchange model parameters.

We have recently demonstrated a method for extracting exchange parameters in blood which does not require the physical separation of compartments (4). Biexponential decompositions of transverse decay curves at two paramagnetic doping levels permit a direct conversion of relaxation data into two-site exchange parameters. Here, we demonstrate that biexponential decomposition of both the longitudinal magnetization and the transverse magnetization also permit a similar conversion (5). We apply the analysis to published data sets of  $^1\text{H}$  relaxation behaviour in mycelia of *Botrytis cinerea* Persoon (a common fungus) and pupae of tobacco cutworm. Physically acceptable exchange parameters are found, demonstrating the compatibility of the relaxation data with the two-site exchange model.

Relaxation decay curves have been fit to normalized biexponential functions in these systems (6):

$$\begin{aligned} S_2 &= a \exp(-R_{2a}t) + (1-a)\exp(-R_{2b}t) & [1] \\ S_1 &= d \exp(-R_{1a}t) + (1-d)\exp(-R_{1b}t) & [2] \end{aligned}$$

$S_2$  and  $S_1$  are signal decays (or restoration) of transverse and longitudinal magnetization, respectively. "Apparent" volume fractions and relaxation rates,  $a$ ,  $d$ ,  $R_{2a}$ ,  $R_{2b}$ ,  $R_{1a}$ , and  $R_{1b}$  provide the raw data from which two-site exchange parameters may be extracted. The non-linear inversion, though analytic, is too lengthy to report here but has been discussed in detail (4,5). Two-site exchange model parameters are the real volume fractions of exchangeable water  $f$  and  $g$  ( $f+g=1$ ), the exchange rates between fractions  $k_{fg}$  and  $k_{gf}$  ( $fk_{fg}-gk_{gf}=0$ ), and the intrinsic transverse and longitudinal relaxation rates  $R_{2f}$ ,  $R_{2g}$ ,  $R_{1f}$ , and  $R_{1g}$  in each fraction (those present in the absence of exchange). Table 1 lists the experimental relaxation data and Table 2 lists the two-site exchange model parameters derived from this data.

	$a$	$R_{2a}$	$R_{2b}$	$d$	$R_{1a}$	$R_{1b}$
<i>B. Cinerea</i>	0.17	48	16	0.08	6.2	1.6
Cutworm	0.26	35	8	0.12	3.9	1.3

Table 1: Biexponential parameters reported by Yoshida and Nose. Relaxation rates are in Hz.

	$f$	$k_{fg}$	$R_{2f}$	$R_{2g}$	$R_{1f}$	$R_{1g}$
<i>B. Cinerea</i>	0.19	1.5	46	15	4.6	1.4
Cutworm	0.28	0.8	34	8	3.0	1.1

Table 2: Two-site exchange model parameters derived from the data in Table 1. Exchange rates and intrinsic relaxation rates are in Hz.

Protons associated with the smaller fraction  $f$ , have larger transverse and longitudinal relaxation rates in both of these systems (Table 2). These protons presumably form the "bound" water fraction with less rotational and/or translational freedom than those in the "free" water fraction. The average lifetime of a proton in the bound fractions ( $k_{fg}^{-1}$ ) is 666 ms and 1250 ms for *B. cinerea* and the cutworm pupae respectively.

Water exchange between different environments in homogeneous tissue specimens influences observed relaxation rates. The extent to which this feature may be used to extract exchange parameters depends upon quantitative analyses of relaxation data. We have developed such analyses (4,5) based on the two-site exchange model. When exchange rates are on the order of the intrinsic relaxation rates - the so called intermediate exchange regime - biexponential functions characterize the decay curves (1). We have demonstrated that the biexponential parameters may be directly converted into two-site exchange model parameters. Obtaining physically acceptable exchange parameters implies that two-site exchange is compatible with the relaxation data. Values extracted may be compared with predictions based on either a biological or physical model of water compartmentation. Failure of the analysis to yield physically acceptable exchange parameters (eg. negative exchange rates) implies that more sophisticated models are required to describe the relaxation behaviour. The ability to quantitatively assess exchange parameters is an important first step in understanding the true nature of water compartmentation in tissue. We have provided a method for doing so within the framework of two-site exchange and NMR relaxation data.

- Zimmerman, J.R., W.E. Britton, *J. Phys. Chem.* **61**, 1328, 1957.
- Bottomley, P.A., et al. *Med. Phys.* **11**, 425, 1984.
- Pirckle, J.L., et al. *Biophys. J.* **25**, 389, 1979.
- Mulkern, R.V. et al. *Biophys. J.* **55**, 221, 1989.
- Mulkern, R.V. et al. Submitted for Publication, *Magn. Reson. Med.*
- Yoshida, M., K. Nose, *Agric. Biol. Chem.* **51**, 3399, 1987.

## Cross Relaxation and Restricted Diffusion in Polyacrylamide Gels and Amino Acids

Jianhui Zhong, John C. Gore and Ian M. Armitage<sup>†</sup>

Depts. of Diag. Radiol. and <sup>†</sup>Mol. Biophys. & Biochem., Yale Med. School, New Haven, CT 06510

### Introduction

To further our understanding of proton relaxation in tissues we report measurements of NMR relaxation times and restricted diffusion in model systems. Polyacrylamide gels, their requisite components and several amino acids were studied at different pH and different deuteration conditions. The results give detailed information on changes of structure as the solvent pH value varies and on the influence of polymerization on relaxation times. Attempts have been made to quantitate different mechanisms responsible for  $T_1$  and  $T_2$  relaxation processes, and to correlate the results with possible related mechanisms in tissues.

### Methods and Analysis

Polyacrylamide gel (PAG) samples of 50mg/ml were made and soaked in a large volume of solvent with pH 1-10 and different  $H_2O/D_2O$  ratios. NMR relaxation times  $T_1$  and  $T_2$  were measured at 20 MHz using inversion-recovery and CPMG sequences respectively. Solutions of each gel component, acrylamide, crosslinking agent *N,N'*-methylenebisacrylamide (Bis), as well as several amino acids (Lys, Gln, Asn) were examined.

$T_1, T_2$  measurements showed that in all the solutions the  $T_1$  remains approximately constant at all the pH values, but the  $T_2$  for the solutions containing ionizable groups (all except Lys) sharply increases around pH2, stays high for pH 2-9, and then decreases at pH10. This may be explained in terms of the ionization of  $NH_2$  in the amide group at different pH. There is a fast chemical exchange present at all pH values, as seen by the variation of  $T_2$  with interpulse interval in CPMG sequences. Gels also show the existence of a similar chemical exchange process, but also demonstrate a close correlation between  $T_1$  and  $T_2$  variations: at pH around 3.5 and up to pH10 both  $T_1$  and  $T_2$  are reduced in magnitude by more than 30%. Data for gels soaked in 100% protonated solvent are shown in Fig.1. The results suggest that there exists a process in gels that facilitates both  $T_1$  and  $T_2$  relaxation that is not present or is zero averaged in the monomer. Control pH reverse studies showed that gels with pH lower than 3.5 have elevated  $T_1$  and  $T_2$  regardless of previous pH history.

Previous studies have suggested that water molecules in macromolecular systems can be divided into a fraction that is closely associated with macromolecules ("bound") and has shorter  $T_1, T_2$  due largely to cross relaxation with macromolecular protons and a fraction of "free water", with fast exchanges causing an overall reduction in  $T_1$  or  $T_2$ . We directly measured the fraction of non-freezing water by subjecting gels to temperature below -40°C and measuring the water peak area compared with that at room temperature. The results indicate a higher fraction of unfrozen water for gels with pH higher than 3.5. Curve fitting of  $R_2 (= 1/T_2)$  vs the interpulse interval according to the fast chemical exchange model of Luz and Meiboom(1) also shows that all quantities proportional to the bound water fraction jump at pH=3.5 by more than 30%. The study of  $T_1$  vs  $H_2O/D_2O$  suggested that the  $T_1$  differences for gels of high and low pH is largely due to the difference in their cross relaxation rate, which is also proportional to the bound water fraction. We used scanning electron microscopy (SEM) to measure the pore sizes in gels of different pH, and the results suggest that in all the gels the pore size is smaller than 0.1  $\mu m$ . Using the typical residence time of the bound water of 10ms, the average free path length for a water molecule is of the order of 5  $\mu m$ . The water diffusion in gels is therefore restricted. The diffusion coefficients  $D$  of gels were measured on a 2T CSI system with a home-built gradient coil of max-

imum gradient strength  $\sim 40G/cm$ . It was verified that the effect of possible internal gradients are negligible compared with the external gradient. In Fig.2  $D$  is plotted against duration between the pulsed gradient for PAG of pH2 and pH6, and for distilled water. It is clear that gels have lower  $D$  than water, and the smaller  $D$  with longer diffusing time indicates a more restricted diffusion. Assuming water diffuses in spherical barriers, it can be estimated(2) that the radius for pH2 gel is 1.3 times that of the pH6 gel.

### Conclusion

The observed simultaneous  $T_1$  and  $T_2$  changes in gels correspond to a change in gel pore size and a resultant change in the effective bound water fraction: gels with smaller pores have shorter  $T_1, T_2$  since they apparently have a larger fraction of bound water. Each pore has a larger surface/volume ratio and there are more frequent interactions of water with the gel matrix. The results suggest that relaxation changes can occur without alterations in molecular tumbling, water content or molecular weight. These studies provide insight into understanding the differences between the properties of macromolecules in solutions and those of tissue matrix.

(1) Z.Luz and S.Meiboom, *J. Chem. Phys.*, **39**, 366 (1963).

(2) J.E.Tanner and E.O.Stejskal, *J. Chem. Phys.*, **49**, 366 (1968).

Fig.1

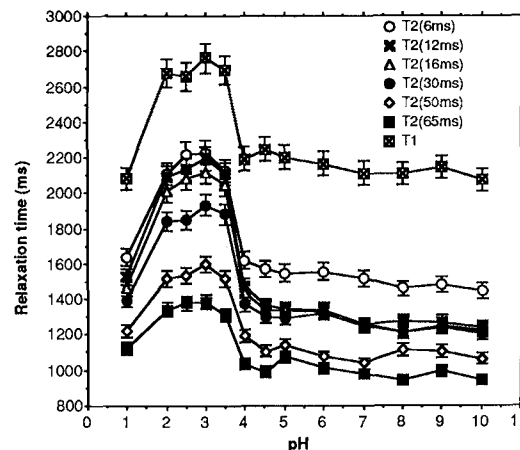
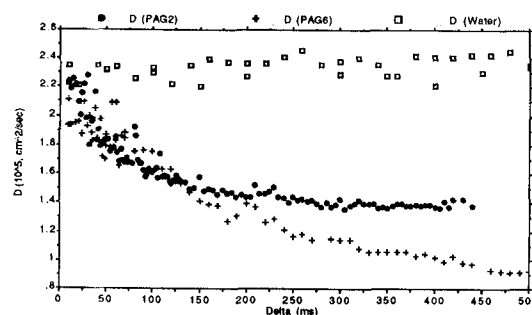


Fig.2



**Effects of Extracellular Space and Protein Content on Water Proton Relaxation Rates in a Model Tissue System**

R.S. Menon, M.S. Rusinko and P.S. Allen

Department of Applied Sciences in Medicine

University of Alberta, Edmonton, Alberta, CANADA T6G 2G3

**Introduction**

The various relaxation rates of water protons in heterogeneous tissue provide a very sensitive means of manipulating tissue contrast in an NMR image. The changes in these rates that occur as a result of pathology can provide valuable diagnostic information. A fundamental understanding of relaxation mechanisms in tissue will undoubtedly improve the potential of NMR imaging as a quantitative, specific, diagnostic modality.

Water proton relaxation measurements of tissue *in-vitro* and *in-vivo* have proven difficult to interpret, especially with regards to mechanisms that can generate multiexponential relaxation decays. We have chosen to investigate tissue water proton relaxation by building on a series of increasingly complex model systems. Previous work on the simplest such system, aqueous protein solutions, has allowed us to quantify changes in relaxation rates as a function of protein size, shape and concentration (1-3). The next level of sophistication has been to incorporate a membrane to form a quasi-cellular system, which we have by employing intact red blood cell (RBC) ghosts (3,4). Preparations of these ghosts allowed us to evaluate changes in water proton relaxation rates; (1) as the ratio of intra to extracellular water is varied, (2) as the amount of protein in the extracellular environment is increased and (3) as the degree of compartmentalization of the preparation is varied from microscopic to macroscopic by mixing or layering as described below.

**Experimental**

Briefly, the longitudinal ( $R_1$ ), transverse ( $R_2$ ) and longitudinal relaxation in the rotating frame ( $R_{1\phi}$ ) were measured using, respectively, a 40 point inversion recovery experiment, a 16384 echo CPMG and a 40 point spin-locking experiment (3,4). The amplitude of the spin-locking pulse was varied, in different experiments, between 3 and 9 G. The relaxation measurements were done on two different sample configurations in a 5 mm NMR tube. In the first case, albumin containing solutions or phosphate buffered saline (PBS) solutions (denoted as ECF) were gently layered onto varying fractions of packed ghosts, keeping the total sample volume to 100 $\mu$ l. After doing our battery of relaxation measurements on such a sample (denoted layered), it was gently shaken (denoted mixed) and the NMR measurements repeated. The resulting decay curves were analysed using both non-linear least-squares techniques and linear inverse theory methods.

**Results**

Relaxation rate behaviour for two different ECF concentrations of albumin are shown in figures 1-3. In the mixed case all relaxation rates were observed to be monoexponential in nature. In the layered cases,  $R_{1\phi}$  and  $R_2$  were biexponential in nature, whereas  $R_1$  remained monoexponential, with the same value measured in the layered case. In the layered case, the compartment decaying with the greater rate was always associated with the intracellular water. This leads us to suggest that *macroscopic compartmentalization, by virtue of slower water exchange times, can generate biexponential decay behavior in tissue*. In addition the behaviour shown in the figures implies that for tissue like systems, *the predictive value of knowing the concentration dependence of relaxation rates in aqueous protein solutions can be very much reduced if the extracellular*

*protein solution is limited in extracellular volume*. The ability to interpret the observed changes in relaxation times is much improved by knowledge of the field dependence of the spin-locking experiment, and this may prove to be a superior way to introduce some specificity into quantitative relaxation measurements from NMR images.

**Acknowledgements**

We are grateful to the Alberta Heritage Fund for Medical Research for a Studentship (RSM) and a Medical Scientist Award (PSA). This work is supported by the Medical Research Council of Canada.

**References**

1. Allen, P.S., Castro, M.E., Treiber, E.O., Lunt, J.A. and Boisvert, D.P.J. *Phys. Med. Biol.*, 31, 669, 1986.
2. Menon, R.S and Allen, P.S. *Abstracts of the 6th SMRM*, 436, 1987, New York.
3. Menon, R.S. and Allen, P.S. *Biophys. J.* Submitted
4. Menon, R.S., Rusinko, M.S. and Allen, P.S. *Abstracts of the 7th SMRM*, 228, 1988, San Francisco.

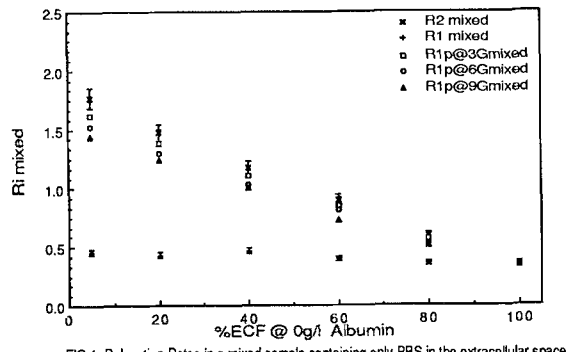


FIG 1: Relaxation Rates in a mixed sample containing only PBS in the extracellular space.

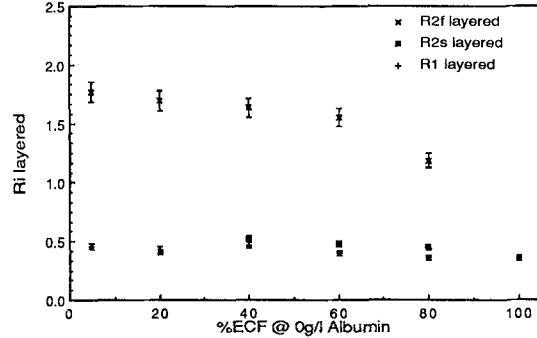


FIG 2: Relaxation Rates in a layered sample containing only PBS in the extracellular space.

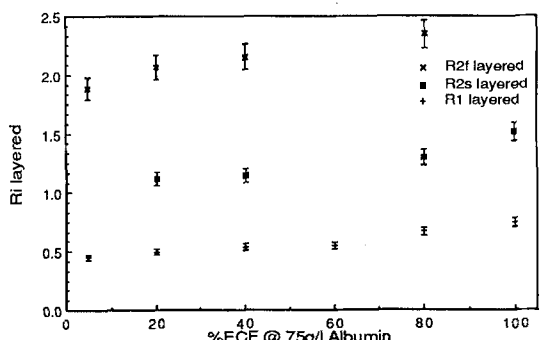


FIG 3: Relaxation Rates in a layered sample containing 75g/l Albumin in the extracellular space.

## The Effect of Diffusion on Transverse Relaxation in Normal Tissue.

Yoseph Rozenman, Xueming Zou, Howard L. Kantor  
 Massachusetts General Hospital and the Francis Bitter National Magnet Laboratory,  
 Massachusetts Institute of Technology, Boston, MA.

### INTRODUCTION

It is well known that diffusion in the presence of magnetic field gradients induces spin dephasing and accelerates transverse relaxation. Traditionally this effect has been considered a negligible contributor to  $T_2$  relaxation in tissue (1,2). The purpose of this study is to reassess this issue in several tissues: brain heart liver and spleen.

### METHODS

Animals: Samples were excised immediately after sacrifice from 9 Lewis rats (250-400g), washed in saline, blotted dry, wrapped with plastic film and placed in sealed NMR tubes. Excess blood was removed from the ventricular cavities in the hearts using saline flush through both atria. All measurements were made within 2 hours of tissue excision. Samples were obtained from three different rats for each tissue (liver and spleen samples were taken from the same rats).

NMR spectroscopy:  $T_2$  values were obtained at 37° and 8.4 Tesla using a CPMG pulse sequence. Each sample was examined with five to nine different  $\tau$  values from 0.2 to 10ms ( $2\tau$  is the separation between the 180° pulses in the sequence). Echo signals were obtained during similar periods of signal decay for the different  $\tau$  values in each tissue. Only the last echo was acquired from each pulse train, and  $T_2$  curves were constructed from 2 ( $\tau=10ms$ , spleen) to 12 ( $\tau=0.2ms$ ) echoes. Magnetic field homogeneity was maximized and 180° pulse duration was calibrated (33-36μs) for each sample before data collection. Measurements were also performed on water sample to ensure that no systematic errors were produced in the measured relaxation times.

Data analysis:  $T_2(\tau)$  values were obtained using a non-linear least square exponential fit for each  $\tau$  value. Diffusion induced transverse relaxation ( $R_d(\tau)$ ) was calculated from the formula:

$$R_2(\tau)=R_2(0)+R_d(\tau)$$

where  $R_2=1/T_2$  and  $R_2(0.2)$  was used for an estimation of  $R_2(0)$  (transverse relaxation in the absence of diffusion). Mean values of  $R_d(\tau)$  were plotted vs  $\tau^2$ , for each tissue.

### RESULTS

$R_2(0.2)$  values were  $20.0 \pm 0.5$ ,  $28.4 \pm 0.2$ ,  $43.3 \pm 2.5$ ,  $33.0 \pm 2.0$  s<sup>-1</sup> in brain, heart, liver and spleen respectively. Figure 1 is a graph of  $R_d(\tau)$  as a function of  $\tau^2$  for the different tissues. In all tissue samples studied there was an initial increase of  $R_d(\tau)$  with increasing  $\tau$  as would be expected in the case of unrestricted diffusion

$$R_d(\tau)=(\gamma^2 G^2 D/3)\tau^2 \quad (\text{eq. 1})$$

where  $\gamma$  is the gyromagnetic ratio,  $G$  is the magnetic field gradient and  $D$  is the diffusion coefficient. At higher  $\tau$  values  $R_2(\tau)$  becomes independent of  $\tau$ . This would be expected for the

case of bounded diffusion (or unrestricted diffusion in the presence of periodic magnetic field gradients), in which:

$$R_d(\tau)=\gamma^2 G^2 X^4/120D \quad (\text{eq. 1})$$

where  $X$  is the linear dimension of the boundary (3). The initial slope (S) and the plateau value (P) from the graphs are presented in the table together with tissue iron content in humans, as found in the literature (4).

Tissue	$S \times 10^{-6}(s)$	$P(s^{-1})[Fe](\mu\text{g/g wet tissue})$
Brain	$11.0 \pm 0.5$	$7.3 \pm 1.3$
Heart	$17.2 \pm 0.3$	$17.3 \pm 1.0$
Liver	$32.3 \pm 0.3$	$28.2 \pm 3.3$
Spleen	$71.5 \pm 3.4$	$67.0 \pm 2.0$

It can be shown from eq. 1 and 2 that:

$$P/S = (X^2/2D)^2/10 = t_x^2/10$$

where  $t_x$  is the time during which the molecule crosses  $X$ .  $P/S$  is approximately  $10^{-6}$  s<sup>-2</sup>, and  $t_x$  is approximately 3ms. Assuming  $D$  of  $10^{-5}$  cm<sup>2</sup>/s we get an estimate of  $2.5\mu\text{m}$  for  $X$  which suggests that the "boundary" is intracellular or more likely that there is a periodic variation of the magnetic field gradient in the cell. There was a significant correlation between iron content in the tissue and both  $S$  and  $P$  ( $r=0.98$ ,  $p<0.05$  and  $r=0.93$ ,  $p<0.05$  respectively).

### CONCLUSIONS

- A. Diffusion in the presence of magnetic field gradients has a significant influence on measured  $T_2$  values at high magnetic fields; this effect differs in magnitude between tissues.
- B.  $T_2$  varies significantly with  $\tau$  and calculations from this dependence suggest that diffusion is occurring in the presence of periodic intracellular magnetic field gradients.

### REFERENCES

1. Chang, D.C., C.F. Hazlewood, B.L. Nichols, et al. *Nature*, 235, 170, 1972.
2. Packer, K.J., *J. Mag. Reson.*, 9, 438, 1973.
3. Wayne, R.C., R.M. Cotts, *Phys. Rev.*, 151, 264, 1966.
4. Worwood, M., *Semin. Hematol.*, 14, 3, 1977.

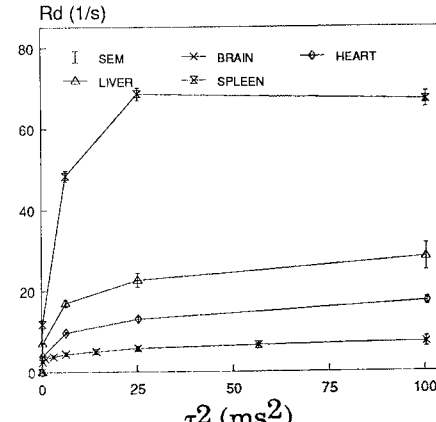


Figure 1: Diffusion induced transverse relaxation  $R_d$  as a function of  $\tau^2$  for the different tissues.

Simple Water Structure Models and Human *in vivo* Dispersion Data

J Ewen Rimmington  
Department of Biomedical Physics, University of Aberdeen, Scotland, U.K.

Introduction

Water structure models may be fitted to single frequency NMR relaxation data but data from several frequencies can provide a more stringent test because the model must predict the changing contribution made by "bound" water. To date most frequency dispersion data has been collected on *ex vivo* samples. However, changes occurring in the tissue on death may change the shape of the dispersion curve. We have collected human *in vivo* dispersion data and tested it against the following simple models.

Model 1 proposed by Fullerton(1)

$$1/T_{1\text{obs}} = 1/T_{1f} + b(1/T_{1b} - 1/T_{1f}) \quad <1>$$

where  $1/T_{1\text{obs}}$  is observed relaxation rate,  $1/T_{1f}$  is free water relaxation rate,  $b$  is bound water fraction and  $1/T_{1b}$  is bound water relaxation rate.  $T_{1b}$  is given by  $T_{1b} = 1.83 \times f_0 + 25.02$  where  $f_0$  is the Larmor frequency.

Model 2 proposed by Bottomley(2)

$$T_{1\text{obs}} = A f_0^B \quad <2>$$

$A$  and  $B$  are constants for each tissue. This equation was derived empirically from data compiled from literature.

Model 3 proposed by Escanyé(3)

$$1/T_{1\text{obs}} = C f_0^{0.5} + D \quad <3>$$

$C$  and  $D$  are constants related to the tissue bound and free water fractions respectively.

Models 1 and 3 are "two site, fast exchange" models i.e. they consider water to be either mobile, like pure water, or "bound" to the surface of a protein.

Method

Six point, *in vivo* dispersion curves were obtained over the frequency range 1.7-64MHz from 12 fixed-frequency imagers.  $T_1$  was measured using the standard pulse sequence for each machine i.e. either inversion recovery (IR) / saturation recovery (SR) or 6 point SR.

A range of tissues were examined on three normal individuals using pre-chosen regions of interest on specified slices.  $T_1$  was calculated by the site method. The scatter in the dispersion curves was reduced by calibrating each imager with a test object.

The water structure models were fitted by derivative-free non-linear least squares fit. The weight was the inverse square of the standard deviation expressed as a percentage of T1.

Results

Liver, white and grey brain: Within the scatter of the data these tissues were adequately fitted by all three models, eg brain data is shown in

Figure 1. Brain Data  
with Model 2 Curves

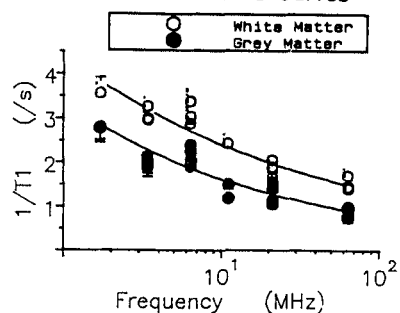
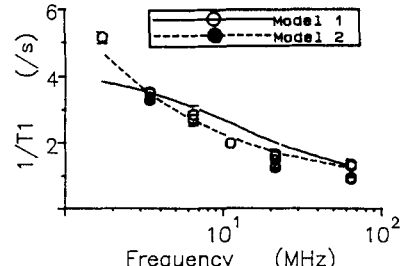


Figure 1 with the curves fitted by model 2.  
Muscle: Figure 2 shows this data with Model 1 (a poor fit) and Model 3 (the best fit). Model 2 produced too shallow a curve.

Spleen: Model 3 correctly estimates low frequency behaviour but underestimates at high frequencies. Models 1 and 2 were, again, less good fits.

Figure 2. Thigh Muscle

Discussion

In general, measurements made over a wide range of frequencies show that tissue dispersion curves inflect below 1MHz. At high frequencies they level off to leave a residual component from "free" water. Model 1, for all tissues, predicts an inflection at approximately 10MHz. Neither model 2 or 3 inflect in the frequency range examined. However, the relaxation rate predicted by Model 2 tends to zero at high frequencies. This model gives a shallower curve than Model 3. Model 3, for most tissues, provides the best fit. Also, the frequency independent constant  $D$  makes allowance for the free water contribution.

Although model 3 generally characterises the data best, over the range of frequencies used in imaging all three models are adequate for liver and brain but show limitations in describing the more complex behaviour of muscle and spleen.

References

1. Fullerton G., Cameron I.L., Ord V.A. Radiology, 151, 135, 1984.
2. Bottomley P.A., et al. Med. Phys. 11, 425, 1984.
3. Escanyé J.M., Canet D., Robert J. Biochim. Biop. Acta 721, 305, 1982.

## In Vivo Frequency Dispersion Studies of Tissue

M.A. Foster, J.E. Rimmington, J.R. Mallard  
 Department of Biomedical Physics, University of Aberdeen, Scotland, U.K.

Introduction

NMR relaxation times of tissues, studied ex vivo, show characteristic frequency dispersion behaviours. However, tissue relaxation times may change after death and the shape of the frequency dispersion curve may also change. The present study attempts to obtain frequency dispersion curves of  $T_1$  and  $T_2$  from living, human tissues. These curves are compared with ones from animal tissues ex vivo and provide an assessment of the frequency variation in  $T_1$ -derived "contrast" between adjacent tissues.

Methods

Unavailability of imaging systems with wide frequency ranges necessitated the use of several imagers. Results were obtained from twelve machines, operating at 6 frequencies, from 5 manufacturers and sited throughout Great Britain. Using the appropriate head or body coil, a female subject aged 35 and one of two males aged 21 and 22, were imaged through the head (grey and white brain and CSF), the upper abdomen (liver and spleen) and the mid-thigh (muscle, fat and marrow). A test object containing bottles of 2% agarose gel doped with various concentrations of manganese chloride was imaged at ambient temperature in each coil.

Differences in manufacturer's protocols prevented use of standard pulse sequences. Inversion recovery/saturation recovery (IR/SR) or 6-point SR were used for  $T_1$  and 2-point spin echo or CPMG for  $T_2$ .  $T_1$  and  $T_2$  values were obtained from regions of interest (ROIs) in the images and calculated using the standard method of the site. The ROIs were matched to pre-chosen slice maps to maximise consistency between sites. After collection of all imaging data, core samples were removed from the bottles of gels and their  $T_1$  and  $T_2$  measured at the imaging frequencies and ambient temperature on a Bruker CXP100 relaxation spectrometer. For most images the plots of  $T_1$  and/or  $T_2$  of the gels against values from the CXP100 showed some variation from an  $x=y$  line and/or were non-linear. To overcome this, the imager  $T_1$  and  $T_2$  were calibrated to the CXP100 values.

Results

Fig. 1 shows the uncalibrated (as collected) and calibrated (corrected to test object) data for muscle as a plot of relaxation rate against frequency. Calibration reduces the scatter in values, indicating that this arises from inaccuracies in some of the imagers. After calibration the scatter of the  $1/T_1$  dispersion graphs for most tissues was at least as small as that shown for muscle. Exceptions were CSF and bone marrow, presumably due to partial volume effects and adipose tissue with a multi-exponential relaxation curve which would have been sensitive to differences in imaging techniques. Adipose tissue did, however, show a shallow dispersion curve compared to other tissues, as expected.  $T_2$  values showed more scatter but the low frequency dependence could be observed for most tissues. Some tissues,

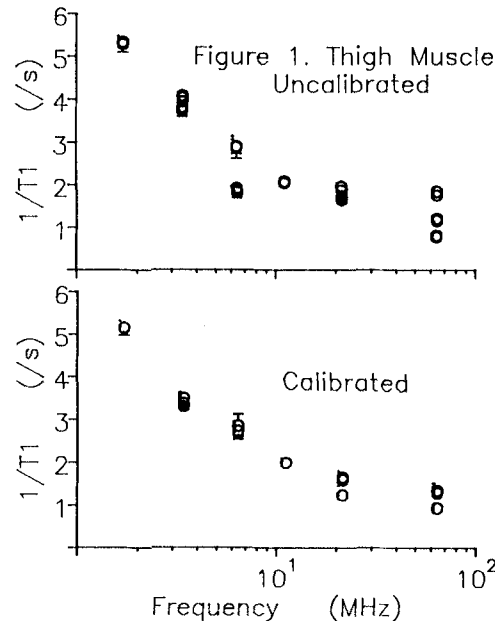
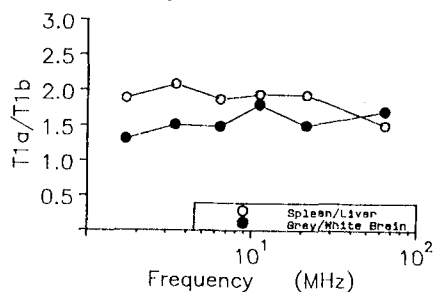


Figure 1. Thigh Muscle Uncalibrated  
 Figure 1. Thigh Muscle Calibrated

however, showed an increase in  $1/T_2$  with frequency. These included spleen (presumably due to tissue iron content) and marrow and adipose tissue, possibly because multi-exponentiality gave spurious results. Over the frequency range studied,  $T_1$ -related contrast between adjacent tissue pairs (grey/white brain and spleen/liver) showed no significant change (Fig. 2).

Figure 2. Contrast between adjacent tissues



Comparison of the  $T_2$  values with those obtained ex vivo from rat tissues was difficult due to the noisy dispersion data but for  $T_1$  most tissues showed a similarity between in vivo human and ex vivo rat. The only poor fit was for liver where the ex vivo data fitted the in vivo data well at low field but had a higher relaxation rate at high field. This suggests that the liver may be particularly prone to changes after death.

Conclusions

NMR frequency dispersion curves can be obtained in vivo using different imagers, but the results need to be calibrated to a standard. The  $T_1$  dispersion curves show the normal form and the  $T_2$  curves, although showing scatter, have expected or explainable trends.

### Measurements of T<sub>1</sub> and T<sub>2</sub> Relaxation Times in Mouse Tissue at 9.4T.

Albert S. Lee, B.A., Chen Chang, Ph.D., Robert Kersh, M.D., Leoncio Garrido, Ph.D., Faina Shtern, M.D., Thomas J. Brady, M.D. Department of Radiology, Massachusetts General Hospital, Boston, MA 02114

#### Introduction:

T<sub>1</sub> and T<sub>2</sub> relaxation time measurements are critical in the design of imaging techniques for optimization of tissue contrast. At this time T<sub>1</sub> and T<sub>2</sub> relaxation times have been reported for lower field strengths (100 MHz and less). Recently there has been increased interest in high field strength MR imaging, providing improved signal to noise ratios in voxels of smaller dimensions, which are critical for MR microscopy (1). This abstract describes *in vitro* measurements of T<sub>1</sub> and T<sub>2</sub> values at 9.4 Tesla (400 MHz) for various mouse organs.

#### Materials and Methods:

All spectroscopic measurements were made on a Bruker MSL400 spectrometer (84 mm diameter bore) operating at a field strength of 9.4 Tesla. Nineteen 7-10 week old inbred C57BL/6 mice were sacrificed by cervical dislocation. Brain (n=4), heart (n=3), kidney (n=4), liver (n=5), and skeletal muscle (n=3) were excised within five minutes of death, sealed tightly in stretched Parafilm to prevent water loss, and placed in a 20 mm spectroscopy tube, which was in turn placed in a 20 mm <sup>1</sup>H probe. All measurements were made on freshly excised tissues equilibrated to 37° C.

T<sub>1</sub> was measured using an inversion recovery sequence (2) by varying inversion time from 10 ms to 10 sec. T<sub>2</sub> was measured by both Hahn spin echo (SE) (3) and Carr-Purcell-Meiboom-Gill (CPMG) pulse sequences (4). For the standard Hahn SE sequence, TE ranged from 200 us to 50 ms. The CPMG sequence generated an echo train with a 4 ms inter-echo delay. The linewidths for these experiments were always less than 200 Hz. All sequences used whole volume excitation with hard pulse widths less than 100 microseconds in duration. Measured values were generated by a least-squares fit of data to a single exponential equation.

#### Results and Discussion:

Mean values ( $\pm$  one standard deviation) for measured T<sub>1</sub> and T<sub>2</sub> relaxation times are calculated and summarized in Table I. Our results suggest that relaxation times for these murine tissues at 9.4T differ from measurements at lower field strengths (5). T<sub>1</sub> values at 400 MHz are approximately two times longer than those described for these tissues at lower fields (100 MHz and less). The increase in T<sub>1</sub> relaxation time with increase in field strength is expected (6). T<sub>2</sub> values, on the other hand, are approximately 50-60% shorter in comparison with previously reported values at fields as high as 100 MHz. Our observation of short T<sub>2</sub> times at high field strength is in accord with previously reported work describing this trend in canine brain tissue up to 300 MHz (7). These shorter T<sub>2</sub> relaxation times require short TE's for optimum contrast in T<sub>1</sub>-weighted images. Additionally, the longer T<sub>1</sub> values make T<sub>2</sub>-weighted images very time-costly (e.g. a T<sub>2</sub>-weighted liver image on our system with TR of 7500 ms, 2 averages, and 256 phase encoding steps takes a minimum of 64 minutes to acquire).

tissue	T1 in ms	CPMG T2 in ms	Hahn T2 in ms
brain	2005 $\pm$ 41 (n=4)	42.4 $\pm$ 0.52 (n=3)	34.7 $\pm$ 0.71 (n=2)
heart	1970 $\pm$ 29 (n=3)	26.9 $\pm$ 0.67 (n=3)	18.3 $\pm$ 0.53 (n=3)
kidney	1810 $\pm$ 68 (n=4)	27.9 $\pm$ 2.33 (n=4)	20.2 $\pm$ 0.38 (n=4)
liver	1337 $\pm$ 45 (n=3)	18.4 $\pm$ 1.87 (n=5)	13.2 $\pm$ 0.46 (n=3)
muscle	2180 $\pm$ 20 (n=3)	31.0 $\pm$ 2.32 (n=3)	24.2 $\pm$ 0.36 (n=3)

Table I

#### References:

1. Aguayo JB, et al., *Nature* 322:190-91 (1986).
2. Farrar TC and Becker ED, *Pulse and Fourier Transform NMR, and Introduction to Theory and Methods*. Academic Press, NY (1971), pp. 20-23.
3. *Ibid.*, pp. 22-25.
4. *Ibid.*, pp. 27-29.
5. Bottomley PA, Foster TH, Argersinger RE, and Pfeifer LM. *Medical Physics*;11(4) Jul/Aug:425-448 (1984).
6. *Ibid.*
7. Kurland RJ and Ngo FQH. *Magnetic Resonance in Medicine*, 3:425-431 (1986).

## Proton Spectra of Cylinders of Hydrated Cortical Bone: the Effects of Oxygen-17 Enrichment.

Richard G. Barr<sup>(1)</sup>, Amos L. Hopkins<sup>(2)</sup> and Clyde B. Bratton<sup>(3)</sup>.

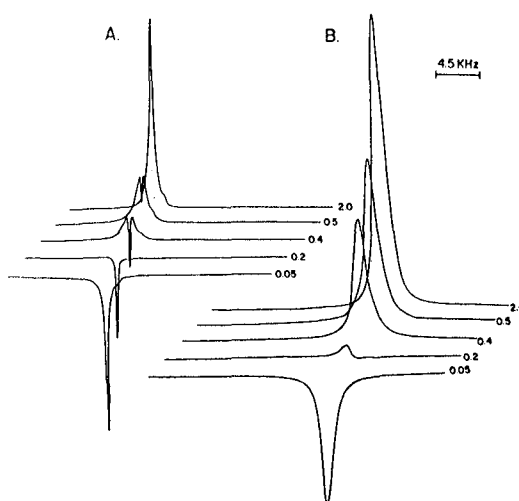
Departments of (1) Biochemistry, (2) Anatomy and Radiology, Case Western Reserve University, Cleveland, OH 44106, (3) Physics, Cleveland State University, Cleveland OH, 44115.

Introduction

In spite of its singular qualifications in studies of tissue hydration, the application of proton NMR to bone has been very limited. It is well known that both the mechanical and electrical behavior of dry bone is very different from that of wet bone (1) yet there are apparently no NMR studies of the state of water at physiological levels of hydration in structurally intact tissue samples. The few reports to be found are either on undefined samples which are referred to only as "bone", powder samples with very low (<5%) water contents or the mineral component after the removal of the organic matrix. As a consequence that water fraction which plays a role in determining the biophysical behavior of the living bone has been overlooked. The present report is primarily concerned with the behavior of water protons at the physiological range of hydration in cylinders of solid cortical bone tissue which is about 15% water. Secondarily observations are included on both the effects of reduction in water content and changes in the fiber-field angle on the proton NMR signals.

Results and Discussion

The proton spectra of cylinders of dense human cortical bone is composed of several overlapping classes of water proton peaks which can be distinguished on the basis of their proton relaxation times. In the fully hydrated state the spectra is dominated by a central peak, or group of peaks, due to the readily removable majority fraction of the water as is seen in using the Carr-Purcell inversion recovery method for  $T_1$  in Fig 1 A. The narrowest component of the central peak inverts through the other broader ones at a different time. This leads to estimates of  $T_1$  for the total water component in fully hydrated samples falling between 250 and 660 ms, depending on which component is measured and how completely the surface water has been removed by blotting. The water contained in the Haversian system of canals is undoubtedly makes a major contribution to the narrowest component of the central line.



When the same inversion-recovery sequence is used on samples which have been partially dried (25% of their total water removed), there is no evidence of one peak inverting through another (Fig 2 B). In addition, the broader component has not gone through zero at  $t = 0.2$  s which is the case in the fully hydrated sample. It should be noted that times are the same in 1 A and 1 B but that the areas under A and B are not comparable due to the greater gain used in B. If these components are in communication through proton exchange it is reasonable to assume that the replacement of the narrow water component with an oxygen rich air interface through drying, has altered the proton relaxation rates of the remaining water, which suggests the use of caution in extrapolation from the results of partially dried systems to their behavior in the fully hydrated state. As an alternative to drying we are replacing the normal oxygen-16 water with oxygen-17 water, with has been shown to greatly shorten the  $T_2$  of water in other tissues(2)

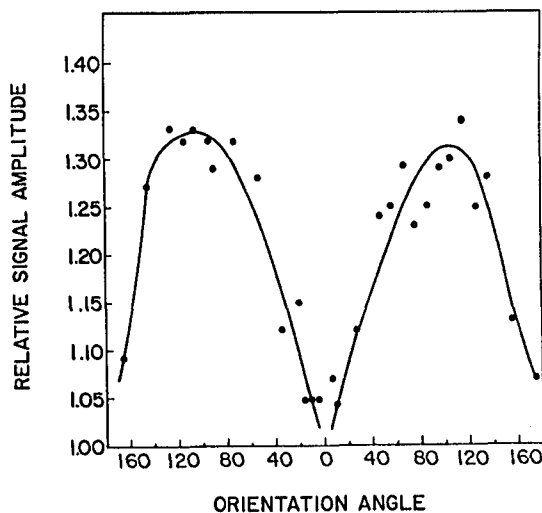


Figure 2

The possibility that orientation effects could be observed in bone was investigated. In the 24 MHz probe it is possible to obtain any angle between the fiber axis and the applied magnetic field of the Varian 4012 magnet by using cylinders of bone cut at  $90^\circ$  to the original long axis of the intact bone. Changes in the fiber - field angle produced a 30% change in the peak magnitude with a broad maximum at  $90^\circ$  to  $120^\circ$  and a sharp minimum at  $0^\circ$  (Fig. 2). This is similar to the magnitude effect seen by Berendsen (3) which he attributed to orientation of the adsorbed water molecules.

1. Otter, M., J. Shoenung and W. S. Williams, *J. Orthop. Res.* 3, 321, 1989.
2. Hopkins, A.L., E.M. Haacke, J. Tkach, et al. *Magn. Reson. Med.*, 7, 222, 1988.
3. Berendsen, H. J. C., *J. Chem. Phys.*, 36, 3297, 1962.

Proton Relaxation Time Alterations in Rat Liver treated with  
different Hepatotoxic Model Agents<sup>b</sup>

P.Holzmueller, G.Gomiscek, E.Moser, E.M.Markis\* and H.Echsel\*  
Institut f. Med. Physik, <sup>a</sup>Institut f. Path.Anatomie and <sup>b</sup>Institut  
f. Allg. und Exp. Pathologie, Universitaet WIEN, A-1090 AUSTRIA

Proton relaxation times measured *in vitro* do not only contain information about almost dead tissue but are even sensitive to differences due to physiological status (*in vivo*) like sex or starvation. In addition, by applying different wellknown animal models it may serve as a method for a more profound knowledge of relaxation time mechanisms in tissue (normal and pathologic) and to optimize *in vivo* MRI through quantitative comparison.

#### Material and Methods

Long term (4-120 hours) alterations of rat liver after carbontetrachloride ( $CCl_4$ ) or ethionine intoxication have been investigated. Male Sprague Dawley rats (Him:OFA(SD), 150-200g) were pretreated with phenobarbital and received a single dose of  $CCl_4$  (1ml/kg body weight), dissolved in corn oil p.o. DL-ethionine (1g/kg bw.), dissolved in lightly acidic aqua dest. was injected i.p. to female Sprague Dawley rats (Him:OFA(SD), 180-200g). Liver injury and regeneration were followed by low resolution NMR. Spin-lattice ( $T_1$ )- and spin-spin ( $T_2$ ) relaxation time measurements were performed *in vitro* with a Bruker minispec pc 120 by fast saturation recovery (40 points,  $T_R=0.1s$ , 9av.) and CPMG ( $T_E=2ms$ ,  $N=100$ ,  $T_R=3.0s$ , 9av.) respectively. Measurements of  $T_1$  and  $T_2$  versus time after excision (5-240min, 9min time interval) were undertaken at 37°C. The time course was studied in normal (untreated, phenobarbital pretreated and sham injected) and damaged (4,24,48,72,96 and 120 hours after  $CCl_4$  or ethionine application) rat liver, each group consisting of five animals. Mono- and biexponential models were fitted for quantitative data analysis and statistical methods were applied for comparison of models. The total water content of liver samples was determined gravimetrically. A part of fresh liver tissue was fixed in formaldehyde, stained with hematoxylin-eosin and damage was evaluated semi-quantitatively by light microscopic examination.

#### Results and Discussion

$CCl_4$  is a toxic agent which is known for its ability to induce fatty liver and necrosis. Ethionine is producing fatty liver without any necrosis. So we decided to use these two damage models to see what effects may be detected on relaxation time behaviour. (Examinations with paracetamol, a compound which leads necrosis only are in progress). Liver spin-lattice relaxation time enhancement after  $CCl_4$  treatment (taken at ca. 30min after excision) is about 20% at maximum liver damage, 48 hours

after toxin application. About the same maximum occurred for ethionine intoxicated animals. However, the increase in  $T_1$  was only half as large for ethionine and regenerating livers showed relaxation values beyond normal. The most interesting point in  $T_1$  time course after excision measurements is that  $T_1$  is able to detect necrosis (1). This was also seen in our experiments with  $CCl_4$ , where the shape of the  $T_1$  time course followed the histologically evaluated pathology, whereas ethionine treated rat livers showed a shape different from normal and  $CCl_4$  treated non-necrotic rats but no correlation between  $T_1$  values and fatty liver induction could be established. Spin-spin relaxation times (taken ca. 30min after excision) showed alterations for used hepatotoxic models versus normal rat liver, maximum values were obtained 48 hours after intoxication. At this moment  $T_2$  for  $CCl_4$  treated animals is enhanced by about 50% compared to normal values (36ms).  $T_2$  increase for ethionine injected animals was in the same range. The shape of the time course of  $T_2$  showed no significant difference between the two types of damage. The increase and decrease of relaxation times correlated with the known course of damage and regeneration, however our histologic examinations showed, that there was no correlation between fatty liver after ethionine and relaxation data. Overall water content did not correlate with observed relaxation time values from  $CCl_4$ - or ethionine treated rat liver.

As expected there were differences in relaxation behaviour of these two liver damage models. They occurred mainly in  $T_1$  time course, thus  $T_1$  time course is a parameter which is sensitive to the kind of damage, whereas  $T_2$  increase shows only the severity of the liver damage, but does not differ for different types of lesions. Thus  $T_2$  alteration seems to be due to unspecific reactions to tissue damage like fever is an unspecific reaction to different types of illness. These findings of damage specific  $T_1$  time course and unspecific  $T_2$  have to be a matter of concern for MRI. However, the role of relaxation times for *in vivo* tissue characterization may also be different from findings *in vitro*.

*In vivo* measurements with the described models are in progress.

1. Moser E. et al., submitted to SMRM  
8<sup>th</sup> Annual Meeting, Amsterdam, 1989

<sup>b</sup> work supported by the Austrian Fond zur Förderung der wissenschaftlichen Forschung under grants P5342 and P7017

ASSESSMENT OF THE FIBRINOLYTIC ACTIVITY OF TISSUE PLASMINOGEN ACTIVATOR USING  $T_2$  RELAXATION TIMES

Azoury R., Bitton M., Abrashkin S., Lavie E.,

Radiopharmaceuticals Department, Soreq Nuclear Research Center, Yavne 70600, ISRAEL.

The use of human tissue-type plasminogen activator (t-PA) as a potential thrombolytic agent is a relatively new approach to the treatment of acute myocardial infarction and other thrombotic disorders. Plasminogen activators are serine proteases which convert plasminogen into active plasmin that induces the fibrinolytic processes. Therefore, PA acts as the main mediator of vascular clot lysis.

**PURPOSES:**

The purposes of the present study were to develop a new approach to study the structure of fibrin clot, to explore the relations between the clot lysis and possible compartmentalization of water, and to follow the fibrinolysis kinetics induced by t-PA using proton relaxation times.

The amount of t-PA in the assay markedly affected the lysis rate and level of the clot (fig. 1). The changes induced by the lytic activity of t-PA were reflected in pronounced prolongation of the transverse relaxation times  $T_2$ . Furthermore, deactivation of t-PA with diisopropyl fluorophosphat (DFP) cause only nonspecific ( $\approx 10\%$ ) prolongation of  $T_2$ . The graphical analysis of the magnetization signal decay seems to be associated with structural features of the clot and reflects the liberation of compartmentalized water from the clot (fig. 2, table 1).

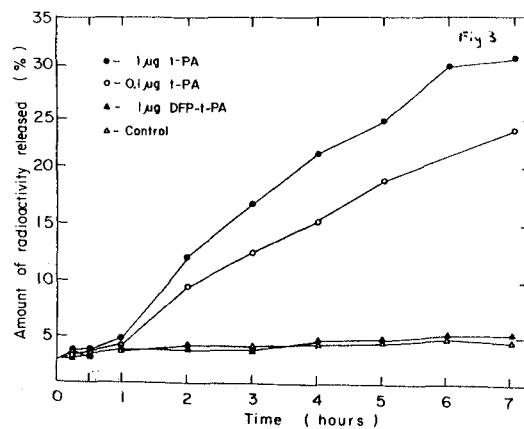
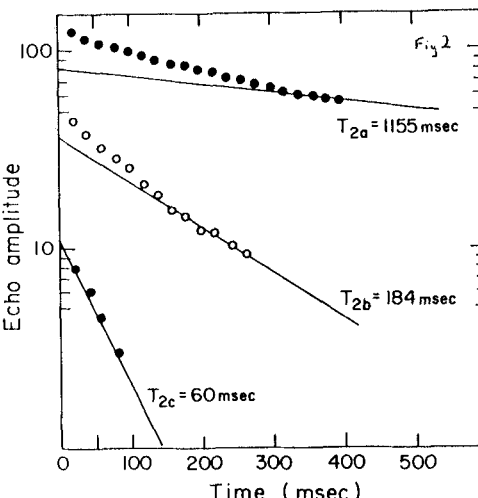
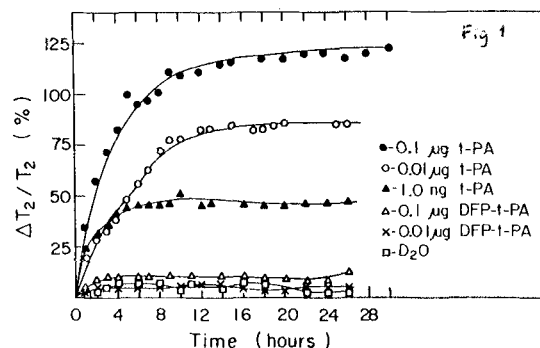
**CONCLUSIONS:**

$T_2$  measurements is a very sensitive way to assess the proteolytic effect of t-PA and other proteases such as chymotrypsin, trypsin, etc. The present results inforce evidence to a possible two-phase mechanism in the lysis of fibrin: t-PA alters the organization and the properties of water trapped in the clot prior to the fragmentation of fibrin. The sensitivity of the technique is significantly superior to that of other techniques (such as radioactive assay) and provides information on early stages of the fibrinolytic processes.

Table I

Changes in the transverse relaxation rate ( $R_2 = 1/T_2 \text{ sec}^{-1}$ ) and the fractional population (%) in parenthesis of the three components of the spin-spin relaxation time, before and after the addition of t-PA to the fibrin clot.

Time (min) after t-PA addition	$R_{2a} (\text{sec}^{-1})$	$R_{2b} (\text{sec}^{-1})$	$R_{2c} (\text{sec}^{-1})$
0 (no t-PA)	0.865 (63%)	5.43 (31%)	16.66 (6%)
10	0.765 (68%)	5.92 (20%)	16.95 (11%)
60	0.761 (85%)	5.31 (16%)	-
720	0.480 (92%)	5.81 ( 9%)	-
Control			
H <sub>2</sub> O + fibrinogen	0.381 (91%)	6.09 (10%)	-
H <sub>2</sub> O	0.45 (100%)	--	--



Experimental brain tumors in cats: Multiparametric tissue characterization based on multiexponential  $T_2$  evaluation at 4.7 Tesla

M. Höhn-Berlage, K. Bockhorst, Y. Okada, K.-A. Hossmann, T. Tolxdorff\*, F. Upmeier\*  
 Max-Planck-Institut für Neurologische Forschung, 5000 Cologne 91, FRG  
 \*Medizinische Statistik und Dokumentation RWTH, 5100 Aachen, FRG

**Introduction:** Determinations of relaxation times  $T_1$  and/or  $T_2$  have long been used for the characterization of tissue samples in vitro. These measurements have been carried out to differentiate between benign and malignant tissue types, as a support of diagnostic purposes. More recently, this successful approach has been extended to the multicompartmental analysis of the  $T_2$  relaxation data (1). The same analytic procedure was applied in vivo using a multiecho CPMG sequence at low field (0.28T) (2). However, these in vivo studies were limited to a small number of volunteers with differing pathological states, and it has been questioned whether the in vitro approach can be reliably applied to the in vivo situation. Therefore, we have undertaken a study on a series of cats with implanted tumors to analyze  $T_2$  of the brain tissue and to compare the results with histological findings and invasive biochemical methods for evaluation of brain water and tissue metabolites.

**Methods:** Experimental brain tumors were produced in cats by stereotactical xenotransplantation of glioma cells. Thirteen tumor-bearing animals (plus two controls) were studied at various times after tumor implantation (1, 2, 3, 4 weeks) to observe tumor growth and edema development. The animals were tracheotomized and mechanically ventilated. The imaging equipment consisted of a 4.7T high field system (Biospec, Bruker Germany) with a 30 cm bore magnet. The images were obtained using either a birdcage resonator or a doubly-tuned surface coil (15 cm diameter) which was positioned horizontally above the head. The animal's head was fixed in a stereotactical head holder during the NMR experiment. Up to three coronal and/or horizontal slices (3 mm thickness) were imaged by CPMG sequence. Data from 16 echoes were submitted to multiexponential evaluation (RAMSES software package, (3)) of the transverse magnetization decay curve.  $T_2$  values, the relative spin density rho, and the relative contribution alpha of the  $T_2$  components in the individual pixels (the latter two parameters are expressed in %) were used to differentiate various brain tissues. At the end of the NMR experiments the brains were frozen in situ for regional biochemical analysis. Thus NMR relaxation parameters were

correlated with the regional distribution of metabolites, water content and serum extravasation.

**Results:** Edema and tumor could be clearly differentiated from each other, and from normal grey and white matter, respectively. For separation of tumor from the surrounding edema the selection of a very narrow range of the spin density rho (20 - 30 %) or the transverse relaxation time  $T_2$  (65 - 90 ms) was most efficient. The separate presentation of muscle tissue, edema, grey and white matter, and of cerebrospinal fluid was achieved by selection of  $T_2$  and alpha value ranges. Within the edematous zone a gradient of  $T_2$  times was noted with the long end of the  $T_2$  dispersion in the center of the edema. In the late stages of tumor growth the ipsilateral ventricle which is in direct contact with the edematous tissue, revealed distinct differences in relaxation parameters not detectable on conventional  $T_2$ -weighted images. This change in  $T_2$  and relative contribution alpha for the ipsilateral ventricle is interpreted as an influx of (protein-containing) edematous fluid into the ventricle. These changes and/or variations of relaxation parameters will be discussed in relation to the biochemical analysis and the water content determination of various brain regions.

- 1) Barthwal, K. et al. *Magn. Reson. Med.*, 3, 863, 1986.
- 2) Gersonde, K. et al. *Magn. Reson. Med.*, 1, 463, 1984.
- 3) Gersonde, K. et al. *Magn. Reson. Med.*, 2, 390, 1985.

**Spin-Spin Relaxation in Lung: Hahn-Echo and Carr-Purcell Measurements at Different Frequencies**

H Kolem, C Goodrich, K Ganesan, DC Aillion, AG Cutillo, S Chen,  
AH Morris, S Shioya, S Watanabe  
University of Utah and LDS Hospital, Salt Lake City, UT USA

**Introduction**

Previous spin-spin relaxation measurements in rat lungs have shown that the transverse magnetization decay can be fit by a mult exponential function (1,2). The reported values of exponential components are not entirely consistent and appear to depend on such factors as pulse sequence (Hahn-Echo vs. CPMG) characteristics of lung specimen (intact isolated lung, *in-vivo* lung, lung fragments, etc.), lung inflation, and Larmor frequency.

In order to investigate the effects of diffusion and internal gradients in lung, we performed Hahn-Echo and Carr-Purcell-Meiboom-Gill (CPMG) measurements in excised rat lungs and in pieces of lung tissue at various Larmor frequencies (magnetic fields) and different inflation pressures.

**Experimental Techniques**

Lungs were excised from female Sprague-Dawley rats (200g). Whole intact lungs were studied immediately after excision. Some of the lungs were degassed before measurements using the oxygen absorption method. In this method all air in the alveoli and airways is replaced by oxygen and the trachea is then clamped, after which the animal's own circulation removes the oxygen, thereby resulting in an airless (degassed) state for the lung. NMR measurements were performed on these degassed lungs as well as on lungs inflated with air to various pressures (0-30 cm H<sub>2</sub>O). In a few experiments, passively deflated fragments of the outer portion of the lung (peripheral parenchyma) were used.

The NMR experiments were performed in a superconducting magnet with a 33 cm bore initially at fields of 0.95 T and 1.9 T. We used the CPMG pulse sequence with a spacing between 180° pulses of 1 ms in order to determine the T<sub>2</sub> components. On the same lungs, we also performed Hahn spin echo measurements. All of the CPMG experiments and most of the Hahn

measurements were done in the non-imaging mode. Since Hahn echo amplitudes are sensitive to diffusion in the presence of gradients, we optimized the magnet's homogeneity by adjusting the room temperature shim, thereby reducing the external gradients to values smaller than 0.5 mG/cm.

**Results**

Typical transverse magnetization decays obtained with the Hahn echo and CPMG methods in excised lung are compared in Fig. 1. The CPMG data appears to be characterized by a time constant T<sub>2</sub> which gradually increases from a few ms to 400 ms. We were able to fit these data with four (but not fewer) time constants: 3 ms (representing 7% of the magnetization M), 50 ms (70% M), 140 ms (20% M), and 400 ms (3% M). Even though the data in Fig. 1 were obtained for a passively collapsed lung, similar experiments on other lungs at different inflation pressure could also be fit by four time constants which vary slightly with inflation pressure. However, the long component could not be detected in passively-deflated pieces of lung tissue.

As shown in Fig. 1, the echo amplitude decay measured by the Hahn sequence is much faster than that measured by CPMG, thereby indicating that diffusion across internal gradients is occurring. The ratio of the Hahn to CPMG echoes is of the form  $\exp(-\lambda t)$  for all but the shortest time constant, suggesting the possibility of restricted diffusion (3).

Further discussion of the spin-spin relaxation mechanisms will be presented along with the Larmor frequency and inflation pressure dependence of T<sub>2</sub>.

**Acknowledgments:**

This work was supported by NIH grants CA44972 and HL31216.

**References:**

1. Kveder, M, et al, Mag Res Med 2, 432 (1988).
2. Ganesan, K, et al, SMRM 1988, 577.
3. Packer, KJ, J Mag Res 9, 438 (1973).

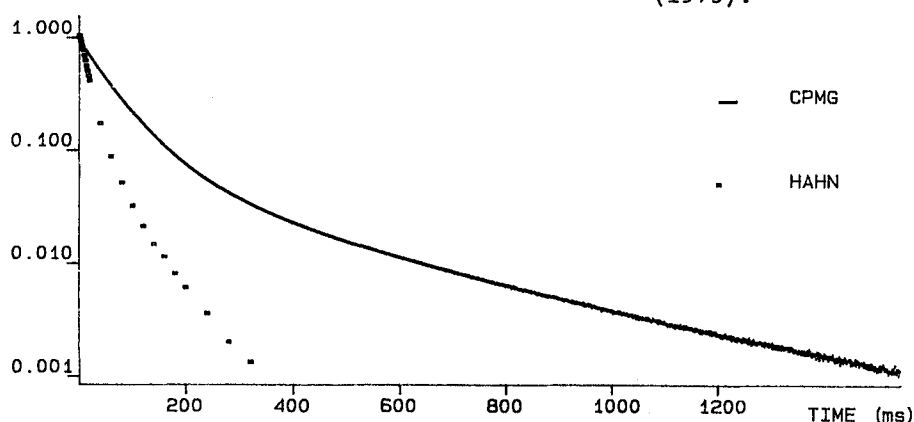


Fig. 1. Normalized spin echo amplitude vs. echo time for passively collapsed lung at 1.9 T.

PROTON T<sub>2</sub> COMPONENTS OF MUSCLES RECOVERING FROM NERVE TRAUMA

R. Abello, K. Long, J. Wondergem, E.E. Kim, L.K. Misra.  
 Univ. of Texas M.D. Anderson Cancer Center and Rice University,  
 Houston, Texas

Nerve injury is known to affect the intrinsic properties of skeletal muscles (1). Various changes in muscles result from reduced activity, loss of neurotrophic molecules and accumulation of products of nerve degeneration. The structural integrity of muscles may be compromised leading perhaps to posttraumatic atrophy. Variable recovery may follow reinnervation of muscle fibres by newly formed axons (1). The objective of our study was to evaluate the effects of posttraumatic reinnervation and recovery of muscles on their multiexponential proton spin-spin relaxation times, T<sub>2</sub>.

The right sciatic nerve of six Wistar rats ( $310\pm17$ g), anesthetized with pentobarbital sodium (50mg/kg, IP) was crushed for one minute at the level of the sciatic notch using a hemostat. The left leg, with intact sciatic nerve, served as an internal control to the traumatized right leg. The 'toe spreading' test of De Medinaceli et al (2) was used to evaluate the muscle tones. By 30 days post-trauma, approximately 78% recovery of motor function in right leg was evident. Rats were then sacrificed and their gastrocnemius muscles were excised. Proton T<sub>2</sub> relaxation times of muscles were measured on a Bruker SXP NMR Spectrometer at 30 MHz by the Carr-Purcell-Meiboom-Gill pulse sequence at 25°C. After T<sub>2</sub> measurements, the water and fat contents of muscles were determined by gravimetric procedures.

Our T<sub>2</sub> analysis focused on two components: T<sub>2S</sub> and T<sub>2L</sub>. The T<sub>2S</sub> values ( $47\pm8$ ms) of gastrocnemius muscles, innervated by the traumatized nerve, were similar to those ( $41\pm8$ ms) of the contralateral control muscles. Approximately 8-10% of the total signal contributed to the T<sub>2S</sub> component. The T<sub>2L</sub> relaxation times ( $179\pm10$ ms) of the affected muscles were, however, significantly ( $p<0.5$ ) prolonged compared to T<sub>2L</sub> ( $144\pm14$ ms) of the control muscles. The proportions of signal contributing to the T<sub>2L</sub> of control and affected muscles were  $76\pm4\%$  and  $83\pm2\%$ , respectively. Results suggest that T<sub>2L</sub> values may be helpful in evaluating the posttraumatic recovery of muscles. The water content of recovering muscles was significantly ( $p<0.01$ ) elevated ( $77.55\pm0.46\%$  vs.  $80.43\pm1.72\%$ ). The fat content of affected muscles ( $3.86\pm0.61\%$ ) was also significantly ( $p<0.05$ ) higher than that of control muscles ( $2.68\pm0.9\%$ ). Elevated water and fat contents may, therefore, contribute to changes in the longer relaxing T<sub>2</sub> component of recovering muscles.

References

1. Jolesz F., F.A. Streter. *Ann Rev Physiol*, 43, 531, 1981.
2. De Medinaceli L., T. Quach, A.M. Duchemin, R.J. Wyatt. *Expt Neurol*, 94, 788, 1986.

(Supported by a Grant from General Electric Medical Systems)

## Magnetic resonance imaging of human blood: An in vitro study.

R. Nyman, A Ericsson and F. Niklasson. From the Departments of Diagnostic Radiology and Clinical Chemistry, Akademiska sjukhuset, University of Uppsala, S-751 85 Uppsala, Sweden.

**Introduction:** The MRI characteristics of blood have been extensively investigated by many authors (1-8). However, there is still unclear what is causing the change in signal intensity during aging of haematoma. The concentration of hemoglobin (Hb) and its different components oxy-, deoxy- and met-Hb have been suggested to effect the MRI parameters. The magnetic field strength as well as the image technique used will also influence the MRI behaviour of blood. The aim of this study was to make an in vitro MRI characterization of the different blood products and to simulate the in vivo situation by a simple model.

**Materials:** Fresh blood products from healthy adult volunteers and the brain in a healthy volunteer were investigated. Whole blood, concentrated red blood cells (RBC), clots, plasma, serum and white blood cells (WBC) were prepared. Oxy-Hb was converted to deoxy-Hb by bubbling N<sub>2</sub> through whole blood. Met-Hb was made by adding NaNO<sub>2</sub> to whole blood. In order to compare the effect of intra- and extracellular Hb the samples were hemolysed by freezing. The effect of different concentration of oxy-, deoxy- and met-Hb and the effect of storage were also studied. The effect of temperature change (+22° C to +37° C) of the different blood products on the MRI parameters was studied.

**Methods:** MRI was performed with a Siemens Magnetom, 0.5 T. Six single-echo sequences with TR of 100, 300, 500, 700, 1500 and 3000 ms were recorded for estimation of T1 and relative proton density and a multiple-echo sequence with TR of 1500 ms and 16 TE:s of 30-480 ms for T2. The effect of different concentrations of oxy/deoxy- and met-Hb, in comparison with normal brain, on the signal intensity in commonly used pulse sequences (500/30, 2000/30; 70 or 120) was simulated. A linear correlation between Hb concentration and 1/T1, 1/T2 and proton density, respectively, was assumed. The calculated values were also used for synthesizing areas, simulating haematoma, in normal brain images in order to see the effect of different adjustments of window and level on the monitor.

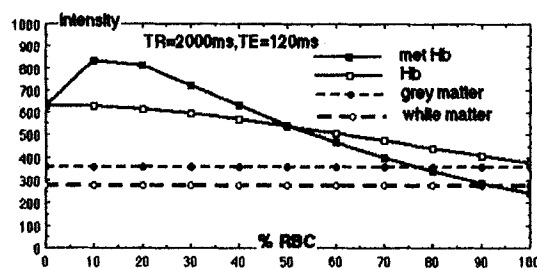
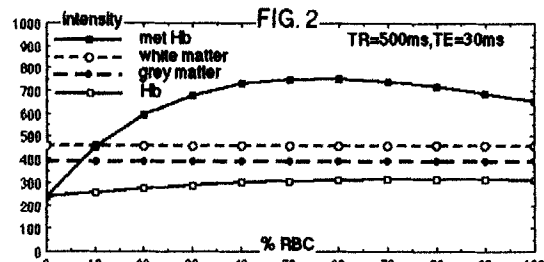
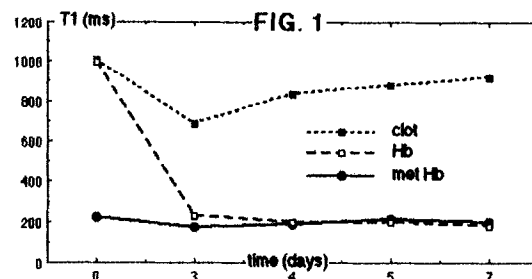
**Results:** RBC concentrated by centrifugation or by clotting had similar MRI characteristics as concentrated WBC. The relaxation times were prolonged and the proton density increased by decreasing Hb concentration. Oxy- and deoxy-Hb had similar MRI characteristics. Increased concentration of met-Hb caused a significant shortening of both T1 and T2. No major differences in the MRI parameters between intra- and extracellular Hb were noticed. Oxy/deoxy-Hb had also similar MRI characteristics as albumin solutions and plasma at comparable protein concentrations. The storage of blood caused a shortening of T1 and T2, paralleled with appearance of met-Hb in the samples. This effect appeared earlier in time at 37° C compared to 22° C and was less pronounced in clots compared to concentrates of RBC. (Fig. 1). The increase in temperature from 22° C to 37° C caused a 20 % increase in T1 and 5-10% in T2, except for met-Hb where T1 decreased by 50 % and T2 by 10 %. The simulated curves in comparison to normal brain for the pulse sequences 500/30 and 2000/120 are presented in Fig. 2.

**Discussion:** The major impact on signal intensity by blood seems to be Hb concentration and the formation of met-Hb. At the field strength of 0.5 T deoxy-Hb has the same effect as oxy-Hb on the MRI parameters. The Hb molecule seems to have similar MRI characteristics as other proteins.

The hypointensity in the T2-weighted sequences seen in haematomas on day 1 to 3 is probably due to retracted clot and also to a low concentration of early formed met-Hb. Later in time will the increased formation of met-Hb cause a major increase in signal intensity in the T1-weighted image as has been proposed by others (1-5, 8)

### References:

- Brooks R.A. and Chiro G.D.: Magnetic resonance imaging of stationary blood: A review. *Med. Phys.* 14, 903, 1987.
- Chiro G.D., Brooks R.A., Girton M.E., et al.: *AJNR* 7, 193, 1986.
- Cohen M.D., McGuire W., Cory D.A. and Smith J.A.: Mr appearance of blood and blood products: An in vitro study. *AJR* 146, 1293, 1986.
- Gomori J.M., Grossman R.I., Yu-Ip C. and Asakura T.: NMR relaxation times of blood: Dependence on field strength, oxidation state and cell integrity. *J. comput. assist. tomogr.* 11, 684, 1987.
- Gomori J.M., Grossman R.I., Goldberg H.J., et al.: Intracranial hematomas: Imaging by high-field MR. *Radiology* 157, 87, 1985.
- Hayman L.A., Ford J.J., Taber K.H., et al.: T2 effect of hemoglobin concentration: Assessment with in vitro MR spectroscopy. *Radiology* 168, 489, 1988.
- Thulborn K.R., Waterton J.C., Matthews P.M. and Radda G.K.: Oxygen dependence of the transverse relaxation time of water protons in whole blood at high field. *Biochem. et Biophys. Acta* 714, 265, 1982.
- Zimmerman R.D., Heier L.A., Liu D.P.C., et al.: Acute Intracranial Hemorrhage: Intensity changes on sequential MR scans at 0.5 T. *AJR* 150, 651, 1988.



Determination of absorbed dose distributions for radiotherapy using an MRI-scanner.

L. E. Olsson, Å. Ericsson, A. Fransson and S. Mattsson. Dep. Radiation Physics and Dep. of Radiology, Malmö and Uppsala University Hospital. Sweden.

Introduction

A clinical MRI-scanner is just not a diagnostic tool in medicine. It can also be used for quantitative measurements of i.e. the spin-lattice ( $T_1$ ) and spin-spin ( $T_2$ ) relaxation times. This quality may be used for determination of radiation absorbed dose distributions. The great advantage by using an MRI-scanner as a radiation detector is the possibility to measure the absorbed dose over a large volume at one time.

The principle is to use ferrous sulphate solution, in which ferric ions are produced during irradiation (1). The amount of ferric ions produced will be proportional to the absorbed dose. Since ferric ions are paramagnetic and the relaxation rate,  $R_1$  is proportional to the concentration of a paramagnetic ion (2) then  $R_1$  will proportional to the absorbed dose.

For radiotherapy it is of greatest interest if three-dimensional dose distributions can be measured within a radiation sensitive volume (phantom). Especially if the phantom could be shaped in irregular forms or even containing tissue mimicking materials i.e. bone. This may be possible if the ferrous sulphate solution can be gelled to a phantom. Several attempts have been done to do this (3,4,5,6).

Material and Methods

A new dosimeter, a dosimeter gel for MRI use has been developed. It consists of ferrous sulphate solution bound in a gel of agarose. The mixture of the gel was optimatized with respect to the sensitivity. The linearity, dose rate dependence and minimum detectable dose of this dosimeter gel were investigated in the following way: The preparations were done in a manner close to Olsson et al., 1989 (3). After preparation the gel was poured into glass-tubes. The irradiations (absorbed doses between 0- 40 Gy) were done using 6 MV photons from a linear accelerator. The mean dose rate was at most 12.4 Gy/min (0.69 mGy per pulse).  $T_1$  was measured at an NMR-analyser, 0.25 T (PRAXIS II).

A set of spin-echo images with different TR (100-3000 ms) of the tubes were measured at a Siemens Magnetron (0.5 T). A  $T_1$ -image of the irradiated gels were calculated according to Sperber et al. 1989 (8). Phantoms of Perspex were filled with dosimeter gel. They were then

irradiated with a simple electron or photon field. The absorbed doses were between 25- 35 Gy at the depth of dose maximum.

The phantoms were scanned as described above in the Magnetron before as well as after the irradiation. The slices were located both along and perpendicular to the central axis of radiation field. Relative depth dose curves as well as isodose curves were calculated.

Results

The dosimeter gel made of ferrous sulphate solution and agarose has a linear dose response relationship. This presumes that the gel has been bubbled with oxygen during preparation. The sensitivity of this gel is a factor of about 4-5 higher than conventional ferrous sulphate solution (Fricke solution). This means a  $G(Fe^{3+})$ -value of approx. 100 (100 eV<sup>-1</sup>). Higher values have been observed but not with the linearity unaffected. The dosimeter gel shows no dose rate dependence of dose rate (up to 12.4 Gy/min). The minimum detectable dose is below 1 Gy as measured with NMR-analyser. The  $T_1$  times measured at the Magnetron are longer than at the Praxis depending of the different field strengths. The linearity between relaxation rate and absorbed dose is, however, unaffected.

They by MRI-technique measured relative absorbed depth dose and isodose curves have shapes similar to corresponding curves measured by diodes.

References

1. Fricke, H. and Hart, E.J., Radiation dosimetry vol 2, (New York: Academic) pp 167-239, 1966.
2. Fukushima, E. and Roeder, S. Experimental pulse NMR (Massachusetts: Addison-Wesley).
3. Olsson, L.E., Petersson, S. and Persson, B., Läkarsällskapets riksstämma abstract (in Swedish), 1985.
4. Olsson, L.E., Petersson, S., et al. Phys. Med. Biol., 34, 43, 1989.
5. Appleby, A., Christman, E. A. and Leghrousz, A., Med. Phys. 14, 382, 1987.
6. Appleby, A., Leghrousz, A. and Cristman, E. A., Radiat. Phys. Chem., 32, 241, 1988.
7. Sperber, G. O., Ericsson, Å. and Hemmingsson, A., Magn. Reson. Med., 9, 113, 1989.

## PROTON CHEMICAL SHIFT IMAGING OF DIABETIC AMYOTROPHY

R.H. Griffey, B.V. Griffey, W.L. Sibbitt, R.R. Sibbitt, J. Bicknell, R.P. Eaton;  
Center for Non-Invasive Diagnosis, and Univ. of New Mexico School of Medicine

Purpose

Diabetic amyotrophy is clinically characterized by muscle weakness and rapid fatigue often associated with concomitant peripheral neuropathy. However, characterization of muscle abnormalities yields variable results, including primary myopathy or denervation. To better characterize this condition, we have studied 59 diabetics and 25 age-matched controls. The clinical symptoms were determined using a neurological examination based on motor, sensory, and reflex variables of the leg. These results are compared to measurements of relative hydration and lipid content of muscle performed using magnetic resonance spectroscopy (MRS). We demonstrate that proton chemical shift imaging can be used to identify diabetic patients with two conditions: patients with a 10-25% increase in the hydration of muscle fascicles; and patients where replacement of muscle tissue with lipid is occurring. The increased muscle hydration correlates with increased scores on the neurological muscle exam ( $p<0.1$ ). These results suggest that primary myopathy may be differentiated from denervation by chemical shift imaging.

Methods

Patients were screened for other complications, including nephropathy, retinopathy, and chronic exposure to alcohol.

MRS. All patients were studied at 1.5 T on a General Electric Signa system using the method of Dixon. The right ankle was placed in the extremity coil with a standard of 0.1 N copper sulfate secured to the ankle, and 9-13 images were acquired in the axial plane, corresponding to "in phase" and "out-of phase". The echo time was 20 msec, and the repetition time was 2500 msec. The field of view typically was 8 cm, and a 256x256 matrix of data points were obtained. The values for muscle hydration and lipid content were calculated from 1  $\text{cm}^2$  regions of the gastrocnemius in seven slices.

Neurological Muscle Exam. The evaluation of motor function assessed flexion and extension of the toes and ankles, and reflex testing. The results were graded to yield a score ranging from 0 to 24. Nerve conduction velocities also were determined using conventional methodology.(1)

Results

Normals. The mean value for the hydration level in the gastrocnemius of 25 normals is  $41.5 \pm 2.4\%$  of the copper sulfate standard. The value is independent of sex and age for men and women between 20-70 years old. No correlation was observed between the hydration level, the nerve conduction velocity, and the neurological exam.

Asymptomatic Diabetics. The mean muscle hydration for 22 diabetic patients without peripheral neuropathy is  $41.8 \pm 3.1\%$  of the standard. In 4 of these diabetics, the value is above 48% ( $>2 \text{ SD}$ ). No correlation was observed between the hydration level, the nerve conduction velocity, and the neurological muscle exam.

Diabetics with Peripheral Neuropathy. The mean muscle hydration for 37 diabetic patients with peripheral neuropathy is  $46.6 \pm 9.3\%$ . In 12 of the 37 patients, the hydration value was greater than 47%, with a mean of  $51.2 \pm 2.6\%$ . The 21 patients with hydration levels below 47% had a mean value of  $42.3 \pm 2.7\%$ . The increased level of water in muscle correlates with increased water in the sural nerve ( $p<0.05$ ) and with the score on the neurological muscle exam ( $p<0.1$ ).

Three patients with symptomatic neuropathy presented with lipid intensities in the muscle of 7% or greater, compared to the value of  $2 \pm 1\%$  in all other patients. The three patients all had greater than 48% muscle hydration. Five other symptomatic patients presented with replacement of muscle with adipose tissue as determined from the relative areas of high intensity (lipid) and low intensity (muscle) in the conventional MR image.

Conclusions

MRS analysis of muscle hydration and lipid content in diabetic patients provides a new quantitative description of diabetic myopathy. The extent to which this can be differentiated from primary neuropathy remains to be defined.

References

1. Griffey, R.H., Eaton, R.P., et al. J. Am. Med. Assoc., 260, 2872, 1988.

## MRI of Pituitary Disorders Utilizing Gadolinium-DTPA

M.J. Fenstermacher, M.D. Powers, C.M. Bonmati, and J.W. Yeakley  
 Department of Radiology, University of Texas Medical School  
 at Houston, TX 77030 USA

The role of MRI in the evaluation of suspected pituitary disorders has been documented and optimal techniques for imaging at 1.5 T have been described. (1) The recent widespread availability and approval of Gd-DTPA necessitates an examination of its usefulness in pituitary MRI. The purpose of this study was to describe an efficient pituitary protocol incorporating Gd-DTPA and to prospectively evaluate its utility in routine imaging.

Methods: Approximately 40 patients with suspected pituitary disorders were imaged on a 1.5 T GE Signa System. Pathologic or strong laboratory/clinical confirmation of the imaging diagnosis was obtainable in 35%. The population of disorders included pituitary adenoma (33%), craniopharyngioma (7%); Rathke's cleft cyst (7%), hypophysitis (7%); 33% of the studies were normal.

The protocol began with obtaining IV access prior to placing the patient in the scanner. Imaging prior to enhancement included sagittal TR 800/TE 20, 3mm/0.5 gap; coronal TR 2000/TE 20,80 3mm/0.5 gap; axial TR 2000/TE 20,80 24 FOV1 NEX 5mm/2.5 gap through entire brain; coronal TR 400/TE 20, 3mm interleaved, 4 NEX. Immediately following the IV administration of Gadolinium-DTPA (0.1 mmol/kg), the last sequence was repeated. Unless otherwise specified, FOV=16, NEX=2. Total imaging time was approximately 31 minutes. Image analysis included focal signal abnormalities, cavernous sinus integrity, involvement of adjacent structures such as chiasm, pituitary stalk and sphenoid sinus, and evaluation of the pattern of contrast enhancement in normal structures and focal lesions.

Results: All normal pituitary tissue enhanced in the same, homogeneous, slightly mottled fashion, the stalk enhanced to a slightly greater degree and the adjacent cavernous sinus venous blood enhanced intensely. All solid adenomas showed no significant qualitative enhancement. The two cystic prolactinomas in our series enhanced intensely on immediate post-contrast scans. The solid portions of the craniopharyngiomas also enhanced.

When comparing the pre- and post-contrast images, Gd-DTPA was helpful in approximately 55% of the cases. Of this group, contrast was particularly useful for excluding questionable lesions (20%), increasing the signal difference of subtle lesions (20%), staging of neoplasms relative to adjacent structures (27%), identifying residual normal pituitary tissue (13%), and indentifying atypical signal characteristics (13%). In a subset of 10 post-operative cases, Gd-DTPA was helpful in 5, particularly for evaluation of the chiasm, residual tumor margins, cavernous sinus extension and for differentiating post-operative tissues from adjacent normal structures.

Conclusion: Gd-DTPA is useful to confirm questionable lesions and improve lesion detectability, to accurately identify tumor margins and extent, and to evaluate post-operative patients. Contrast enhancement can be performed in an efficient manner for use in routine MRI of suspected pituitary disease.

1. Kulkarni, M.V. et al. AJNR, 9, 5, 1988.

## Liposomal Gadolinium DTPA Enhanced MR Imaging of Hepatic Metastases

E. Unger, M.D.<sup>1</sup>, P. MacDougall<sup>2</sup>, L. Fajardo, M.D.<sup>1</sup>, A. Zerella<sup>1</sup>, C. Tilcock, Ph.D.<sup>2</sup>  
 University of Arizona, Department of Radiology<sup>1</sup>, Tucson, Arizona 85724  
 University of British Columbia, Department of Biochemistry<sup>2</sup>, Vancouver, BC, Canada

Because liposomes are confined within the vascular space until broken down or cleared by specific cells, such as the reticuloendothelial system, liposome vesicles can deliver magnetic resonance (MR) imaging contrast agents to the vascular system, or specific sites such as the liver, spleen, and bone marrow.[1] Liposomal Gd-DTPA encapsulated within 70- and 400-nm vesicles was tested as a liver MR contrast agent in seven rats with hepatic metastases in doses of 0.1, 0.2, and 0.5 mmol/kg of Gd-DTPA. Liposomal Gd-DTPA caused significant improvement in contrast between liver and tumor ( $P < .005$ ) on T1-weighted MR images. The smaller 70-nm liposomal Gd-DTPA vesicles caused greater contrast enhancement than the larger vesicles, reflecting the larger surface area/volume ratio of the smaller vesicles. Liposomal Gd-DTPA postcontrast scans showed significant improvement in metastasis detection by five blinded radiologists ( $P < .005$ ), with detection of metastases as small as  $0.6 \times 1$  mm. By comparison, free Gd-DTPA without liposomes caused a statistically significant reduction in contrast between tumor and liver ( $P < .01$ ) compared with pre-contrast images, and a reduction in lesion detection by the five blinded radiologists ( $P < .01$ ).

The poor results with free Gd-DTPA likely reflect its rapid equilibration between intra- and extravascular spaces, with a concomitant reduction in contrast.[2,3] Liposomal Gd-DTPA also resulted in sustained vascular enhancement after contrast administration. Biodistribution studies were performed on Sprague-Dawley rats. Rats were injected IV with 0.1 millimole of Gd-DTPA encapsulated in either 100 nm or 30 nm egg phosphatidyl choline cholesterol (EPC/chol) vesicles, with  $^{153}\text{Gd}$ -DTPA label. Rats were killed at 15 mins., 1, 4, 24, and 48 hours, one and two weeks after IV liposomes injection. Biodistribution showed prolonged blood pool phase (longer for the 30 nm vesicles) with highest uptake in the spleen. Splenic bone marrow and liver uptake were higher for the 30 nm vesicles. The half-life for clearance of the  $^{153}\text{Gd}$ -DTPA from the liver and spleen was 3 1/2 days.

Rats were injected IV with 0.1 millimoles per kg of Gd-DTPA entrapped in either 30 nm or 100 nm Gd-DTPA liposomes (6:4 EPC/Chol) with 5 rats studied with each preparation and MR images obtained at 15 min., 1, 4, 24 and 48 hours post injection. Similarly, 5 rats were studied as controls after IV injection of 0.1 millimoles/kg of free Gd-DTPA. Signal intensity of liver, muscle, blood, kidney and urine was measured post contrast. The post-contrast enhancement followed a similar pattern as observed on the biodistribution studies with greater enhancement caused by the 30 nm Gd-DTPA vesicles than the larger 100 nm liposomes. Liposomal enhancement differed markedly from that of free Gd-DTPA, reflecting the differences in biodistribution of liposomal and free Gd-DTPA.[3-5]

Clearance was studied in Sprague-Dawley rats injected IV with 0.1 mole of Gd-DTPA encapsulated in 100 nm egg phosphatidyl choline vesicles. Approximately two-thirds of the clearance occurred via the urine, and one-third via the feces.

Although our in vitro work shows that the 30 nm liposomes are less stable in serum, biodistribution indicates that they are sufficiently stable in vivo for prolonged blood pool phase and delivery of Gd-DTPA to liver, spleen, and bone marrow. Clearance of liposomal Gd-DTPA occurs suggesting that retention, or potential dechelation may not be a problem. These results are encouraging and suggest that liposomal MR contrast agents may eventually be studied in clinical trials.

References

1. Unger, E.C., P. Needleman, P. Cullis, et al. *Invest. Radiol.*, 23, 928, 1988.
2. Carr, D.H., M. Graif, H. Niendorf, et al. *Invest. Radiol.*, 37, 347-353, 1986.
3. Unger, E.C., T. Winokur, P. MacDougall, et al. *Radiol.*, 171, 81-85, 1989.
4. Weinmann H.J., R. Brasch, W. Press, et al. *AJR*, 142, 213-222, 1985.
5. Brasch, R.C., H. Weinmann, G. Wesbey. *AJR*, 142, 625-630, 1984.

Oral Magnetic Particles (OMP): A New Oral Contrast Agent For Abdominal MR Imaging

D Kean, J Best, L Turnbull, J Ridgway, H McRitchie, D Carter, M Wright  
 Depts. of Radiology and Surgery, University of Edinburgh, Nycomed AS Oslo

Introduction

There are two principal methods of labelling the bowel in abdominal MRI. The first is to use "positive" contrast agents such as gadolinium DTPA and clinical results using this method have been demonstrated (ref. 1). The second is to use a "negative" contrast agent which will produce a signal void in bowel loops by means of shortening the T2 relaxation time. Such a contrast agent has been formulated by Nycomed AS and preliminary results have been presented (ref. 2). The contrast agent consists of an aggregate of small ferromagnetic crystals (magnetite) supported on an inert, spherically shaped particle of monosized (mono-disperse) type. The overall size of the particles is approximately  $3.7 \mu\text{m}$ .

IN VITRO STUDIES

These were performed to determine the optimum concentration, orientation relative to Bo and pulse sequence to be employed with a 0.08 Tesla vertical field magnetic resonance system. From these studies it was demonstrated that the optimum concentration of oral magnetic particles (OMP) was 0.1 gram per litre. Above this concentration image artefacts were produced. These consisted of loss of signal from the boundary of the sample and these artefacts increased with increasing concentration of OMP. The degree of artefact was also dependent on the orientation of the sample relative to Bo. Serious artefacts were produced in the sagittal and transverse planes and the optimum orientation was the coronal plane i.e. with the orientation of the sample parallel to Bo. The severity of the artefacts was also dependent on the pulse sequence used. Field echo sequences produced the most serious artefacts.

IN VIVO STUDIES

Results from volunteer experiments showed that the optimum dose of the agent for labelling the upper small bowel was 600ml of OMP (0.1 gram per litre) 10 minutes before scanning of the upper abdomen. An interleaved SR/IR sequence (TR 1 sec T1 200msecs) was used to image the abdomen using transverse and coronal planes. Transverse images were repeated after 20 minutes to assess the passage of OMP into distal small bowel. The problems of artefact production which had been anticipated from the in vitro experiments were not significant in in vivo imaging and they did not

impair visualisation of the upper abdominal viscera in either the transverse or coronal planes.

Ten patients with acute pancreatitis have also been examined using the same examination protocol. OMP consistently labelled the upper GI Tract in these patients and permitted accurate visualisation and quantification of upper abdominal inflammation which, without bowel labelling can be difficult to assess due to the inflammatory fluid merging with long relaxation time bowel contents. No side effects were encountered in these patients studies.

The labelling of the distal small bowel and colon was less reliable in patients and volunteers and it is obvious larger volumes of the contrast agent will be required perhaps with the addition of an agent to increase its viscosity if reliable results in distal small bowel and colon are to be obtained. However the initial results from patients and volunteers show great promise for the use of OMP at least in upper abdominal MR imaging.

References

1. Kaminsky, S., Laniado, M., Kornmesser, C. D., et al. Proc. Second European Congress of NMR in Medicine and Biology, Berlin. June 23-26 June 1988; poster 45.
2. Oksendal, A., Moxnes, A., Bach-Gansmo, T., et al. Proc. Second European Congress of NMR in Medicine and Biology, Berlin. June 23-26 1988; paper 163.

MRI Oral Contrast Agents: Comparative Study of Five Potential Agents in Humans

K.C.P. Li, R.P. Tart, B. Storm, R. Rolfs, P. Ang, P.R. Ros  
 Radiology Department, University of Florida, Gainesville, FL 32610 USA

Introduction

It is now generally accepted that a safe, inexpensive, effective MRI oral contrast agent is required for optimal MR imaging of the abdomen. The purpose of this investigation is to compare five widely available potential MRI oral contrast agents in terms of patient acceptance and imaging properties in human volunteers.

Methods

The five agents studied were: (1) Ferric ammonium citrate, formulated by diluting 8 ml of Geritol in 500 ml of water with a final concentration of 1 mM, (2) 12% corn oil emulsion, prepared by blending 473 ml of homogenized milk, 3 scoops of vanilla ice cream and 60 ml of corn oil, (3) Kaolin-Pectin (UDL Lab.), 500 ml, (4) Single contrast oral barium sulfate suspension at 60% w/w (E-Z-M), 2 cups, (5) E-Z-Gas II effervescent granules (E-Z-M), 2 packets, which should produce no less than 400 ml of CO<sub>2</sub> per packet. Five informed volunteers were recruited. Each volunteer ingested each of the five contrast agents on separate occasions and were then imaged using a 1.5 T Magnetom imager. The first 4 agents were ingested evenly throughout a 2 hour period prior to scanning after the volunteers were kept N.P.O. for at least 4 hours. The effervescent granules were administered immediately prior to imaging with sips of water. No other medication was administered. Coronal 10 mm contiguous sections of the abdomen were obtained using SE 500/22, SE 2500/45/90 and FISP 40/18/40° pulse sequences. Axial 10 mm contiguous sections of the abdomen from diaphragm to iliac crest were also obtained using FISP 40/18/40°. Questionnaires regarding patient acceptance and complications of the contrast agents were filled out by each volunteer after each session. The images were then reviewed to evaluate the ability of the contrast agent to opacify the gastrointestinal tract to enhance visualization of the different abdominal organs. The delineation of the abdominal organs were scored on a scale of 1 to 5, 1 being very poor and 5 being excellent.

Results

The oil emulsions were best tolerated by the participants. On a scale of 1 to 5, 1 being great overall and 5 being intolerable, the average score of oil emulsion was 1.0. The average overall scores for CO<sub>2</sub>, Kaolin-Pectin, barium sulfate and Geritol were 2.0, 2.8, 2.9 and 3.0, respectively. Barium

sulfate caused the greatest amount of nausea, followed by Geritol and Kaolin-Pectin. No nausea was encountered with oil emulsions and CO<sub>2</sub>. Mild constipation and abdominal cramps were associated with the use of barium sulfate and Kaolin-Pectin. No nausea, change of bowel habits or abdominal discomfort were associated with the use of oil emulsions or CO<sub>2</sub>.

The opacification of the gastrointestinal tract was most pronounced when FISP 40/18/40° was used. With this pulse sequence, 60 to 80% of the small bowel was well delineated using Kaolin-Pectin, oil emulsion, or barium sulfate. The best opacification was achieved with Kaolin-Pectin with close to 80% of small bowel loops opacified, followed by oil emulsions and barium sulfate. With Geritol and CO<sub>2</sub> less than 60% of the small bowel loops were opacified. The pancreatic head was best visualized using barium sulfate (average score 4.25) and the pancreatic body and tail were best seen with oil emulsion (average score 4.2 and 3.8). The colon was well delineated mainly due to the air within it and appeared to be independent of the small bowel opacification. With the SE 55/22 and SE 2000/45/90 pulse sequences, the small bowel was well delineated only with oil emulsion, where 60-80% of small bowel loops were well visualized. The delineation of the pancreas was poor, regardless of the contrast agent used.

Conclusion

Oil emulsion was by far the best MRI oral contrast agent in our study. Good delineation of the small bowel, pancreas and other abdominal organs can be achieved using this and gradient echo pulse sequences. The lack of side effects and the excellent taste makes it highly acceptable to human subjects.

## Superparamagnetic Particles as an Oral MR Imaging Contrast Medium

\*M. Lönnemark, \*A. Hemmingsson, \*\*T. Bach-Gansmo, \*A. Ericsson, \*\*A. Oksendal, \*R. Nyman  
 \*Dept of Diagnostic Radiology, University Hospital, Uppsala, Sweden, \*\*Nycomed AS, Oslo, Norway

Introduction

A new superparamagnetic oral MRI contrast medium (Nycomed AS, Norway) that reduces the signal intensity in the bowel loops due to T2 shortening has been developed.

Material and methods

The contrast medium consists of monodisperse resin carrier particles with a diameter of approximately  $3.5 \mu\text{m}$  and containing 20% magnetic iron oxide.

The contrast medium has been evaluated in 25 volunteers given the contrast medium in the concentration of 0.05 to 2.5 g/l. Patients with malignant lymphoma and probable enlarged lymph nodes in the abdomen were given 0.5 g/l. T1 and T2 weighted as well as proton density weighted sequences were applied.

In addition, a phase contrast and a gradient echo sequence were used in examinations of the volunteers.

Results

With spin echo sequences the contrast effect was sufficient at intermediate concentrations, but too weak at 0.05 g/l. At 2.5 g/l the effect was too strong and artifacts and blurring of the images were observed. Lower doses were needed with phase contrast and gradient echo sequences. In patients with malignant lymphoma the contrast medium facilitated the evaluation of normal and pathologic lymph nodes.

The contrast medium did not cause any adverse effects. As in other examinations with gastrointestinal contrast media, the largest problem was to achieve a satisfactory distribution of the preparation in the bowel loops. A new preparation - containing viscosity increasing agents - is therefore tested.

Conclusion

The results indicate that the contrast medium is well tolerated, gives a good contrast effect and increases the diagnostic possibilities in abdominal MRI.

References

1. Hahn PF, Stark DD, Saini S, Lewis JM, Wittenberg J, Ferrucci JT. Ferrite Particles for Bowel Contrast in MR Imaging; Design Issues and Feasibility Studies. *Radiology* 1987;164:37-41.
2. Mendoca Dias MH, Bernardo ML, Muller RN, Acuff V, Lauterbur PC. Ferromagnetic particles as contrast agents for magnetic resonance imaging. *Society of Magnetic Resonance in Medicine, Abstract* 1985:II, 887.
3. Widder DJ, Edelman RR, Grief WL, Monda L. Magnetite Albumin Suspension: A superparamagnetic oral MR contrast agent. *AJR* 1987;149:839-843.

**Carbontetrachloride- and 1,2-dibromoethane-induced liver lesions in rat liver studied by MRI spectroscopy: contrast enhanced by dextran magnetite.**

R. Davolio-Marani, M. Federico, A. Iannone, R.L. Magin, H.M. Swartz,

A. Tomasi, and V. Vannini.

University of Modena, Medical School (Italy) and University of Illinois,  
Urbana IL 61801 (USA).

**Introduction**

$\text{CCl}_4$  toxicity depends on its activation to trichloromethyl free radical in the endoplasmic reticulum. Cytochrome P-450, particularly the isozyme induced by phenobarbitone, bioactivates the halocompound. This first step is followed by a host of related toxic mechanism, including induction of lipid peroxidation, covalent binding to proteins, lipids and DNA of the trichloromethyl free radical, leading to cell lesion and death (1).

1,2-dibromoethane (DBE) toxicity is induced by a mechanism quite different from that described for  $\text{CCl}_4$ . DBE induces a rapid depletion of hepatic and mitochondrial glutathione (GSH) *in vivo* and *in vitro* (2), its GSH-derivative metabolites are genotoxic, the acute toxicity is much higher than that of  $\text{CCl}_4$ .

In this study we describe the development of the liver lesion as seen by proton Magnetic Resonance Imaging (MRI) after  $\text{CCl}_4$  or DBE treatment with or without the concurrent presence of dextran magnetite (DM), a ferrite particle with superparamagnetic propert (3).

DM is a potential contrast agent for MRI with spin-lattice and spin-spin relaxivities higher than those exhibited by paramagnetic colloids (4). Its clearance is fast and is due to uptake by the RE cells of liver and spleen.

**Materials and Methods:**

$\text{CCl}_4$  (0.2 ml/kg b. w.) or DBE (5  $\mu\text{l}/100 \text{ g b.w.}$ ) was administered per os dissolved in mineral oil. Dextran magnetite (DM) was obtained from Meito Sangyo Co. (Nagoya, Japan). The ferrite particles contained 546 mg magnetite, 395 mg iron and 221 mg dextran per ml. Rats were injected i.v., 15 mg/kg, with a DM suspension, 3 mg/ml final concentration.

Animals were inserted in the MRI superconductive unit light nembutal anesthesia at 0, 4 and 16 hours after toxicant administration. The pictures were taken using a Sigma General electric Medical System (Milwaukee, USA) provided with a superconductive unit operating at 1.5 T (bore diameter 60 cm). A cylindrical surface coil, both receiving and transmitting, has been employed for Spin echo coronal and axial scans weighted in  $T_1$  ( $\text{TR}/\text{te} = 400/20 \text{ ms}$ ) and  $T_2$ . Asymmetric spin echo where  $\text{TR}/\text{te} = 2000/20$  and  $80 \text{ ms}$ ). The field of view was ca 8-10 cm and a slice thickness 5 mm. Liver images were taken in control and treated rats

before and 5 min. after the i.v. DM injection (15 mg/kg b.w.).

**Results and Discussion.**

First, control rats were examined with or without DM. DM injection caused a dramatic decrease in the density of the liver image. The liver of  $\text{CCl}_4$  treated rats showed a hyperintense area, in the

$T_2$  weighted image, whose blurry contour was centered on the perihilar area. The lesion was much more apparent when DM was injected, giving a hyperintense area well differentiated from the low signal of the normal surrounding liver.

Focal lesions were not apparent in the liver of DBE treated rats either in the presence or absence of DM. However a severe vasodilation was manifest in images weighted in  $T_1$  and  $T_2$  with or without DM.

**Conclusions**

The present study demonstrate the usefulness of the MRI approach in studying *in vivo* experimental liver lesions. Being this parenchymatous organ rather difficult to study through MRI, we have tried and found the usefulness of DM as a potential contrast agent.

**References**

- 1) Cheeseman K.H., Albano E., Tomasi A., Slater T.F., Env. Health Persp. 64, 85, 1985.
- 2) Botti B., Ceccarelli D., Tomasi A., Vannini, V., Muscatello U., and A.Masini. Biochim. Biophys. Acta in press 1989
- 3) Renshaw P.F., Blum H., Leigh J.S. Jr , J. Magn. Res., 69, 523, 1986.
- 4) Olsson M.B.E., Persson B.R.B., Salford L.G. and Schroeder U. Magn. Reson. Imag., 4, 437, 1986

## Tissue Distribution of Dextran Magnetite in the Rat Studied by ESR Spectroscopy

M. Federico\*, A. Iannone, R.L. Magin, R.B. Clarkson, R. Sabbatini\*, H.M. Swartz, A. Tomasi\*, and V. Vannini\*  
 \*University of Modena, Medical School (Italy) and University of Illinois, Urbana IL 61801 (USA)

**Introduction** Dextran magnetite (DM) is a potential contrast agent with superparamagnetic properties. The spin-lattice and spin-spin relaxivities of DM are higher than those exhibited by paramagnetic colloids. In addition, its fast clearance and selective uptake by liver and spleen macrophages provide advantages for imaging tumors in these organs.

Previously, the distribution of DM particles in various organs was assessed using radiolabels, histochemical reactions, or NMR measurements of its effect on tissue relaxation. These studies showed a marked increase in iron content of liver, spleen, and lung; tissues which have an active population of fixed macrophages.

We recently noted that DM suspensions give rise to an easily detected ESR signal. The DM-related ESR signal can be measured with high sensitivity at room temperature. The ESR signal is stable with time and can be recorded in minutes. The spectra obtained from DM in saline, blood, and tissue samples were similar so that the relative concentration of DM can be estimated. In this study we report measurements of the tissue distribution of DM in rats obtained using this novel ESR technique.

**Materials and Methods** Dextran magnetite (DM) was obtained from Meito Sangyo Co. (Nagoya, Japan). The particles contained 546 mg magnetite per ml, 395 mg iron per ml and 221 mg dextran per ml.

Rats were injected i.v. at a dose of 69  $\mu\text{mol Fe/kg}$  using a DM suspension of 13.7 mM. Animals were sacrificed at various times and blood and tissue samples were immediately collected in 25  $\mu\text{l}$  capillary tubes. Samples were kept at 4 °C until the ESR measurements were performed, always within 4 hours.

**ESR measurements:** A Bruker (X-band) spectrometer was used. The instrumental settings were: field width 6000 G, modulation amplitude 5 G, microwave power 50 mW, field center 3390 G, room temperature. ESR spectra exhibited complex lineshapes with components similar to those observed in other  $\text{Fe}_3\text{O}_4$  particle systems. A broad resonance line attributable to ferrimagnetic resonance is seen in conjunction with a much sharper line from superparamagnetic particles. A calibration curve was made by measuring the peak height of the first derivative spectrum obtained from samples containing standard concentrations of DM.

**Light microscopy:** Tissue sections (spleen and liver) were fixed. The Pearl's Prussian blue iron reaction for trivalent iron was used in order to assess storage iron content.

**Results and Discussion** Dextran magnetite clearance from blood after i.v. injection was measured using ESR spectroscopy. The time course for DM elimination from blood (Fig. 1)

shows a steep decline (half life = 6 min); DM was reduced to less than 10% of the initial value in 90 minutes.

DM concentration was then measured in the liver and spleen (Fig. 2). DM in liver reached a plateau within minutes after the i.v. injection, while quantity in the spleen increased slowly for 90 min. This behavior suggests an initial phase, where the signal intensity essentially reflects blood levels, and a late phase, related to phagocytic activity.

The ESR signal intensity in the spleen was about three times higher than that in the liver on an equal weight basis. This suggests that in the spleen DM uptake is highly efficient and related to its high phagocytic activity. These findings were confirmed by histological examination of spleen and liver specimens. The presence of DM related iron, as demonstrated by specific staining, was restricted to the reticuloendothelial cells in both organs.

**Conclusion** ESR measurements provide a simple and convenient technique for detecting DM in blood and various biological tissues. It is likely that this method could also be applied to other superparamagnetic particles like DM that are currently undergoing clinical evaluation as MR contrast agents. In addition, DM-related signal is stable and dependent on the concentration in the sample.

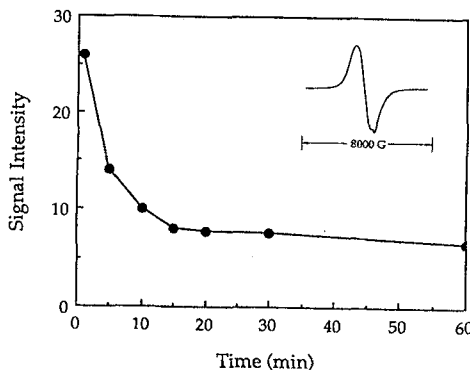


Figure 1. Blood clearance of dextran magnetite after i.v. injection.

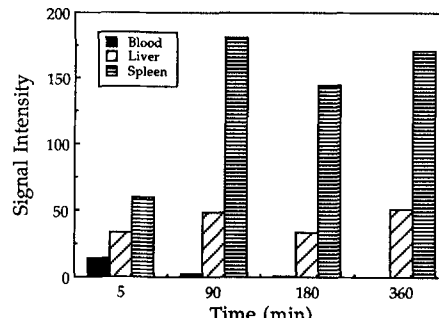


Figure 2. Tissue distribution of dextran magnetite after i.v. injection.

## Improving Tumor-to-Liver Contrast Using Dextran Magnetite

R. L. Magin, G. Bacic, M. R. Niesman, J. C. Alameda Jr, S. M. Wright, H. M. Swartz  
University of Illinois, Urbana, IL 61801

**Introduction** A selective liver contrast agent is needed to improve the ability of magnetic resonance imaging to detect primary and metastatic liver tumors. The recent development of superparamagnetic particles as contrast agents established a new approach to this problem. These agents are rapidly removed from the blood by fixed liver macrophages and are effective at enhancing the  $T_2$  relaxation rate of normal liver and spleen, but not tumor tissues. Therefore, by using the appropriate  $T_2$  weighted image sequence, excellent contrast is obtained between the tumor and surrounding normal tissue at very low doses.

Dextran magnetite is one such superparamagnetic particle whose potential as an MRI contrast agent has not yet been studied completely. Although dextran magnetite was one of the first superparamagnetic particles recognized to provide selective  $T_2$  relaxation enhancement, it was not tested *in vivo* until recently. The small size (30-50 nm) and the high relaxivity of the dextran magnetite particle are characteristics that provide potential advantages for selective tumor imaging. In addition, dextran magnetite appears to be metabolized in the liver faster than other types of ferrite particles. The purpose of this study was to analyze carefully the physical and biological properties of dextran magnetite that influence its use as a contrast agent.

**Materials and Methods** A suspension of dextran-coated magnetite particles was obtained for this study from Meito Sangyo Co. Ltd. (Nagoya, Japan). Dextran magnetite particles consist of small (10-20 nm) magnetite ( $Fe_3O_4$ ) cores coated with the hydrophylic polymer dextran to an overall particle diameter of 30-50 nm. Analysis by Meito Sangyo indicated that the suspension had a magnetite, iron, and dextran content of 546, 395, and 221 mg/ml respectively, and a density of 1.54 g/ml. A stock solution containing 229.6 micromol Fe/ml was made by the appropriate dilution in sterile Hepes buffered saline.

The animal tumor model used was a mammary adenocarcinoma (R3230AC) acquired from Biomeasure Inc. (Hopkinton MA). This tumor arises spontaneously in female Fisher 344 rats, and when implanted subcutaneously forms a well encapsulated, nearly spherical mass.

**NMR Relaxation Measurements** After administration of dextran magnetite, the longitudinal and transverse proton relaxation rates for liver, spleen, and tumor were measured *in vitro*, at 20 MHz using an IBM-Bruker PC-20 relaxometer.

**Imaging** Images were obtained using the 0.50 T Siemens Magnetom whole body imaging system (St. Francis Medical Center, Peoria, IL). The rats were anesthetized with an i.m. injection of a mixture of ketamine (100 mg/kg) and acepromazine (1 mg/kg) immediately prior to

positioning in the head coil for imaging. Contrast agent was administered via a 25 gauge butterfly catheter implanted in the tail vein of the rats so as to allow injection without removal of the rats from the magnet. The dextran magnetite was injected i.v. at a volume of 5ml/kg.

**Histology** Light microscopy was used to study the distribution of dextran magnetite particles. The liver, spleen, and tumor were removed from animals sacrificed at 1 hour, 1 day, and 1 week after injection of dextran magnetite (69 or 690 micromol Fe/kg). After fixation in 10 percent buffered formalin, the tissue samples were imbedded in paraffin blocks and sectioned at a thickness of 10 microns. The Prussian blue iron reaction with safranin counterstain was used to visualize the location of ferric iron within each tissue section.

**Results** Dextran magnetite substantially reduced the  $T_2$  of the liver and spleen, but not of the tumor; thus providing a basis for improved tumor imaging. A larger  $T_2$  reduction was measured in these tissues using the Hahn spin echo method instead of the CPMG technique. This is reasonable because the CPMG pulse sequence compensates in part for the diffusion of water through magnetic field inhomogeneities like those produced by dextran magnetite. The  $T_1$  of the tumor was not affected following injection of dextran magnetite in the dose range studied, while the spleen  $T_1$  was reduced substantially more than the  $T_1$  of the liver. Histological studies using the iron reaction for Prussian blue clearly showed dextran magnetite in the liver and spleen, but not in the tumor. While dextran magnetite was sequestered in macrophages in both liver and spleen, the distribution in the liver was more diffuse (70 micron particle separation) than that in the spleen (25 micron). The lack of a  $T_1$  effect in the liver is consistent with the fact that water cannot diffuse to the relaxational centers on the time scale of the liver's intrinsic  $T_1$  (280 ms). In the spleen, however, the dextran magnetite is more densely packed in the red pulp allowing a significant fraction of the water to be relaxed by a  $T_1$  mechanism. Spin echo images of the implanted tumor (mammary adenocarcinoma, R3230AC) in the livers of Fisher 344 rats were obtained at 0.50 T (Siemens Magnetom). The tumor-to-liver contrast was improved for both  $T_1$  and  $T_2$  weighted spin echo images after intravenous injection of the dextran magnetite contrast agent. The contrast determined from these images agreed with that predicted by the measured  $T_1$  and the  $T_2$  (Hahn spin echo) values. In addition, gradient echo  $T_2$  weighted images with good contrast were obtained in a much shorter imaging time than was needed for  $T_2$  weighted spin echo images. These results demonstrate that the MRI contrast enhancement observed with dextran magnetite is based on its selective uptake and distribution in the macrophages in the liver and spleen and that this agent has substantial potential as a superparamagnetic MR contrast agent.

**MRI Contrast-Dose Relationship at 2.0 Tesla for Human Xenograft Tumors in Nude Mice with  
Manganese(III)tetra(4-sulfonatophenyl) Porphyrin**

David A. Place<sup>1,2</sup>, Peter C.M. van Zijl<sup>1</sup>, Patrick J. Faustino<sup>1</sup>, A. Scott Chessnick<sup>1</sup>, and Jack S. Cohen<sup>1</sup>

<sup>1</sup>National Cancer Institute, National Institutes of Health, Bethesda, MD 20892, USA

and <sup>2</sup>Institut für Diagnostikforschung, 1000 Berlin 19, FRG

### Introduction

Previously we reported that Mn(III)tetra(4-sulfonatophenyl) porphyrin, MnTPPS4, a water-soluble paramagnetic metalloporphyrin, is a contrast agent which can effectively enhance tumor detection by MRI<sup>1</sup>. Its low toxicity, selective accumulation in tumors, and MRI contrast enhancement in tumor-bearing nude mice have also been documented.<sup>2</sup> We have continued our studies of this agent in order to further understand the mode of action of MnTPPS4. Results from MRI are correlated with experiments on intact tumors and tumor cell cultures.

### Objectives

Our present efforts center on the experimental determination of dose-contrast relationships over a wide range of dosages in order to determine the lowest dose as well as the best administration method for obtaining visible MRI tumor contrast enhancement.

### Instrumentation

Recent instrumentation advances at the NIH *in vivo* NMR Center allow much higher resolution than in earlier reported images. Spin Echo (SE) and Inversion Recovery (IR) images have been obtained on a 2T GE CSI equipped with shielded gradients. A custom-designed birdcage coil, which accommodates one mouse, is being utilized. The combination of optimized probe design, higher field strength, and state-of-the-art gradients affords high S/N, small pixel size, and effective data acquisition.

### Methods

Sterile filtered solutions (0.01 to 0.02 M) of MnTPPS4 (Midcentury Chemical Co., Posen, IL) were used. Athymic nude mice, bearing subcutaneous MCF-7 human breast carcinoma xenografts were injected with intraperitoneal (IP) doses ranging from 0.025 to 0.5 mmol/Kg. The anesthetized mice were imaged before and after MnTPPS4 administration. Images of 2 mm thickness were obtained which include the tumor and a full coronal cross-section of the mouse for image contrast comparison.

### Method of agent administration

Because of the moderate solubility of MnTPPS4, the injected volume of agent for high doses exceeded the allowable volume for single-bolus IV injections. IP administration has been chosen to eliminate this difficulty. In addition, we were interested in whether a more gradual vascular uptake and distribution of the agent, such as IP injection provides, would lead to improved contrast enhancement.

### Results

In order to determine contrast enhancement, several imaging techniques have been employed. SE images with a range of levels of T<sub>1</sub> and T<sub>2</sub> weighting have been obtained. Substantial systemic relaxation enhancement is observed on T<sub>1</sub>-weighted images shortly after injection, but good tumor enhancement is not apparent until one day after injection, when the background level from the normal tissues has decreased. Individual doses of 0.025 and 0.05 mmol/Kg do not produce visible image enhancement. Single doses of 0.1 mmol/Kg or greater appear to be necessary to produce a detectable effect. At a level of 0.5 mmol/Kg, marked enhancement is produced, the effects of which can be readily observed beyond one week postinjection. Although the contrast effects of lower doses are not readily apparent in the series of SE images, a T<sub>1</sub> difference analysis at short TE values may prove useful for these clinically relevant lower dosages. This will be correlated with results of inversion recovery images.

Results will also be presented on the effectiveness of multiple small dosages administered over the course of several days before imaging, as well as a prognosis for the clinical utility of MnTPPS4.

### References

1. Patronas, N.J., et al, *Cancer Treat. Rep.*, **70**, 391, 1986.
2. Lyon, R. C., et al, *Mag. Res. Med.*, **4**, 24, 1987.

## Characterization of Paramagnetic Contrast Agents by Magnetic Resonance Methods

Jong-Hee Hwang, Martha J. Tanner, R. L. Belford, and R. B. Clarkson  
Illinois ESR Research Center, University of Illinois, Urbana, IL 61801 USA

### Introduction

The overall goal of this work is the physical characterization of factors controlling relaxivity in MRI contrast agents (CA's) and the quantitative determination of their mode of action on a molecular scale, in order to provide information useful in the design of more effective agents. The pioneering work of Koenig, Brown, and colleagues has shown that NMRD measurements often provide information that can be theoretically modeled in order to determine most of the key factors (e.g. [1]). Since it is frequently difficult to determine these parameters uniquely, complementary spectroscopic measurements are most useful. Our approach is to measure the physical properties of paramagnetic CA's with multi-frequency EPR, Electron-Nuclear Double Resonance (ENDOR), Electron Spin Echo (ESE), NMR, and NMRD, and to develop a set of self-consistent values for the key parameters. While each of these techniques has been used individually to study CA's, the application of all of them to the same system has not been attempted until now. Direct measurements of the factors controlling relaxivity in a series of simple Gd(III) chelates can be shown to correlate well with values calculated from NMRD curves, and the correlation is sensitive to the choice of physical models, which provides a check on the validity of model assumptions.

### Multi-Frequency EPR

Solutions of Gd(III) chelated with EDTA, DTPA, TTHA, and other simple amino polyacetic acid ligands are prepared using  $H_2O/MeOH$  or  $H_2O/glycerol$  as solvents. Solutions are frozen as glasses, and EPR measurements at L (1-2 GHz), X (9.5 GHz), and Q (35 GHz) bands are made at liquid helium temperatures. Spectra are analyzed by means of theoretical simulations [2]. Analyses of the data give the zero field splitting parameter ( $D^2 + E^2/3$ ), among other parameters. Similar solutions of Gd(III) chelates measured by EPR at room temperature and above provide lineshape data from which electronic spin relaxation times may be calculated.

### ENDOR and ESE

Measurements of frozen glasses of the Gd(III) chelates by ENDOR and ESE techniques are analyzed to obtain structural information about the complexes and their associated waters of hydration. The two spectroscopies provide complementary data on the ion-water distances ( $r$ ), the number of inner sphere and "middle sphere" waters organized by the agents, and the isotropic hyperfine coupling constant,  $A_{iso}$ .

### $^{17}O$ NMR

Measurements of  $T_1$  and  $T_2$  from inversion recovery, CPMG, and lineshape analysis are made on the O-17 nucleus in enriched water solutions of the Gd(III) chelates as functions of temperature. Data analyses by the methods described by Merbach, et al. [3], yield the inner sphere water exchange rate and the number of inner sphere water molecules. Figure 1 shows data for GdEDTA.

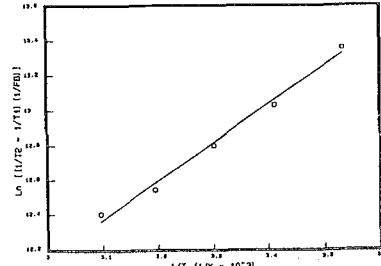


Figure 1. O-17 NMR relaxation measurements.  
(○) data.  
(—) theory.

For DTPA-complexed Gd(III), significant departures from the linear behavior shown in Figure 1. are observed. We attribute this curvature to the temperature-dependent inner sphere water equilibrium:  $GdDTPA + H_2O \rightleftharpoons GdDTPA \cdot H_2O$ .

### NMRD

NMRD measurements are made on all systems using an instrument designed by S. A. Koenig [1]. Data are currently analyzed through simulations employing the Solomon-Bloembergen-Morgan model for relaxation enhancement.

### Results

A self-consistent set of parameters measured by our multi-spectroscopic approach on GdEDTA is shown in Table I. Similar data for GdDTPA, GdTTHA, and other simple Gd(III) chelates are also presented.

(Work partially supported by grants from the NIH (RR 01811) and Schering, AG.)

- Brown, R. D., III, Brewer, C. F., and Koenig, S. H., *Biochemistry*, **16**, 3883, 1977.
- Belford, R. L., Clarkson, R. B., et. al., in *Electron Magnetic Resonance of the Solid State*, Weil, J. A., ed., Chemical Institute of Canada, Ottawa, 1987.
- Southwood-Jones, R. V., Earl, W. L., Newman, K. E., and Merbach, A. E., *J. Chem. Phys.*, **73**, 5909, 1980.

TABLE I. Some Data on Gd EDTA at 21.6°C

Measurement	$r(\text{\AA})$	$q$	$(D^2 + E^2/3)$ (sec $^{-2}$ )	$T_{1e}$ (nsec)	$T_{2e}$ (nsec)	$\tau_M$ (nsec)	$\tau_R$ (psec)	$A_{iso}$ (MHz)
Multi-freq. EPR			$1.6 \times 10^{17}$					
Solution EPR					.22			
ESE/ENDOR	2.6	2						1.9
O-17 NMR		2				3.7		
NMRD	2.9	2	$1.4 \times 10^{17}$	.22	.20	4.5	57	1.95

## NMR Study of Relaxivity of Lanthanide Ions - Potentiality for use in MRI

J Ewen Rimmington, N Roberts, MA Foster  
 Department of Biomedical Physics, University of Aberdeen, Scotland, U.K.

Introduction

Gd<sup>3+</sup>, which is widely used in MRI, is a very effective relaxation agent for water protons. Gadolinium is from the middle of the third transition series (lanthanides) and we have examined the relaxation-enhancing ability of other lanthanides as aquions, chelated with ethylene diamine tetraacetic acid (EDTA) and in agarose gels. The relaxivity of these ions has little dependence on measurement temperature or frequency which indicates possible uses for MRI test objects, but their low overall relaxivity precludes use as *in vivo* contrast agents.

Methods

The trivalent ions listed in Table 1 were dissolved in water at pH3. Eu<sup>2+</sup> was prepared from Eu<sup>203</sup> in acid solution and examined immediately since oxidation is rapid. Chelates of Gd, Dy and Er with EDTA, at 2 moles lanthanide to 3 moles EDTA, were prepared at pH7.2. Agarose (2% w/v) was boiled in Dy solution for 20 minutes to produce a doped gel.

A home-built relaxation spectrometer gave measurements at 2.5MHz. T1 was from a 15 point inversion recovery/Hahn echo sequence with tau from about 0.1 to 3.0 x T1. T2 was from a 100 echo Carr Purcell Meiboom Gill sequence with tau 4ms. Multi-frequency studies were on a Bruker CXP100. T1 was from a 20 point IR sequence from 0.1 - 2.0 x T1. T2 was from a CPMG sequence with tau 1ms, the echo train extending to about 2 x T2. Temperature was controlled to +/- 1°C. Results were calculated as monoexponentials.

Results

Table 1. Relaxivity (/mM.s) of tripositive lanthanide ions at 2.5MHz, 30°C.

Lanthanide	Atomic Number	E*	T1	T2
			Relaxivity	
Aqueous Solutions				
Cerium	58	1	0.007	**
Samarium	62	5	0.003	**
Gadolinium	64	7	24.4	22.0
Terbium	65	6	0.321	0.320
Dysprosium	66	5	0.342	0.349
Holmium	67	4	0.359	0.365
Erbium	68	3	0.359	0.365
Thulium	69	2	0.375	0.391
EDTA solutions				
Gadolinium	64	7	9.29	7.34
Dysprosium	66	5	0.137	0.140
Erbium	68	3	0.098	0.093

\* Number of unpaired electrons in 3+ ion

\*\* T2 too long for accurate measurement

The T1 and T2 relaxivity (the rate of change of relaxation time with concentration) for aquions and EDTA chelate of some tripositive lanthanides at 30°C is shown in Table 1. In general T1 and T2 relaxivity are similar. The early members of the series show extremely low relaxivity and will not be considered further, gadolinium is very high and the second half of the series have moderate relaxivity. Seen in

detail, the second half of the series show that relaxivity increases with atomic number. Chelation with EDTA decreases relaxivity in the three ions examined. The greater percentage decrease for erbium may relate to its smaller atomic diameter. At the earliest time of examination, 15 minutes after preparation, the Eu<sup>2+</sup> ion was already partly oxidised. Measurement at this time showed an order of magnitude greater relaxivity than seen for the second half tripositive ions. Extrapolation to the time of manufacture suggests it has a similar relaxivity to gadolinium.

Temperature affected relaxivity for both aquions and chelates. For the second half of the series temperature dependence increased slightly with atomic number, e.g. relaxivity fell by 13% over the temperature decrease of 40°C to 20°C for thulium aquions but only by 3% for terbium aquion whilst gadolinium decreased by about 15%. Temperature dependence of gadolinium relaxivity increased slightly on chelation but decreased for dysprosium and erbium demonstrating that temperature dependence may relate to relaxation effectiveness.

The T1 relaxation time of gadolinium aquions and chelates shows the expected non-linear frequency dependence where T1 increases with frequency. Tripositive lanthanides of the second half of the series show only a slight frequency dependence, but this is in the opposite direction to gadolinium. For example, over the range 2.5 to 80MHz there was an 8.5% decreased in T1 for 70mM Dy<sup>3+</sup> aquion, 4.1% for 70mM Dy<sup>3+</sup> chelated to EDTA and 7.8% for 85mM Dy<sup>3+</sup> with 2% agarose gel. T2 was usually similar to T1 except for the gel where T2 was decreased by the presence of the agarose.

Discussion

Effectiveness as relaxation agents fell into three categories:

- a) Ions with less than half-filled 4f shells were weak.
- b) Gd<sup>3+</sup> and Eu<sup>2+</sup> with exactly half-filled 4f shells were strong.
- c) Ions with more than half-filled 4f shells were moderate.

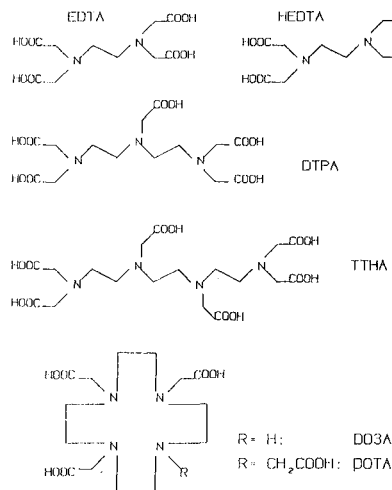
Relaxivity is not just related to number of unpaired electrons, eg Sm<sup>3+</sup> and Dy<sup>3+</sup> both have five but differ by 100 times in relaxivity. Also, relaxivity increases with atomic number ie with decreasing number of unpaired electrons, in the second half of the series. However, the reduction in atomic radius due to the lanthanide contraction plus the change from opposition to addition of the spin (S) and orbital (L) quantum numbers in the second half of the series explains the greater relaxivity of the later lanthanides. The decrease by one in co-ordination number in the second half of the series is evidently a minor factor. When the 4f shell is half full L is zero. There is no spin/orbital coupling. This may be the cause of the exceptional behaviour of the Gd<sup>3+</sup> and Eu<sup>2+</sup> ions.

**pH Dependence of Hydration Numbers and Relaxivities of Gadolinium Complexes**

C.A. Chang, J. Telser, H.G. Brittain, and M.F. Tweedle  
The Squibb Institute for Medical Research  
New Brunswick, NJ, 08903, U.S.A.

**Introduction:**

Gd(III) complexes usable as MRI contrast agents must remain intact *in vivo* while strongly affecting the spin-lattice relaxation time ( $T_1$ ) of solvent water. The former is best accomplished by complexes with high thermodynamic stability and kinetic lability while the latter occurs most effectively with the maximum number of coordinated water molecules (1,2). Because both the thermodynamic stability and kinetic lability of the complexes depend on the pH of the solution, it is important to be able to relate the measured relaxivity with the solution pH and chemical structure. We report here the spin-lattice relaxivity ( $R_1$ ) values for a series of Gd(III) complexes of the following linear and macrocyclic ligands: HEDTA, EDTA, DTPA, TTHA, DO3A, and DOTA over a pH range of 2 to 10. The results are discussed in terms of solution pH, complex stability, and the number of first sphere coordinated water molecules (hydration number,  $q$ ). The  $q$  values were determined for the analogous Tb(III) complexes over the same pH range.



**Experimental:**

Gd(III) complex stock solutions were prepared and standardized by direct or back complexometric titrations. Solutions of varying concentration at different pH values were then prepared by mixing the appropriate buffer solutions (ionic strength 0.1) and the stock complex solutions. The  $T_1$  value of each solution was measured by an IBM PC/20 Multispec relaxometer ( $39^\circ\text{C}$ , 0.47T). The  $R_1$  value for each complex at each pH was obtained by a linear least squares fit of the measured  $1/T_1$

values with the corresponding concentrations. The hydration numbers were determined by the Horrocks method (3).

**Results:**

The results are shown in Fig. 1. The relative standard deviations are  $\leq 5\%$  for  $R_1$  and  $\leq 20\%$  for  $q$ .

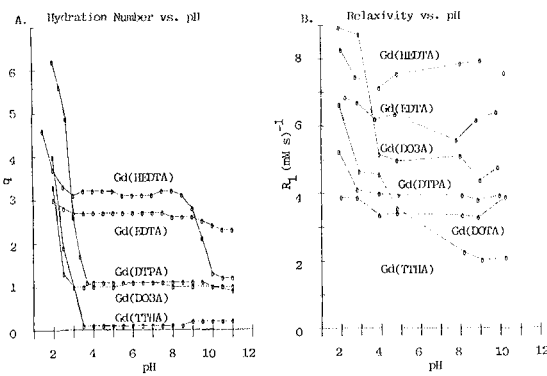


Figure 1: Plots of (A) hydration number,  $q$ , and (B) relaxivity ( $R_1$ ) values vs. pH.

**Conclusions:**

The observed relaxivity values decrease with increasing pH, as  $q$  decreases. When a ligand is fully complexed, the relaxivity value of the resulting complex no longer changes and this "limiting" value corresponds well with the number of first sphere coordinated water molecules ( $q$ ) on the metal center. Ligands with more donor atoms tend to give complexes with lower relaxivity. The observed order of  $R_1$  ( $q$ , pH 8) values are: Gd(HEDTA), (3 or 4) > Gd(EDTA), (3) > Gd(DO3A), (1 or 2) > Gd(DTPA), (1) > Gd(DOTA), (1) > Gd(TTHA), (0). Minor variations are probably due to different correlation times. At lower pH, complexes with higher thermodynamic stabilities give lower  $R_1$  values because a greater fraction of the  $\text{Gd}^{3+}$  is in the complexed form, e.g. the  $R_1$  value at pH 2 for Gd(DTPA)<sup>-2</sup> is lower than that of Gd(EDTA)<sup>-</sup>.

**References:**

1. Tweedle, M.F. et al. In Magnetic Resonance Imaging, 2nd ed., Partain, C.L., et al. eds., W.B. Saunders: Philadelphia, 1988. Vol. 1, p. 793.
2. Lauffer, R.B. Chem. Rev., **87**, 901, 1987.
3. Horrocks, W.D.W.; Sudnick, D.J. J. Am. Chem. Soc., **101**, 334, 1979.

## INFLUENCE OF MEDIUM AND STRUCTURE ON PARAMAGNETIC RELAXIVITY OF NITROXIDE STABLE FREE RADICALS.

P. VALLET<sup>1</sup>, Y. VAN HAVERBEKE<sup>1</sup>, P.A. BONNET<sup>2</sup>, G. SUBRA<sup>2</sup>, J.P. FERNANDEZ<sup>2</sup>, J.P. CHAPAT<sup>2</sup> AND R.N. MULLER<sup>1</sup>.

<sup>1</sup> Department of Organic Chemistry and NMR Laboratory, University of Mons, B-7000 Mons, Belgium

<sup>2</sup> Laboratory of Pharmaceutical Organic Chemistry URA CNRS, University of Montpellier, F-34060 Montpellier, France.

### INTRODUCTION.

Proposed very early as contrast agents for MRI (1), the nitroxide stable free radicals (NSFR) have had a rather limited success in spite of their remarkable potential. The still open question of their toxicity and an apparently irremediable low paramagnetic relaxivity are mainly responsible for this situation. It has been reported (2) that water insoluble NSFR like doxyl stearate (DOS) have a higher relaxivity in aqueous solutions of albumin where they stick to the protein and can interact more efficiently with the surrounding water molecules. In this work, we show that this behaviour is also observed with water soluble compounds and that the relaxivity enhancement is structure dependent.

### METHODS.

The NSFR are commercially available (Aldrich) or have been synthetized by described procedures (3). Protein containing solutions have been prepared from lyophilized human serum Kontrollogen-L (Behring). Nitroxide concentration has been measured by ESR (Bruker ER200D) and by chemical reduction followed by relaxometry (4). Proton Nuclear Magnetic Relaxation Dispersion (NMRD) profiles have been recorded between 0.25 mT and 1.2 T on a IBM Research Relaxometer. In addition, R1 measurements have been performed at 4.7 T on a Bruker MSL 200-15 system.

### RESULTS AND DISCUSSION.

Six NSFR diversely substituted (fig.1) have been studied in pure water and in protein containing solutions prepared from lyophilized serum.

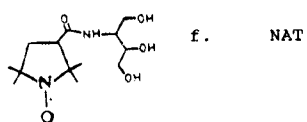
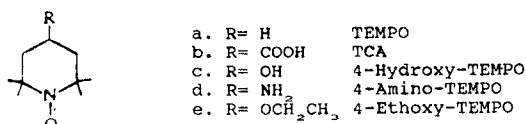


(fig.1)

The relaxivity profiles observed for all these compounds in water are identical and represented by the solid line in figure 2. In serum however, each NSFR experiences an increase of relaxivity which can be correlated to the relative balance of the lipophilic/hydrophilic character of the molecule. Illustrative enough are the very small relaxivity enhancement of the highly hydrophilic NAT and the shift to

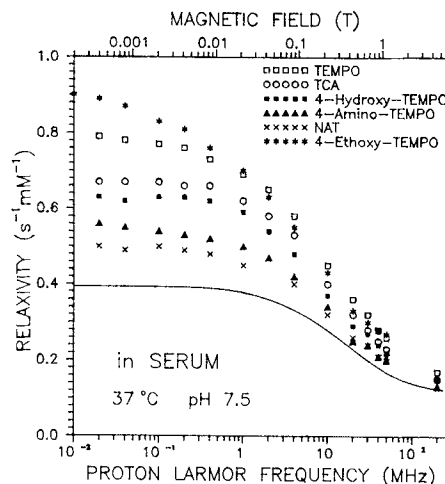


(fig.2)

higher relaxivity induced by the substitution of an hydroxyl group (4-hydroxy TEMPO) by an ethoxy group (4-ethoxy TEMPO). The lipophilic/hydrophilic character of the structure affects the degree of its association with the protein. Owing to this binding at the surface of the macromolecule the relative diffusion coefficient of the nitroxide groups and the water molecules is decreased. This in turn improves the magnetic interaction between the electron and the water protons and enhances the relaxivity.

### CONCLUSIONS.

Relaxivity of nitroxide group is not irredeemably fixed to a low and constant value. Indeed, in protein containing aqueous media, an increase of relaxivity has to be expected according to the relative extent of the lipophilic/hydrophilic character of the paramagnetic compound. This phenomenon will have to be taken into account when concentration of NSFR will be evaluated through relaxation rates measurements since the relaxivities in protein containing media may significantly differ from those measured in water solutions.

### REFERENCES.

1. Brasch R.C., Nitecki D.E., London D., Tozer T.N., Doemery J., Tuck L.D., Wolff S., Proceeding of the first Annual Meeting of the Society of Mag. Reson. Med. 25, 1982.
2. Bennett H.F., Brown III R.D., Koenig S.H. and Swartz H.M., Mag. Reson. Med. 4, 93, 1987.
3. E.G. Rozantsev, "Free Nitroxyl Radicals" (Plenum Press, New York-London, 1970).
4. R.N. Muller et al. unpublished results.